Simulating Strongly-Coupled Light-Matter Systems with Ultracold Atoms

A Dissertation Presented

by

Joonhyuk Kwon

to

The Graduate School

in Partial Fulfillment of the Requirements

for the Degree of

Doctor of Philosophy

in

Physics

Stony Brook University

January 2022

Stony Brook University

The Graduate School

Joonhyuk Kwon

We, the dissertation committee for the above candidate for the
Doctor of Philosophy degree, hereby recommend
acceptance of this dissertation.

Dominik Schneble – Dissertation Advisor
Professor, Department of Physics and Astronomy

Thomas Weinacht – Chairperson of Defense
Professor, Department of Physics and Astronomy

Tzu-Chieh Wei
Associate Professor, Department of Physics and Astronomy

Robert Konik
Chair, Condensed Matter Physics and Materials Science Department
Brookhaven National Laboratory

This dissertation is accepted by the Graduate School.

Eric Wertheimer
Dean of the Graduate School

Abstract of the Dissertation

Simulating Strongly-Coupled Light-Matter Systems with Ultracold Atoms

by

Joonhyuk Kwon

Doctor of Philosophy

in

Physics

Stony Brook University

2022

Understanding and harnessing light-matter interactions is central to the development of applications in quantum information science. Using ultracold atoms in optical lattices as a quantum simulator for such optical phenomena, we have recently implemented a platform of artificial quantum emitters that radiate matter waves into an analogue of a photonic-crystal waveguide. In this dissertation, we extended our studies of analogues of atom-photon bound states to implement a new type of strongly-coupled quasi-particle in a lattice geometry that can be viewed as the matter-wave equivalent of an exciton polariton. We spectroscopically accessed the dispersion relation of this matter-wave polariton and studied polaritonic transport in the superfluid and many-body Mott insulator regimes.

Polaritons, a key feature of strongly-coupled light-matter interactions, are at the heart of emerging platforms for quantum in-

formation processing and simulation. Unlike all other polaritons in the optical domain, our matter-wave polariton is dissipation-free and fully tunable and thus can serve as an ideal testbed for polariton physics.By combining the Bose-Hubbard and Weisskopf-Wigner models, the matter-wave polariton system naturally connects two separate areas, condensed-matter physics and quantum optics.

Dedicated to my mother

Contents

List of Figures

Acknowledgements

I have thought many times about the moment of writing this acknowledgement as a final step of my dissertation. However, how I feel at this moment is not like what I imagined; looking back on my journey towards my PhD degree, I have to say that everything I achieved in this period was with the help of all the great people around me and I am incredibly lucky to have them in my life.

I first want to thank my advisor, Dominik Schneble. He has been the best advisor that I could possibly have dreamt about. From the first moment I met him in his class, he has always been supportive and full of passion. It is impossible to describe in this limited space, but I still would like to write down what I can since he is the one that I truly revere and want-to-be both as a scientist and a person. Dominik guided me how the physicist should be by showing and sharing his life with us. His endless enthusiasm toward the truth and high standard of self criticism is more than what I read from the textbook for being a good scientist. I also enjoyed every moment I talked with him no matter what the topic was, since he is a great person beyond being an advisor. He is always considerate, warm-hearted and full of (German) humor (not a sarcasm!) that I love. What I do miss already is the presence of Dominik at the corner of the lab office as I am leaving, but I believe that a bonding between me and him in our life has just started.

I also thank the committee for my dissertation, Tom Weinacht, Tzu-Chieh Wei, and Robert Konik for their effort, support and time. I appreciate their careful and thorough reading of my dissertation with insightful comments. I am thankful to Robert Konik for kindly offering to serve as an external committee member and providing critical comments and advice that make my thesis more accessible. I also thank Tom and Tzu-Chieh for always bringing up critical questions with great insight for giving me good advice. I have to say that I greatly enjoyed the joint meetings and discussions with Tzu-Chieh's group over many years that were always providing theoretical richness and stimulation.

It was an exceptional pleasure to work and collaborate with wonderful people in the laboratory. During my early years, I learned everything that I

needed in a lab from Ludwig Krinner. He is an excellent physicist with great mastery of details that I always admire, and he is also a great lab mate as a person. I still miss our post-conference trip to Miami. I am also indebted to Arturo Pazmiño, who taught me all the skills that I need in lab. His amazing skills for dealing with equipment and electronics still benefit the whole lab greatly. My life in lab can not be described without Michael Stewart, who is not only a great physicist but also a heartwarming person. I enjoyed all the friendly banter we had all the time, even while under heart-attack-inducing machine troubles, and most of all, we went through all the things together. Alfonso Lanuza is a very talented physicist and I am absolutely indebted to his awesome theoretical abilities. It was a great pleasure of mine to work with him, and I am also happy to see that he is now a form of experimentalist as well. I have to say that I admire his great artistic skills as much as I do Mike's, which might actually mean that I have some kind of a preconception toward (semi-)theorists. I would like to thank Youngshin Kim, a great physicist and a wonderful lab colleague. He is absolutely reliable and steadfast, and also provides fantastic insights. I enjoyed all the moments that we measured all the data points with a superposition of concern and joy. He is now truly a core of our lab and I am looking forward to seeing his great work in the near future. Hongyi Huang, who recently joined our group, has already become an essential member of the lab. He is an excellent graduate student and absorbs all the knowledge like a sponge. I have no doubt about his successful PhD life in our group.

I am also grateful for being a part of the wonderful AMO community at Stony Brook. I am thankful to professors Hal Metcalf, Tom Weinacht, Eden Figueroa and Tom Allison. Under their leadership, all AMO graduate students were always rooting for and helping each other inside and outside of the work, and this made me truly feel like I belong here. I will miss all the small talk and Friday lunches with our incredible basement members especially Yusong, Chuan, Brian K, Spencer, Sam, Brian A, Sonali, Guodong, Bertus, Yifan, Xiaoyang, Samet, Jay, Eli, Chris, Eunji and Max.

My life outside of the lab in Stony Brook was all about my Foxhill friends, Junsik You, Jaehyeok Chang, Dongwon Han and Kyle Lee. From the beginning to the end, I shared all my life with them with great pleasure. All the moments that we shared together were memorable and invaluable. I already miss everything we've enjoyed including food, drinks, trips and all friendly banter. I am so glad that we all indeed made it as we initially planned many years ago. Each of you deserves more than a full page, but here I shortened it down since I know that this is only the beginning of our story, and we are the one group.

Last but the foremost, I could not have made it without the endless support of my family. I have always tried to make my mother and father proud of me, and I am now incredibly happy to say that I have made it this far with their support. I could always feel their bottomless love that is encouraging me all the time, and I should say that I am also proud of my parents. I thank my sister, and I have to say that she is the most promising person, and I can stay abroad for many years without any concern only because of her. Lastly, I would like to thank my wonderful wife, Sohyun. I never thought that I might have a chance to thank my wife in my thesis, and I am so lucky that I am doing so. It is hard for me to describe how much I got encouraged by her support and presence. I can't wait for the incredible journey that lies ahead of us.

We are grateful for the generous support by the National Science Foundation of the United States of America (NSF).

Chapter 1

Introduction

Since the early 1900s, quantum mechanics has given a new point of view of the microscopic world where classical understanding does not work, and indeed this has greatly affected the development of statistical physics: At low temperature, the spin nature of the particle determines the behavior of an ideal gas to either Bose-Einstein statistics for spin-integer or the Fermi-Dirac statistics for spin-half integer particles.

Bose-Einstein Condensation (BEC) was predicted in 1924 [1–3] but only relatively recently observed in dilute atomic gases [4–7] in 1995. BEC is named after S.N. Bose and A. Einstein, who showed that the particles with integer spin (boson) can have a macroscopic occupation of a single quantum state. In a trapped gas, this degenerate state exhibits macroscopic coherence which enabled the groups of C. Wieman and E. Cornell; R. Hulet; and W. Ketterle to first observe BEC in the real world. Since then, quantum gases using ultracold and dilute gases paved a way toward studying ideal quantum systems in atomic, molecular, and optical (AMO) physics. Experiments showed that cooling fermionic atoms also leads to quantum degeneracy as degenerate Fermi-Dirac gases (DFG) [8–11] in potassium atoms. Starting from rubidium [4], various atomic species have been used to realize degenerate quantum gases in the last two decades; alkali-metals (lithium [5, 7], sodium [6], potassium [11, 12] and cesium [13]) which are easy to laswer-cool, alkaline earth metals (calcium [14], strontium [15, 16]), hydrogen [17] and metastable helium [18], chromium [19], and even lanthanides (ytterbium [20], erbium [21], and dysprosium [22]) have recently come into heavy use based on the experimental purpose.

Research with BEC has also expanded explosively. In the early days, coherence properties [23–28], collective excitations [29] and propagation of sound [30] in BEC were studied followed by works on solitons [31, 32] and vortices [33–35]. Moreover, advanced techniques that are popular today were developed such as tuning interactions between ultracold atoms via Feshbach resonances

[36, 37] and Bragg spectroscopy [38]. Studies with Fermi gases also gave insights into long-lasting questions such as BEC-BCS crossover [39, 40] and the realization of the polar molecules [41–44].

Ultracold atomic systems became even more versatile in combination with optical lattices [45, 46]. Optical lattices are an ideal platform to test theoretical models that were developed for condensed-matter physics by virtue of the fact that they are defect-free and have an unparalleled degree of tunability. This system provides analogous models to study fundamental physics underlying solid-state phenomena, thus playing the role of an analog quantum simulator. Quantum simulation, first suggested by Feynman [47] in 1982, is one of the main directions in the quantum information paradigm.

Realizing the Bose-Hubbard model [48] on a square lattice led to the remarkable observation of the phase transition between a superfluid and a Mott-insulator [49, 50]. Other geometries [51–54] have also been studied for various models, such as Haldane [55] and Hofstadter models [56, 57] with the help of the realization of spin-orbit coupling [58–60]. Also, optical lattices with fermions have been used to implement the Fermi-Hubbard model and have led to the detection of anti-ferromagnetism [61–64]. Adding disorder with laser speckle [65] or atomic disorder [66] to the Hamiltonian allows for studies of Anderson localization [65, 67–69] and Aubre-André model [70] with interesting features such as a mobility edge [71–73] and a topological Anderson insulator [74]. Present-day technology even enables single-site resolved imaging in two-dimensional systems for bosons [75–77] and fermions [78–81].

In this dissertation, we will discuss experiments with BEC using a novel platform for the study of quantum-optical phenomena using matter waves that was realized in our laboratory recently. In this platform, we use hyperfine-state dependent optical lattices, which have a long history in the Schneble laboratory where they have led to demonstrations of collinear four-wave mixing of matter waves [82], superfluidity of interacting mixtures [83], glassy behavior [66], probing ultracold-atom crystal with matter waves [84], and non-adiabatic diffraction of matter waves [85]. With the improved techniques and equipment stability, we recently utilized matter-waves as a substitution for photons in two-level quantum emitter systems [86, 87]. Very recently, we combined this with the Bose-Hubbard model of condensed-matter physics to realize a strongly interacting polaritonic system [88] as will be covered in the main text.

In chapter 4, we briefly review the earlier work [86] on an open quantum system in which a two-level quantum emitter is coupled to a continuum of modes. The Hamiltonian of this system is the Weisskopf-Wigner model [89], which describes the mechanism of spontaneous decay of the excited state under emission of a photon [86]. The work established our matter-wave platform, in

which a two-level system is realized via a microscopic atom trap (a site of an optical lattice) that is occupied (excited state) or empty (ground state). The quantum electrodynamic (QED) vacuum field that couples to the atomic dipole moment is replaced by a matter-wave vacuum that couples to an effective dipole moments generated via a classical microwave field.

We also review our extended experimental study of non-Markovian dynamics of a matter-wave quantum emitter in a structured vacuum [87], to which the author of this dissertation contributed significantly. By providing a band structure to an emitted matter-wave of which we isolated a single band, we observed the transition of decay dynamics from spontaneous decay to vacuum Rabi oscillations, depending on the ratio between the band width and the coupling strength. This gives a connection between regimes ranging from the Weisskopf-Wigner model to the Jaynes-Cummings model of cavity QED limit where only one mode is available for emission. It also highlights the role of bound states, which are formed by an evanescent matter-wave surrounding a partly decayed emitter, in analogy to the atom-photon bound state [90].

In chapter 5, the main focus of this thesis, we extend our understanding of the atomic bound states to a more general context, a polariton, which is a quasiparticle formed between photon and matter-excitation. In our case, this excitation is an atom hopping in a lattice, while being surrounded by a virtual cloud of matter-wave excitations; forming what we will call a matter-wave polariton.

The history of polariton research is very deep and broad over many fields, and since its first description as linear superposition of light and matter excitation [91, 92], polaritons have been an as essential key to understanding the nature of light-matter coupling [93]. The core feature of a polariton is captured by the realization of microcavity polariton [94], which shows observation of coupled exciton-photon mode splitting that suggests quasi-particle interpretation. There are more than 70 different types of polariton [95] in various subfields, ranging from semi-conductor excitons [96–98], coupled cavity arrays [99, 100] to circuit QED [101], with various applications [102, 103] especially in the quantum information since it provides a way to control the interaction of photon.

These various platforms of different polaritons all share the feature of strong light-matter coupling, which is often difficult to achieve due to a finite Purcell factor [104], i.e. the residual coupling to modes not participating in the polariton formation. This is not the case for our matter-wave platform, where the Purcell factor diverges. With our matter-wave platform, we realized a polaritonic dispersion relation in an optical lattice. Due to the coupling of the heavy particle to lighter matter wave, it is essentially in analogy to an exciton-

polariton system [96, 98]. The matter-wave polariton we introduce here can be used as a new platform for fundamental studies of polaritonic systems, since it provides full tunability of polariton properties while still containing the features of conventional polaritons. By controlling those parameters in the regime of interest, the system can also mimic polaritonic systems in waveguide [105–108] and circuit QED [102].

The system we introduce has both features of radiative polaritonic behavior and condensed-matter physics. The band structure that we implemented can be described by a 'polaritonic' Bose-Hubbard hamiltonian, which describes a phase transition between superfluid to Mott insulator.

In this dissertation, prior to reviewing the platform and related experiment, we first introduce the experimental setup and related background theories briefly in following chapter 2. More detailed theoretical concepts about band structure and Bose-Hubbard model is discussed in chapter 3. After reviewing the matter-wave platform in chapter 4 and discussing the experiments on matter-wave polaritons in chapter 5, we finally suggest some future experiments in chapter 6.

Chapter 2

Basic experimental methods

For the past two and a half decades, Bose-Einstein Condensates (BEC) have been studied in various contexts and the related experimental techniques are now well-established. Depending on the target application, however, the details for an experimental setup can be very different. In this chapter, we will briefly review our experimental setup for BEC of rubidium-87 atoms and the related theoretical background at the ultracold atom lab at Stony Brook, which is universal over this whole dissertation.

2.1 Making BEC

In this section, we will take a short look at how we produce and use ^{87}Rb Bose-Einstein condensates in the Schneble laboratory. Details of the experimental setup have already been discussed in a number of previous dissertations [109–115] and a publication [116]. Thus in order to avoid redundant information, we will discuss the mechanism of creating BEC rather qualitatively, and focus more on the unique features related to the experiments in this dissertation.

Fig. 2.1 shows a photo of our BEC machine, which only includes the crucial part where the atoms are present. To obtain BEC, we start from a solid sample of room-temperature ^{87}Rb atoms, inside our 'oven' attached to the ultrahigh vacuum chamber that controls the temperature of the sample and its vapor pressure. This control is done by a Peltier element and we are maintaining the temperature at $\sim 15°C$. Sublimated atoms are now in an ultrahigh vacuum ($\sim 10^{-9}$ Torr) cylindrical tube of glass ((1) in fig. 2.1). A first cooling step involves laser cooling in a magneto-optical trap (MOT), which consists of three orthogonal pairs of counter-proparating beams that are red-detuned from the D_2 line ($F = 2 \rightarrow F' = 3$) by 18.7MHz (cycling light) (cf. fig. 2.2). In brief, atoms absorb near resonant light at 780nm from laser beams

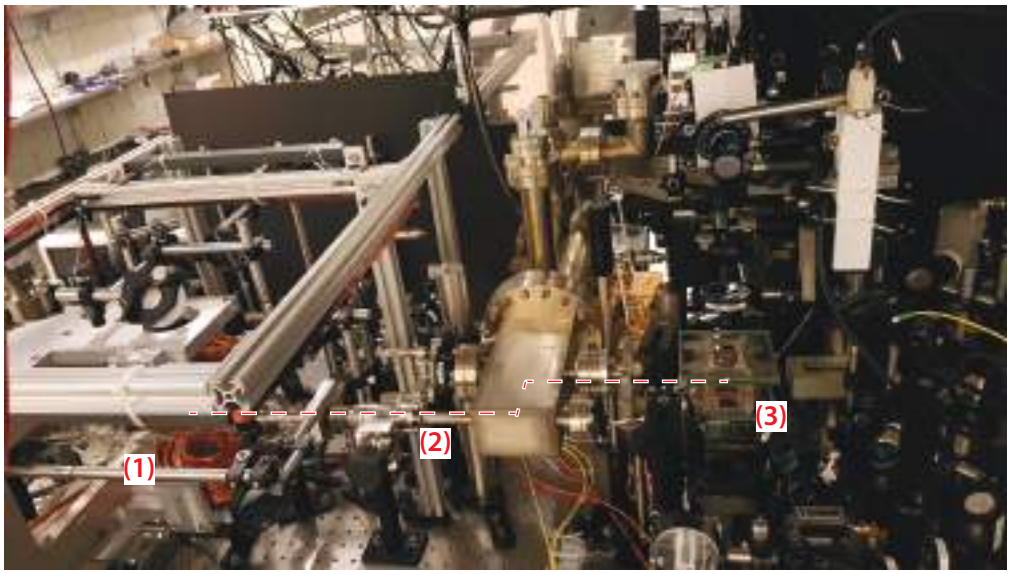

Figure 2.1: BEC machine at SBU. This photo only shows the ultrahigh-vacuum chamber of the equipment that atoms moves through. The movable large pair of (brown) coils in (1) generate a magnetic field gradient with its anti-Helmholtz configuration, and a magneto-optical trap is created in a cylindrical glass tube with the help of near-resonant laser beams. The magnetically trapped atoms are moved through the differential tube (2) and arrive at the science-cell (3), along the path depicted as a red-white dashed line.

in co- and counter-propagating directions that change their momentum and produce a friction force ($\boldsymbol{F} \propto -\boldsymbol{v}$) using the Doppler effect [117]. Using the presence of Zeeman-shifted magnetic sublevels, a spatially varying resonance frequency due to a linear magnetic field gradient ($\sim$ 10G/cm) created by a quadrupole magnetic coil causes a restoring force ($\boldsymbol{F} \propto -\boldsymbol{x}$) to the atoms. We use three different laser beams; cycling light ($F = 2 \rightarrow F' = 3$) aforementioned that creates orthogonal 3-axis counter-propagating laser trap, repump light ($F = 1 \rightarrow F' = 2$) that pumps inactive $F = 1$ atoms back into the $F = 2$ states, and depump light ($F = 2 \rightarrow F' = 2$) to finally park all atoms into the final $F = 1$ ground states via optical pumping (cf. fig. 2.2).

In practice, we use a Toptica DL-pro-780 as a seed laser locked via Doppler-free polarization spectroscopy to rubidium to generate $\sim$ 30mW of 780nm light with narrow linewidth ($<$ 500 kHz). Since we need relatively high laser power ($>$ 400mW) for the MOT, we amplify the light to $\sim$ 1W using a Toptica BoosTA laser amplifier, which provides enough laser power for cycling, depump light ($>$ 10mW) and $F = 2$ imaging light (cf. sec.2.3). For the repump light

(and $F = 1$ imaging light), we use a Toptica DL-100 to generate light of > 50mW that is separately locked to $F = 1 \rightarrow F' = 2$ transition using Doppler-free saturation spectroscopy. All beams except for the repump light are delivered to the atoms using single-mode optical fibers, and can be switched using a combination of mechanical shutters and acousto-optical modulators.

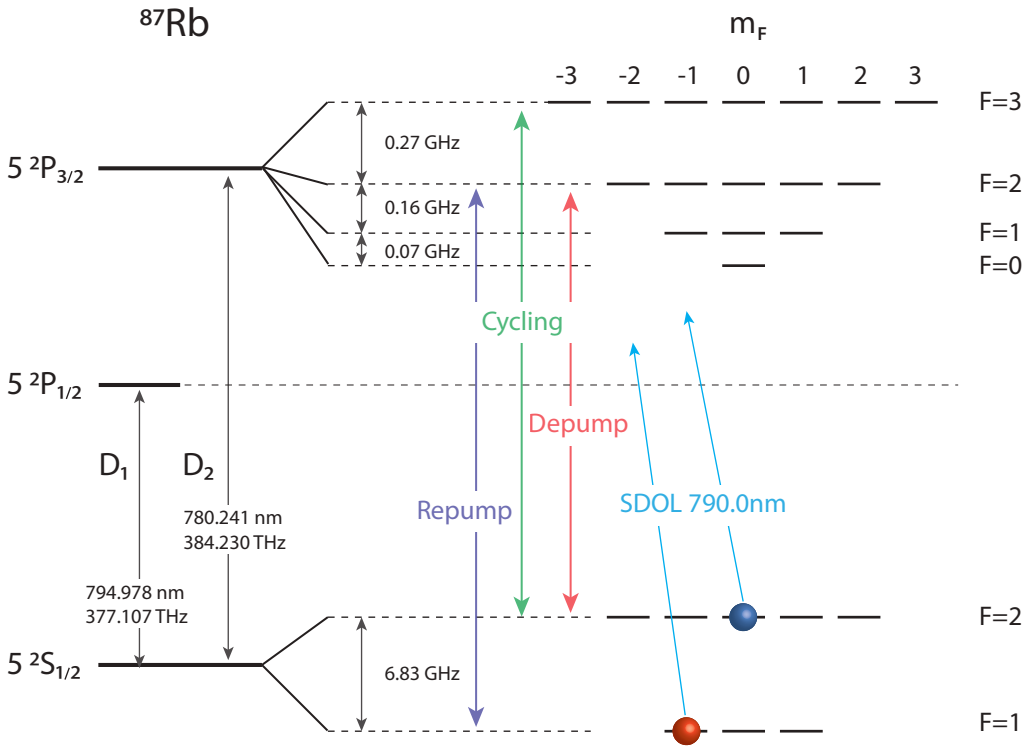

Figure 2.2: ^{87}Rb energy level scheme. Transition data for D_1 and D_2 line is taken from [118]. $5^2S_{1/2}$ contains the ground states that are in use for the experiments that consists of five $F = 2$ states and three $F = 1$ states. When a bias magnetic field is applied, Zeeman splitting will happen between degenerated m_F levels (see fig. 2.6). Note that the sublevels for $5^2P_{1/2}$ are not shown. For cooling process, three specific transitions are in use optically; cycling ($F = 2 \rightarrow F' = 3$), repump ($F = 1 \rightarrow F' = 2$) and depump ($F = 2 \rightarrow F' = 2$) light. These transitions are also used for our imaging (see sec. 2.3).

At the zero magnetic field (and zero gradient) accomplished by the gradient coil around the cylindrical vacuum cube, applying the detuned cycling light gives an "optical molasses" providing sub-Doppler cooling [119, 120]. Then

by turning off the repump light and actively turning on the depump light, all cooled atoms are now in $F = 1$ state with the low temperature $\approx 100\mu$K.

Next, we transfer the atoms into a quadrupole magnetic trap [121], using a same coil that is used for creating MOT above. Note that the atoms in hyperfine states of low-field seekers are only trapped here, which is $|F = 1, m_F = -1\rangle$ (since $F = 2$ states are depumped at this stage). We then transport the atoms into the 'science-cell' (fig. 2.1 (3)), an ultrahigh-vacuum ($\sim 10^{-12}$ Torr) quartz glass cell (2cm $\times$1cm $\times$5cm), by physically moving the magnetic trap coils. The pressure difference between two sides is maintained by the differential tube (diameter $\sim$ 1cm) that gives a factor of 100 in pressure (see fig. 2.1 (2)). The maximum axial field gradient is very stiff $\approx$ 480 G/cm [114] to maximize adiabatic compression and optimize the transport through the differential pumping tube. The vacuum is maintained using a combination of ion and titanium sublimation pump.

In the science-cell, we use a series of evaporative cooling steps [122]. The first step is a pre-evaporative cooling in a linear quadrupole trap using an 'RF knife', which creates oscillating magnetic fields of adjustable frequency (1$\sim$100 MHz) that changes the internal states of the atom in resonance and expels the most energetic atoms, thus lowering the average temperature of the atoms in the trap and increasing the phase-space density (PSD). The minimum temperature we here can achieve is about 100μK because of Majorana losses that happens from the sudden spin-flip as the atoms pass the center of the magnetic trap where the field is zero and no quantization axis is provided. Then we create a time-orbiting potential (TOP) trap [123] by adding a rotating bias field in $x-y$ plane to the quadrupole magnetic trap. The field-zero is now rotating rapidly around the center, while the magnetic field at the trap-center is offset from zero thus avoiding Majorana losses. We apply another ramp of the RF knife as the TOP trap cools atom further.

We then transfer atoms from the magnetic trap into the 3D optical trap, which is made by intersecting two orthogonal laser beams at 1064nm ($\omega_0 = 140\mu$m, $\sim$ 1mW) from our ytterbium fiber laser (YLR-20-1064-LP-SF/PL series). The optical trap gives us full freedom of using magnetic fields in the experiments as required. In the optical trap, we apply the third evaporative cooling step by simply lowering the optical trap depth slowly, which lets the high-energy atoms escape and re-thermalizes the rest of atoms to lower temperature and higher PSD.

With the combination of cooling steps, we achieve BEC of typically order of $\sim 10^5$ atoms at temperatures $\sim$ 100nK. We generally prepare the atoms in the $F = 1$, $m_F = -1$ state with the free control of atom number by controlling the depth of the optical trap. The relevant hyperfine states of ^{87}Rb are shown

in fig. 2.2 [118]. Among the 8 hyperfine states (3 for $F = 1$, 5 for $F = 2$), we typically use $|F = 1, m_F = -1\rangle$ (red atom in fig. 2.2) and $|F = 2, m_F = 0\rangle$ (blue atom in fig. 2.2) states for the convenience in technical point of view, especially in regards of magnetic field sensitiveness. (Most of the experiments done in the lab need a high level of stability and accuracy, so any possible issue that can induce the unwanted fluctuations should be minimized. Details are discussed in later sections.)

It should be stated that the moving-coil system that we have in the lab is somewhat non-ideal as it requires lots of open spaces for the coils to move that cannot be used otherwise. On the other hand, the large spatial separation between the MOT and the science cell makes a life of an experimentalist very easy in practice, especially in terms of trouble-shooting. Also, this large coil pair provides multiple functions throughout the experimental process. Starting from the magneto-optical trap, it traps and moves the atom to the high-vacuum cell, and serves as the main coil for the TOP. Furthermore, at the stage of the detection, by pushing back about $\sim$ 1cm, the coil also provides the magnetic field toward transverse axis, which is used as Stern-Gerlach separation for different hyperfine states. In the past, we even used the coils - in Helmholtz configuration- to access a Feshbach resonance at $\sim$ 1007G [114].

2.2 Hyperfine state control

2.2.1 Zeeman sublevels in magnetic bias fields

Most of the work in our lab is based on the manipulation of atoms in different hyperfine states. For example, starting with BEC of atoms at $|1, -1\rangle$ state, as previously discussed, we typically implement a transfer into $|2, 0\rangle$ state. Historically the $|2, -2\rangle$ state was generally used together with $|1, -1\rangle$ in our lab to achieve high Rabi-frequency for a given coupling field, but we used $|2, 0\rangle$ in this dissertation for reasons of magnetic field insensitivity and state-selectivity (see sec. 2.5).

For implementing transitions between states, it is of importance to precisely control the corresponding energy gap. In our lab, the optical dipole trap potential that traps BEC is practically state independent since it is very far-detuned, so that there is no differential energy shift between the states. The bare energy gap between states is mainly dependent on the offset magnetic field. The magnetic field dependency of each energy level in the $S_{1/2}$ ground

state manifold can be calculated in the Breit-Rabi formula [124] as follows:

$$E_m(x) = -g_I \mu_N m B_0 - \frac{\Delta E}{2(2I+1)} \pm \frac{\Delta E}{2} \sqrt{1 + \frac{2mx}{I+1/2} + x^2} \tag{2.1}$$

in case of an atom with $J = 1/2$, where $I = 3/2$ is the nuclear spin of rubidium-87, B_0 is the applied magnetic field, ΔE is the bare energy separation between hyperfine states, $x = (g_e \mu_B + g_I \mu_N) B_0 / \Delta E$ and $m = m_i + m_j$ is the magnetic quantum number.

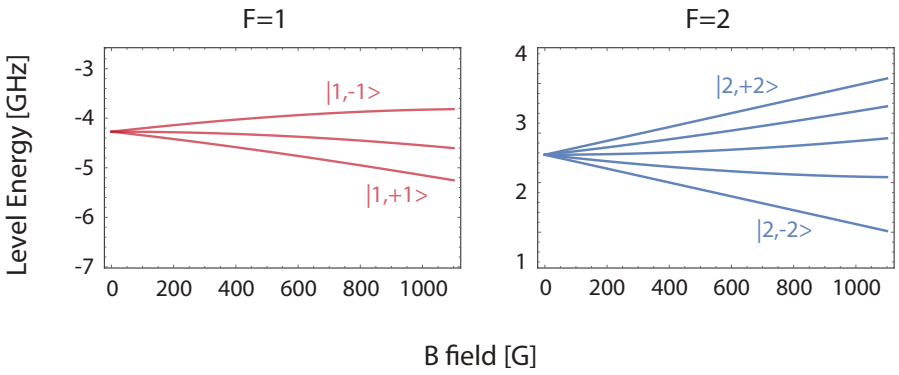

Figure 2.3: Breit-Rabi formula that gives the energy level of each hyperfine state depending on the magnetic field.

Fig. 2.3 shows the magnetic field sensitivity of the energy level for each state. In our experiment, we tune the offset magnetic field to $\sim$ 5G along z-axis to provide the quantization axis. At zero magnetic field, the energy splitting between $F = 1$ and $F = 2$ is 6.834 682 610 GHz [118], and the linear Zeeman shift between neighboring m_F levels is ± 0.7 MHz/G. For spectroscopy purposes, the second-order contributions are even important at small fields. For very high magnetic field (> 1000G), $|2, -2\rangle$ states moves along with other $F = 1$ states.

2.2.2 Rabi oscillations

The manipulation of the internal hyperfine state in magnetic bias field is a key feature in our lab that allows us to prepare the system in a desired initial state. For the fixed energy levels, the most general technique for state transition is a Rabi oscillation.

In detail, it uses the oscillatory magnetic fields that drives magnetic dipole moment resonantly. Consider a spin-1/2 particle in an external magnetic field $\boldsymbol{B}(t) = \boldsymbol{B}_z + \boldsymbol{B}_{rot}(t)$, where $|\boldsymbol{B}_{rot}| \ll |\boldsymbol{B}_z|$ and $\boldsymbol{B}_{rot} \perp \boldsymbol{B}_z$. The spin precessing in the external field $\boldsymbol{B}_z$ forms a two-level system $|g\rangle$, $|e\rangle$ with energy spacing $\hbar\gamma B_z$, subject to the external oscillating field $B_{rot}(t) = B_1 \sin\omega t$. Starting from the Schrödinger equation

$$i\hbar|\dot{\psi}\rangle = \hat{H}\,|\psi\rangle \tag{2.2}$$

we then have the Hamiltonian

$$\hat{H} = \boldsymbol{\mu} \cdot \boldsymbol{B}(t) \tag{2.3}$$

where $\boldsymbol{\mu} = \gamma\hbar/2\hat{\sigma}$ is a magnetic dipole moment, $\hat{\sigma}$ is Pauli matrices and $\gamma = g\mu_B/\hbar$.

In the rotating frame, we can obtain the relation

$$i\hbar \begin{pmatrix} \dot{c}_g \\ \dot{c}_e \end{pmatrix} = -\frac{\hbar}{2} \begin{pmatrix} -\delta & \Omega \\ \Omega & \delta \end{pmatrix} \cdot \begin{pmatrix} c_g \\ c_e \end{pmatrix} \tag{2.4}$$

where $\delta = \omega - \omega_0$ is the detuning from the resonance frequency $\omega_0 = \gamma B_z$ and $\Omega = \gamma B_1$ is the Rabi-frequency.

Starting in $|g\rangle$ (spin down), the time evolution of the final state population is given as $P_{|e\rangle}(t) = c_e c_e^*$, which is

$$P_{|e\rangle}(t) = \frac{\Omega^2}{\Omega^2 + \delta^2} \sin^2\left(\frac{t}{2}\sqrt{\Omega^2 + \delta^2}\right). \tag{2.5}$$

Note that full population transfer can only be achieved on resonance ($\delta = 0$).

Fig. 2.4 (A) shows the time-dependent state transition with fixed detuning and Rabi-frequency, called Rabi oscillation or Rabi flopping, between $|1, -1\rangle$ and $|2, 0\rangle$ driven by a σ^+ polarized magnetic field. Here the coupling strength is $\sim \Omega = 2\pi \times 3.7$kHz, which gives about 270μs of the oscillation period as shown in the figure. We can also vary the detuning while the coupling time t is fixed, and it gives Rabi spectra as shown in fig. 2.4 (B). Here the width of the spectrum depends on the Rabi frequency as well as the pulse-duration. For the short-pulse regime, the higher the Rabi frequency is, the larger the spectral width is.

These Rabi spectra can be encapsulated in 3D plot from eq.2.5, as plotted in fig. 2.4 (C) in detuning and time domain with fixed Rabi-freqeuncy. Each feature from figure (A) and (B) can be shown as a cross section of the plot with zero-detuning and $t = 200\mu$s pulse duration, respectively.

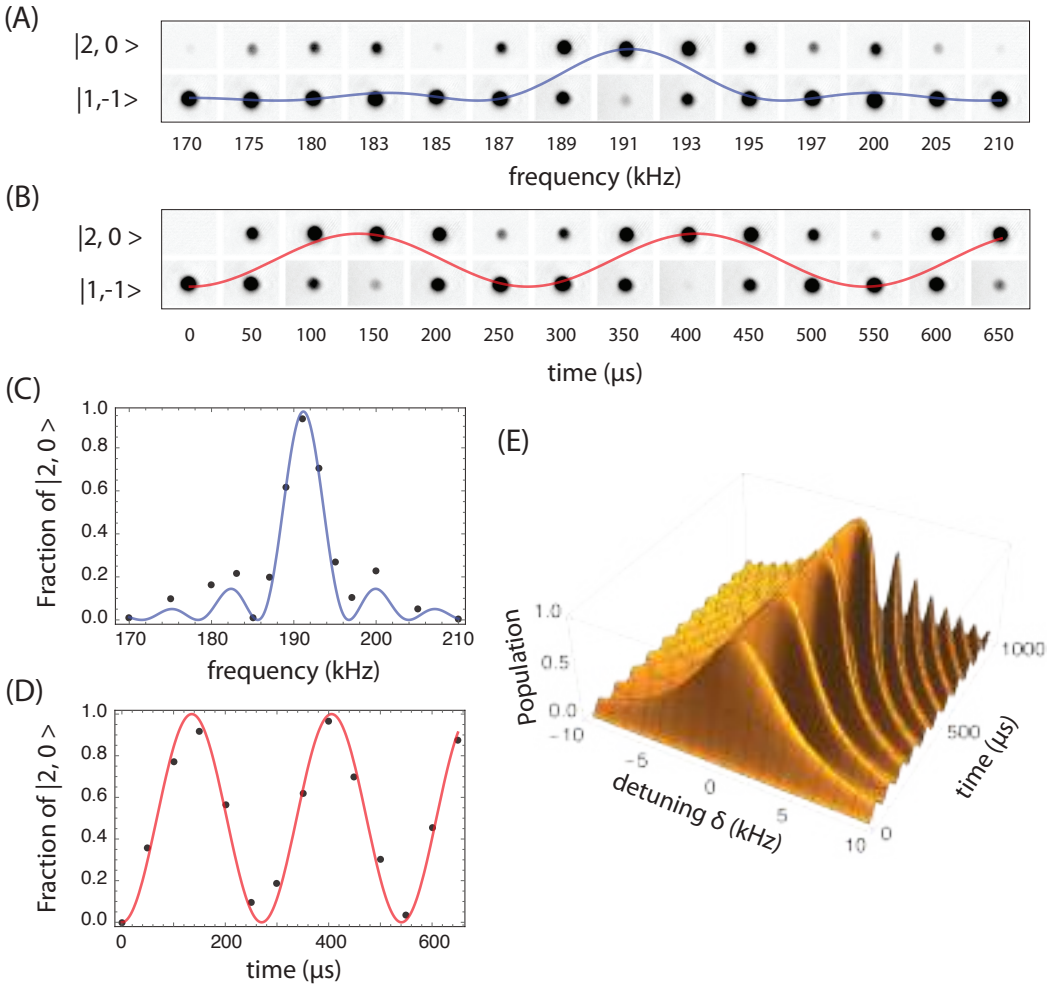

Figure 2.4: Rabi oscillation spectra. (A, B) Stern-Gerlach separated time of flight image of Rabi spectrum (oscillation) ($\Omega = 2\pi \times 3.7$kHz, square pulse) between $|1, -1\rangle$ and $|2, 0\rangle$ states in detuning (time) domain for fixed $t = 0$ ($\delta = 0$). Blue (Red) solid line is a fitted curve with eq. 2.5. (C, D) Rabi spectrum (oscillation) of the relative population of $|2, 0\rangle$ state in detuning (time) domain, data extracted from (A (B)). (E) Theoretically expected 3D plotted Rabi spectrum. The Rabi frequency is set as ($\Omega = 2\pi \times 3.7$kHz), the same with (A-D). Each feature from (C) and (D) is a cross section of the plot.

In our experiment, we use the Rabi-spectrum measurement to identify the coupling strength Ω and the corresponding magnetic field from the fitting as shown in fig. 2.4. When both two bare ground states are not in lattices, the resonance frequency ω_0 is the same with the bare energy splitting from the

Breit-Rabi formula (cf. eq. 2.1), but in the presence of the lattices, we need to take into account the zero-point energy shifts.

2.2.3 Landau-Zener sweep

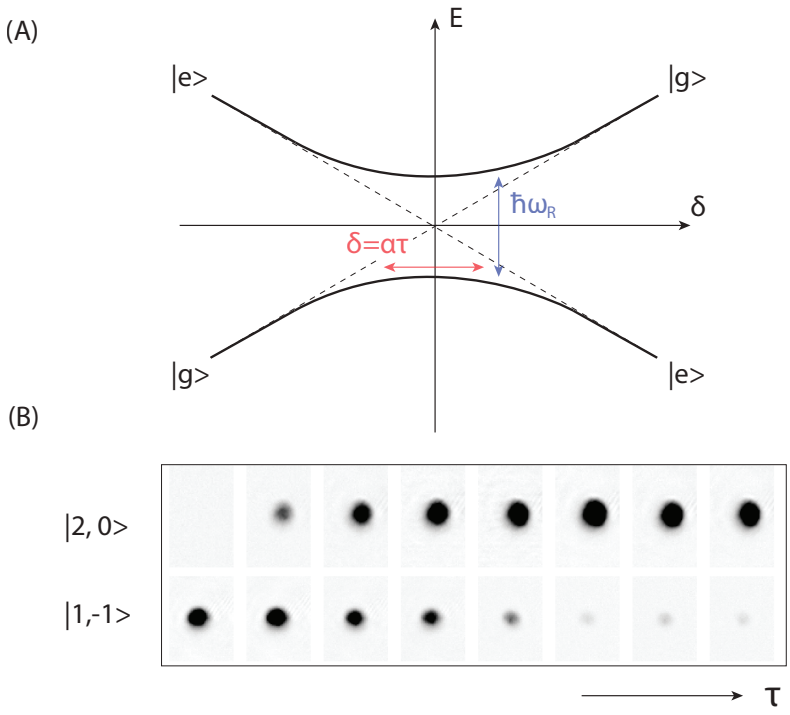

Figure 2.5: Landau-Zener sweep. (A) Schematic diagram. The incoming excited (ground) state goes out as the ground (excited) state if the sweep is adiabatic, along the thick solid line above (below). The adiabaticity depends on the ratio between the vertical gap (ω_R) and the horizontal sweep ($\delta = \alpha\tau$) where α is a sweeping velocity in time τ. Under the condition $\omega_R^2/\alpha \ll 1$, the sweep is adiabatic. (B) Experimental realization. $\omega_R = 2\pi \times 8.0$kHz, and the sweep time τ is varied from 0.1 to 10ms while $\delta = 1$MHz is fixed. The incoming state $|1, -1\rangle$ is transferred to $|2, 0\rangle$, and the transition rate depends on the sweeping time τ. For longer sweeping time, the adiabatic condition is fulfilled and most of the initial state is turned into the final state.

One of the most reliable ways to transfer one state totally to another state is to use the Landau-Zener (LZ) sweep [125]. This mechanism has been discovered in 1930s by Landau and Zener [126, 127], that uses the avoided-crossing

mechanism in energy and detuning domain. Fig. 2.5 (A) shows the schematic of the Landau-Zener sweep. In the energy-detuning plane, there is an avoided crossing at the resonance $\delta = 0$ where the two bare states (excited and ground) cross each other. The two dressed states (eigenstate of eq. 2.4) are separated by $\hbar\sqrt{\delta^2 + \Omega^2}$. Starting from the one state at effectively infinite negative detuning, scanning the detuning that crosses the resonance decides its final state depending on how fast the scan is. If the scanning speed is slow enough, the change of the eigenstate is adiabatic and the corresponding eigenvalue is deformed to avoid the level-crossing as shown in the figure. Here the competing parameters are the slope from x and y axis, i.e., the speed of detuning scan ($\delta = \alpha\tau$) where α is a sweeping velocity, and the Rabi-frequency (ω_R). If the sweep is too fast, the system is no more adiabatic and it follows the dashed line in the figure, so that the final state is the same with the initial state.

The adiabatic condition can be estimated qualitatively. From the figure (A), $\delta \approx \omega_R$ which gives $\tau \approx \omega_R/\alpha$. Also from the uncertainty condition $\Delta E = \hbar/\tau$, this should be much smaller than the energy $\hbar\omega_R$. This indeed gives $\omega_R^2/\alpha \ll 1$ as an adiabatic condition for the LZ sweep.

Fig. 2.5 (B) shows the experimental realization of the LZ transition. Starting with the initial state $|1, -1\rangle$, changing the detuning across the resonance under the transition time τ gives a state transition to the final state $|2, 0\rangle$. Here, the sweep rate depends on the sweep time τ as shown; for very short sweeps, the state is unchanged which means that the system is fully non-adiabatic. As the τ increases, the system gets more adiabatic, and most of the $|1, -1\rangle$ population are turned into the final state $|2, 0\rangle$ for long enough sweep time τ.

2.2.4 Two-photon transition

Sometimes it is required to make a transition in the system between the main two bare states (typically called red and blue) which is not allowed by the selection rules for a one-photon transition. For example, the transfer $|1, -1\rangle$ to $|2, 1\rangle$ is not generally allowed due to the conservation of angular momentum. In such cases, we use a two-photon Raman resonance, which uses a third state as a (virtual) intermediate step.

For our case, we use both microwave and radio-frequency fields as sources of one photon each. For the case of coupling $|1, -1\rangle$ and $|2, 1\rangle$ as depicted in fig. 2.6, we proceed via the $|2, 0\rangle$ state as a virtual state at large detuning, and coupling with $|1, -1\rangle$ is done by microwave photon and $|2, 1\rangle$ by radio-frequency photon, respectively. This process should not populate $|2, 0\rangle$, the effective virtual state here, and one should use a detuning much larger than the coupling strength. The total Rabi frequency of the resonant two-photon

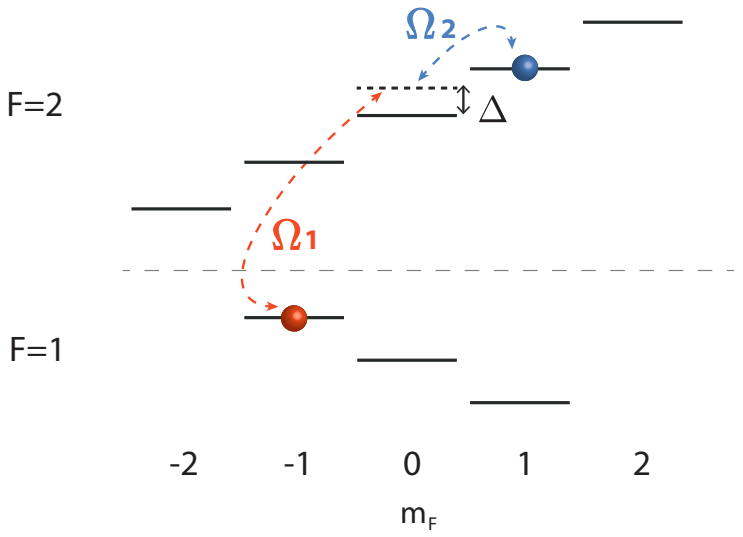

Figure 2.6: Two-photon transition. $|1,-1\rangle$ and $|2,1\rangle$ states are coupled by two-photon process, with the detuned virtual state $|2,0\rangle$. Ω_1 is the microwave photon coupling strength and Ω_2 is the RF photon coupling strength. Each of coupling is detuned by Δ from the resonance. Here the total coupling strength is given by $\Omega_{tot} = \Omega_1\Omega_2/2\Delta$.

transition is given by

$$\Omega_{tot} = \frac{\Omega_1\Omega_2}{2\Delta} \tag{2.6}$$

where Ω_i is the Rabi frequency of the i-th transition and Δ is the detuning from the intermediate state that is used as a virtual state.

2.2.5 Stern-Gerlach separation

With the experiments that manipulate the internal hyperfine states of the atom, it is crucial to detect each of their hyperfine states separately. To accomplish this, we use the Stern-Gerlach separation technique [122] (in combination with state-selective imaging) that gives a force at the beginning of the time of flight by spatially varying magnetic fields.

In practice, we use the same pair of large coils that is already used for MOT and the quadrupole magnetic trap (cf. sec.2.1). After the atoms are transferred from the magnetic trap to the optical trap in BEC preparation steps, we translate the coil about 1cm along the x-axis. Right after the time of flight step, we first rotate the bias magnetic field from the z-axis to the x-

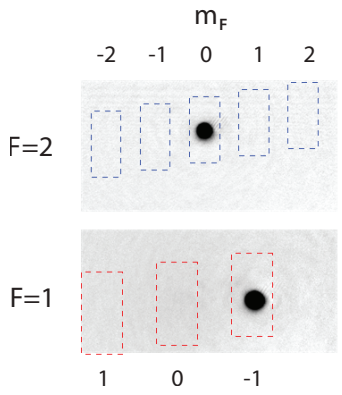

Figure 2.7: Stern-Gerlach separation. The magnetic field gradient that is applied at the beginning of the time of flight step gives a spatial separation of atoms depending on their hyperfine states. Blue and Red dotted box describes the position of atoms for each m_F state. Due to the different sign of g-factor, the arrange of sublevels for $F = 2$ and $F = 1$ is opposite.

axis using external Helmholtz coils around the science cell along x-axis. Then we apply the current to the large coils so that they generate a magnetic field gradient $\boldsymbol{B} = b_0 x\hat{x}$ to x-axis, where $b_0 \sim 100$ G/cm [113]. This provides forces depending on the internal hyperfine state since $\boldsymbol{F} = -\nabla V$ where the potential is from the Hamiltonian $\hat{H} = -\boldsymbol{\mu} \cdot \boldsymbol{B}$, which indeed gives

$$\boldsymbol{F} = -\mu_B g_F m_F b_0 \hat{x}. \tag{2.7}$$

This force gives a spatial separation of atoms in time of flight imaging depending on their hyperfine states. Since the force (in eq. 2.7) is proportional to the Landé g-factor, which has the opposite sign for $F = 1$ and $F = 2$ in ^{87}Rb, the direction of the separation for each F state depending on sublevels (m_F) is also opposite of each other.

2.3 Detection

It is crucial to conserve the information for the hyperfine state when detecting the atom at the end of each experiment. In our experiments, we are mainly using absorptive imaging technique with the combination of time of flight. We use resonant light on the $F = 2 \rightarrow F' = 3$ D_2 cycling transition to initially detect atoms at $F = 2$ states first (see fig. 2.2 for the transition).

Photons incident on atoms in $F = 2$ are scattered by resonant absorption, and this process creates a shadow of the atoms in the forward direction that is detected by a 16-bit CCD camera (Princeton PIXIS 1024B). By comparing the shadow with the background image that is taken in a later part of the time of flight sequence, we can extract the optical density of the atom with a proper calibration. Atoms in $F = 1$ are optically pumped into $F = 2$ states using repump light, and then imaged in the same way $\sim$ 3ms later.

In this imaging process, the CCD camera is taking 3 photos for the imaging of each state ($F = 2$ and $F = 1$); one image with the presence of the atom by shining in resonant light (I_a), the next image again after all atoms are vanished (I_0), and the last 'dark' image without illuminating the light (bkg), with $\leq 1\%$ non-linearity. The optical density (OD) for each camera pixel is then calculated as follows [122]:

$$OD = -ln\left(\frac{I_a - bkg}{I_0 - bkg}\right) \tag{2.8}$$

which gives the atom number $N = OD \times \sigma$ where σ is a calibration that depends on the measurement environment (pixel size, light polarization, field quantization direction, resonant scattering cross section, etc.) which is ~ 125 in our lab [113].

There are two modes that we can choose in our setup; these are 'normal' imaging and 'kinetic' imaging, and we typically use the 'kinetic' imaging method with the CCD camera. The normal imaging gives bigger region of interest, which is useful for the initial alignment. It is desired, however, to use the kinetic imaging for more accurate measurement since it provides better time resolution and a more precise optical density. Above all, Stern-Gerlach separation (cf. sec. 2.2.5) gives the same spatial separation for same m_F states for $F = 1$ and $F = 2$ (with opposite sign), so that we need to temporally separate states.

On kinetic imaging mode, after imaging $F = 2$ onto a partly covered CCD chip, the CCD camera pushes the image upward into the dark region and the same procedure is repeated for imaging $F = 1$ followed by another shift, taking the background image, and finally read-out of the chip. As a result, we obtain a set of 3 images for $F = 2$, $F = 1$ and background that are placed horizontally. Detecting the $F = 1$ states follows the sequence in 2.7ms additional flight. Since there is no resonant light that sends $F = 1$ to $F' = 3$, we first repump the $F = 1$ atoms by shining $F = 1 \rightarrow F' = 2$ laser. The atoms then spontaneously decay into $F = 2$ state, which is now qualified to follow the previous detection method. Here it is critical to fully separate two detections ($F = 2$ and $F = 1$), so that any remaining $F = 2$ atoms do not

contaminate the signal of the other.

2.4 Image analysis using principal components

Obtaining an accurate optical density (atom number) from the measured image (cf. sec.2.3) is very crucial. As mentioned before, we are measuring the shadow of the atom compared with the no-atom image which effectively minimizes the background noise by itself. In practice, however, there are some unwanted noises on the image, such as a circular fringes, which are generally caused by dust particles on optical elements in the path of the imaging light. Most of the noise that is static in time can be easily eliminated via our normal imaging process (cf. eq.2.8), but time-dependent (between the two images taken in a row) noise can give errors in the calculation of the optical density, because those fringes are also considered as the optical density if they are in the region of interest. This effect becomes more critical for the experiments that deal with relatively small atom number ($\lesssim 10^4$) which gives about the order of a few tens of atoms per pixel.

To overcome this issue, we use the technique of principal component analysis (PCA) which is described in detail in L. Krinner's thesis [113]. The authoritative description there is more principle-oriented and quantitative, we thus here explain the technique in a more qualitative way.

As a start, we here first briefly review the mechanism of PCA [128, 129]. PCA is an analysis technique that is widely used in large data processing for many purposes like image processing and compression due to its dimensionality reduction property. In our case, we use PCA to reconstruct clean images by removing noises that are learned from the references. To do this, we use principal components (PCs) that are extracted from a reference data set of many images taken without atoms, where each PC is a sequence of vectors in a real coordinate space. These principal components ($\boldsymbol{p}_i$) are unit vectors that are orthogonal to each other, and they are ordered by magnitude where each of components is in a direction that maximizes the variance of the data set. The first component $\boldsymbol{p}_1$ is the best fit to the data (in other word, minimizing the projection residual (the separation of data from the principal component), which maximizes the variance of the data that passes the center (cf. fig. 2.8 (C) bottom), whereas the second components $\boldsymbol{p}_2$ is the next best-fit that is orthogonal to $\boldsymbol{p}_1$. In this way, we can make a set of PCs that contains the most information (fringe pattern in our case) in a finite (and relatively small) number of components.

The mechanism of obtaining PCs is depicted in fig. 2.8. In our case, we use an empty image (reference image) as a data set, $\boldsymbol{R}_j$, (cf. fig. 2.8 (A))

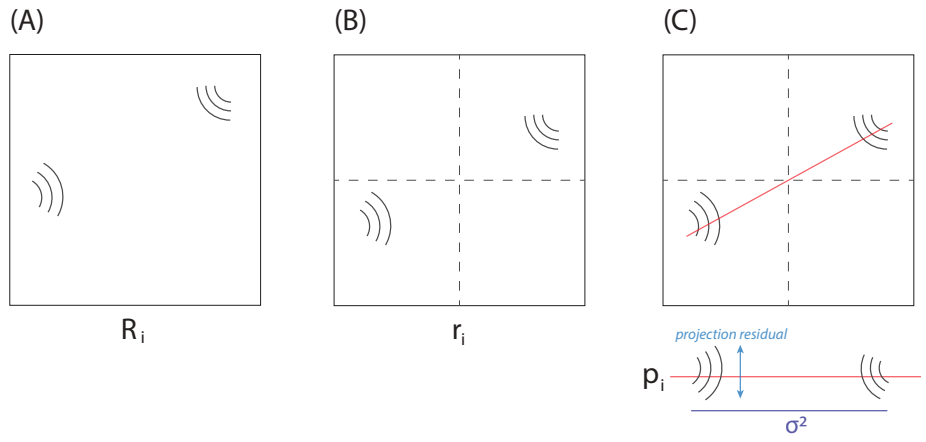

Figure 2.8: Mechanism of constructing principal component. (A) The schematic of the reference image with fringe, $\boldsymbol{R}_i$. (B) Centered image by subtracting the mean of the references $\boldsymbol{r}_j = \boldsymbol{R}_j - \sum_j \boldsymbol{R}_j/N$ (C) Principal component is given as the best fitting of the data that minimizes the projection residual. The bottom projection shows why it simultaneously maximizes the variance and minimizes the projection residual.

which contains the fringes that the analysis will study and remove later. Since our image is 2-dimensional, we make this into a 1-dimensional vector form by changing the basis $\{x, y\} \to x + \dim_x \times y$, where $\dim_x$ is a number of pixels of x-axis in the reference image. For simplicity, this process is not displayed in the figure.

From the set of N reference images $\boldsymbol{R}_j$, the mean reference image is extracted as $\boldsymbol{R} = \sum_j \boldsymbol{R}_j/N$. To perform PCA properly, we need to center the data, i.e. the mean of data should be zero (cf. fig. 2.8 (B)). For this, we now subtract the mean for the reference images to construct data set as

$$\boldsymbol{r}_j = \boldsymbol{R}_j - \boldsymbol{R} \tag{2.9}$$

From this $\boldsymbol{r}_j$, we extract the set of principal components p_i that follows the conditions above (cf. fig. 2.8 (C)). The variance (that is naturally maximized from the principal components) is given by $\sigma^2 = \frac{1}{N}\sum_i (\boldsymbol{d}_i \cdot \boldsymbol{p}_i)^2 = \frac{1}{N}(\boldsymbol{DP})^T(\boldsymbol{DP}) = \boldsymbol{P}^T\frac{\boldsymbol{D}^T\boldsymbol{D}}{N}\boldsymbol{P} \equiv \boldsymbol{P}^T\boldsymbol{V}\boldsymbol{P}$, where we use $\boldsymbol{D}$ as a component of data set in a convention of [113], N is a number of data vectors, and $\boldsymbol{V}$ is the covariance matrix with corresponding eigenvector $\boldsymbol{P}$. In practice, the construction of p_i is easily done by the in-built function of Mathematica;

`PrincipalComponents`[*table*] where *table* is the optical density data table of the reference image.

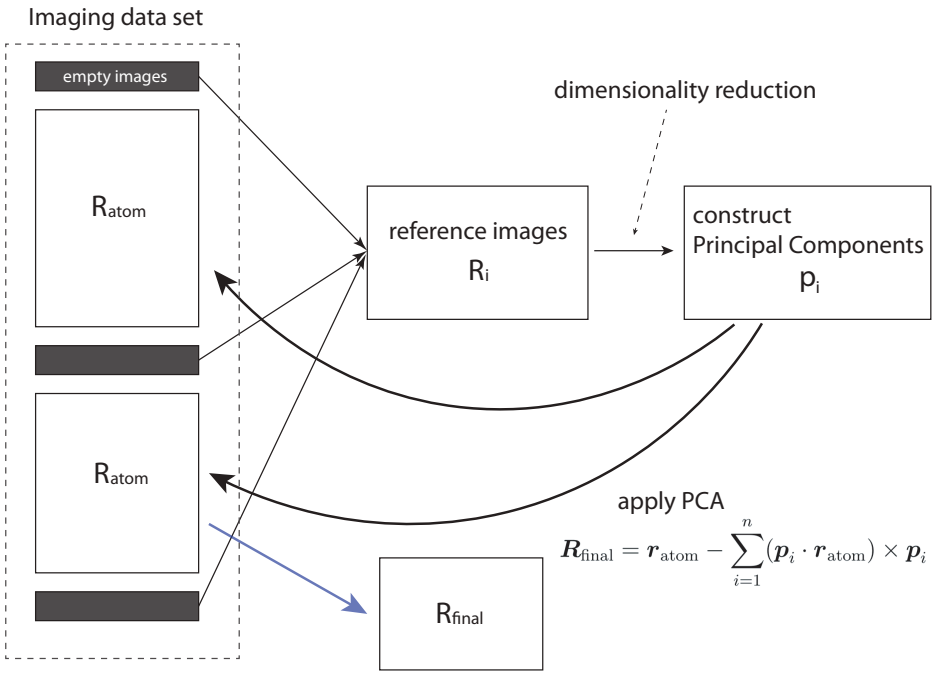

Figure 2.9: Image process steps for PCA. We take empty (atom-free) reference images between the measurements, typically more than ~ 40 in total. From the set of reference images, we extract the principal components for each ground F states. These components are applied to the equation eq. 2.10 to process the images we want to analyze ($\boldsymbol{R}_{\text{atom}}$), and we finally obtain the processed image $\boldsymbol{R}_{\text{final}}$. The number of principal components in use is typically small $n \sim 6$, to avoid over-fitting.

The next step is then applying the obtained principal components to the image that we want to process, which will get rid of fringes from an image with atoms by using the learned fringe pattern from the atom-empty images. Following the convention, we here denote $\boldsymbol{R}_{\text{atom}}$ as an image with atoms that we want to analyze. Since PCA requires the zero-mean data set, we here also subtract the mean of the reference images as $\boldsymbol{r}_{\text{atom}} = \boldsymbol{R}_{\text{atom}} - \boldsymbol{R}$. Then the overlapped part from the subtracted image is considered, only for first a few

principal components (typically $n = 6$ in this dissertation) as follows:

$$\boldsymbol{R}_{\text{final}} = \boldsymbol{r}_{\text{atom}} - \sum_{i=1}^{n} (\boldsymbol{p}_i \cdot \boldsymbol{r}_{\text{atom}}) \times \boldsymbol{p}_i \tag{2.10}$$

Here the subtracted image with atom is projected into the principal components. Note here that if an image contains a large number of atoms, the mean of the image with atoms is far from the zero which causes the error significantly. In this case, we need to consider the error subtraction. In short, one should put the 'mask' to screen out the region with atoms ($\boldsymbol{r}^m_{\text{atom}} = \boldsymbol{m} \times \boldsymbol{r}_{\text{atom}}$ where the 'mask' m is 1 (0) for the outside (inside) of the regions that contain the atoms), and process the analysis, that is discussed in detail in the thesis [113].

The practical flow of the image process is depicted in fig. 2.9. In practice, the reference image (empty atom image) is taken before and after the measurement to minimize the temporal changes between the PCA references and the processing data. We obtain these reference images simply by not loading atoms in MOT but repeating the rest of the same sequence as the other measurement, which is to make the same environmental effect that can be propagated from the sequence steps. Also for processing PCA, we re-adjust the region of interest (ROI) of the image properly. This is to zero the reference image that increases the validity of the process.

Fig. 2.10 shows the result of PCA with the actual measurement data used in our publication [88] (cf. chap. 5).

2.5 State-dependent potential

Making optical lattices in a standing optical wave is key for many of our ultracold atom experiments, which enables us to control the effective dimension of the system. In our lab, we typically make 1D systems that reveal much interesting physics not shown in 3D, by tightly confining the atoms with a far-detuned orthogonal 2D optical lattice in x-y dimensions. The D_2 ($5^2S_{1/2} \rightarrow 5^2P_{3/2}$) transition wavelength of ^{87}Rb is $\sim$ 780nm, so using 1064nm laser gives practically identical lattice tubes for all ground states of Rubidium atoms.

For the remaining 1D axis (z-axis in our lab), we choose a wavelength that is close to the resonance in order to provide the state-dependency. From the atom-light interaction, we can tune both amplitude and sign by choosing the proper combination of the laser and atomic hyperfine state pairs. In detail, this state-dependency is also related with the polarization of the laser and AC

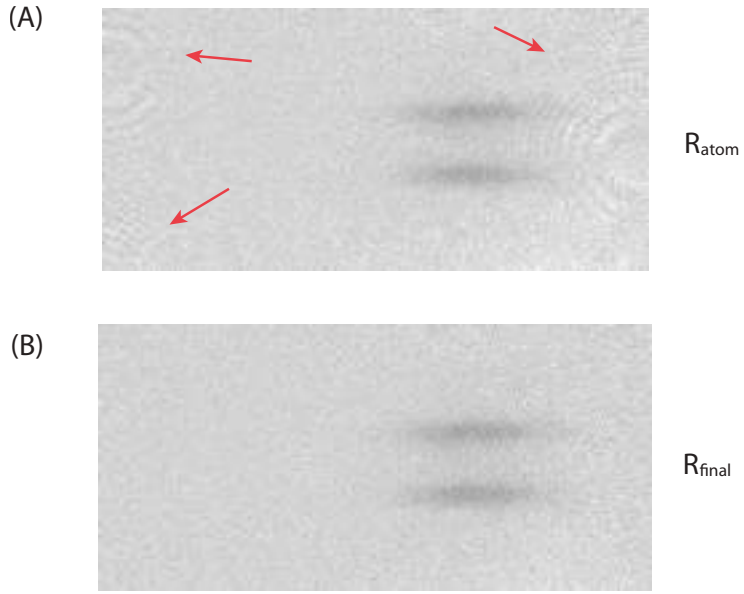

Figure 2.10: Image processed by PCA. (A) is the raw time of flight image $\boldsymbol{R}_{\text{atom}}$ and (B) is the processed image with PCA, $\boldsymbol{R}_{\text{final}}$. Red arrows in (A) marks the fringes, that are removed in the processed image (B). This data is used for the measurement of the onsite-interaction energy of matter-wave polariton (cf. chap. 5).

Stark shift [130, 131]. By ignoring the counter-rotating terms, we have [110]

$$U(\boldsymbol{r}, i, p) = \frac{3\pi c^2}{2}\left[\frac{\Gamma_{D_1}}{\omega_{D_1}^3}\sum_{l\in P_{1/2}}\frac{|c_p^{li}|^2}{\omega-\omega_{li}} + \frac{2\Gamma_{D_2}}{\omega_{D_2}^3}\sum_{l\in P_{3/2}}\frac{|c_p^{li}|^2}{\omega-\omega_{li}}\right] I(\boldsymbol{r}) \qquad (2.11)$$

where i indexes the initial hyperfine state, $\Gamma_{D_{1,2}}$ is the scattering rate of the $D_{1,2}$ transition, c_p^{li} is a Clebsch-Gordon coefficient between the initial and final hyperfine states, p denotes the polarization of the light, which may be $\sigma^{\pm}$ or π-polarized, and $I(\boldsymbol{r})$ is the intensity profile of the optical potential.

Fig. 2.11 shows the the optical potential of three different hyperfine states ($|2,-2\rangle$, $|1,-1\rangle$ and $|2,0\rangle$) for different polarizations (σ^-, π, σ^+) in the vicinity of the D_1 and D_2 resonance wavelength. Note that in order to obtain different lattice depths depending on the hyperfine states, circular polarization $\sigma^{\pm}$ is desired since the magnetic non-neutral hyperfine states ($m_F \neq 0$) experience different optical potential from the unmagnetic state ($m_F = 0$). Another

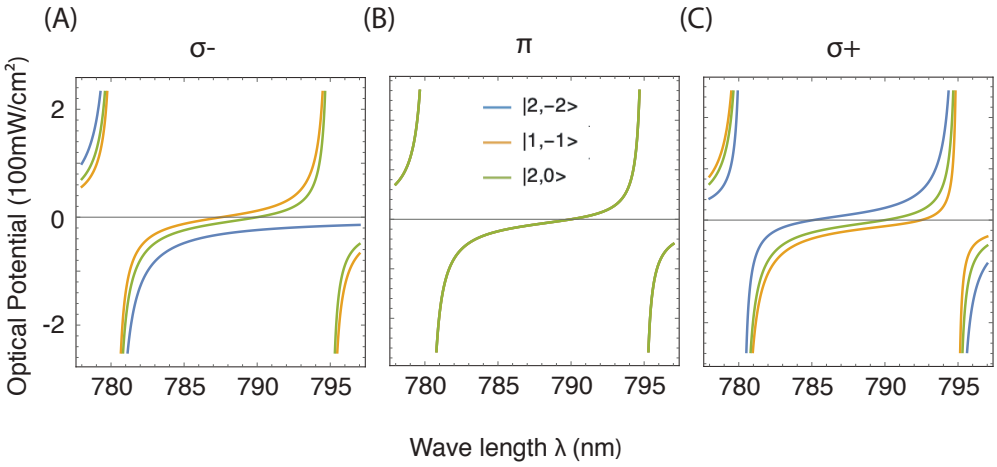

Figure 2.11: Optical potential for various polarizations (σ^-, π, σ^+ for (A,B,C)) is calculated with different hyperfine states ($|2,-2\rangle, |1,-1\rangle, |2,0\rangle$ for blue, orange and green curve, respectively). In a case of circular polarization (A,C), the magnetic hyperfine states ($|2,-1\rangle$ and $|2,1\rangle$) are tuned out in a different way at the wavelength between D_2 and D_1 line due to the opposite sign of the detuning. The magnetically insensitive state $|2,0\rangle$ is always tuned out at the same wavelength without any polarization dependence.

interesting point is that this magnetic neutral hyperfine state ($m_F = 0$) has the same energy shifts for all polarizations, and it does not matter whether $F = 1$ or $F = 2$ is used. Thus for providing the tunability for various lattice depths, it is natural to choose circular polarization, and we are using σ^- for the experiments in this dissertation.

From eq.(2.11), we can also study the wavelength dependence for different hyperfine states. The choice of the hyperfine state pair set is more critical for experiments with state-dependent lattices. With the proper choice of an atomic state pair, it is possible to set a 'tune-out' wavelength that only one of the two state sees the optical potential while the other does not. This is possible by virtue of the cancellation of couplings to the D_1 ($5^2S_{1/2} \rightarrow 5^2P_{1/2}$) and D_2 line of ^{87}Rb, 795nm and 780nm respectively. Our experimental range is between this blue-detuned (795nm) and red-detuned (780nm) wavelength so that we can control the the relative potential including its sign by shifting the wavelength. Fig. 2.12 (A) shows the optical potential in units of recoil energy depending on wavelength near the resonance for different ground states. Here we arbitrarily choose σ^- polarization. As discussed in previous section (cf. sec.2.2.5), due to the opposite sign of Landé g-factor between $F = 1$ and

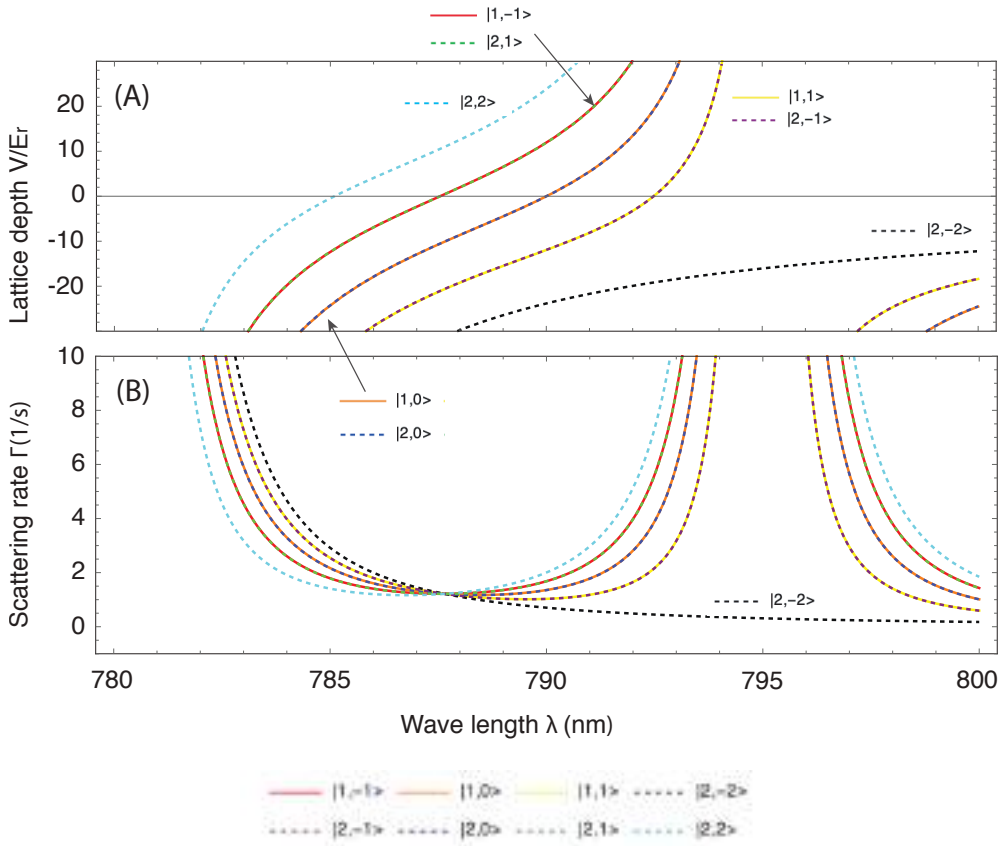

Figure 2.12: Optical potential for various hyperfine states. Lattice depth $s = V_{latt}/E_r$ is calculated with the circular polarization σ^-. Substates of $F = 1$ (solid) and $F = 2$ (dashed) show the opposite response against the wave length due to the sign of Landé factor, which gives perfect overlap for $|1, -1\rangle$ and $|2, 1\rangle$ as well as $|1, 1\rangle$ and $|2, -1\rangle$. (B) Corresponding scattering rate. The scattering rate diverges for most states for the wavelength < 785nm and > 792nm (cf. eq.2.12).

$F = 2$ state, $|1, -1\rangle$ and $|2, 1\rangle$ states give the same potential as well as $|1, 1\rangle$ and $|2, -1\rangle$. In our experiment, we choose the two states $|r\rangle = |F = 1, m_F = -1\rangle$ and $|b\rangle = |2, 0\rangle$, where $|b\rangle$ is tuned-out at the wavelength of $\lambda = 790.02$nm. This is consistent with the recent report for the precision measurement on tuned-out wavelength of Rubidium [132], which claims 790.01859(23)nm for $m_F = 0$ states.

When we use the state-dependent optical potential, it is very important to consider heating from spontaneous photon scattering. The scattering rate is

calculated by $\Gamma_{SC} = \Gamma U/\hbar\Delta$ with the eq.2.11 as follows [110]:

$$\Gamma_{SC} = \frac{3\pi c^2}{2}\left[\frac{\Gamma_{D_1}^2}{\omega_{D_1}^3}\sum_{l\in P_{1/2}}\frac{|c_p^{li}|^2}{(\omega-\omega_{li})^2} + \frac{2\Gamma_{D_2}^2}{\omega_{D_2}^3}\sum_{l\in P_{3/2}}\frac{|c_p^{li}|^2}{(\omega-\omega_{li})^2}\right] I(\boldsymbol{r}). \quad (2.12)$$

The scattering length for the same polarization σ^- is shown in fig. 2.12. The scattering rate diverges for most states for the wavelength $<$ 785nm and $>$ 792nm, due to the D_1/D_2 transition. The scattering rate at 790nm is on the order of one per second ($\Gamma_{SC} = 1.68s^{-1}$ for $|1,-1\rangle$ and $1.35s^{-1}$ for $|2,0\rangle$ at the intensity of 150W/cm^2 that gives $s_z \sim 20E_r$) which is negligibly long compared with our experimental time scale $\lesssim$ 10ms.

With all the techniques described above, we are now ready to explore more specialized directions of ultracold atomic physics. Especially the summary in chapter 4 and the research described in chapter 5 are works based on the techniques above.

Chapter 3

Theoretical concepts

In this chapter, we discuss same fundamental concepts for studying interacting quantum gases in optical lattices. These concepts are particularly relevant for the description of our experiments with matter-wave polaritons (cf. Chap. 5).

3.1 Band structure in optical lattices

In periodic potentials, the motion of a particle is strongly influenced by quantum-mechanical tunneling. We here first see how we obtain a band structure in optical lattices. Since most of the experiments in this dissertation deal with 1D geometries, we will simply solve the system in 1D.

We start with the Hamiltonian for a single atom in a 1D optical lattice:

$$\hat{H} = -\frac{\hbar^2\nabla^2}{2m} + V_0 \sin^2(k_z z) \tag{3.1}$$

where $k = 2\pi/\lambda$ is the wavenumber and λ is the wavelength of the lattice.

In case of a single particle in a periodic potential $V(z+Z) = V(z)$, where Z is an integer multiple of $\lambda/2$, the eigenfunction of the Hamiltonian is given by a Bloch wave as the product of a plane wave and a periodic function [133]

$$\phi_q(z) = \mathrm{e}^{iqz} u(z) \tag{3.2}$$

where q is the quasi-momentum and $u_q(z)$ is a function with the periodicity of the lattice. Sometimes, it is useful to use the eigenfunction in another form as follows:

$$\phi_q(z+Z) = \mathrm{e}^{iqZ} u_q(z) \tag{3.3}$$

for every Z in a Bravais lattice. Here, from the properties of the optical lattice, we can naturally define some basic parameters.

In a microscopic point of view, the confinement of the atom in the optical lattice arises from the continuous absorption and stimulated emission of the photon momentum. Thus there is an energy scale that the atom in the optical lattice naturally brings, the so-called 'recoil energy',

$$E_r = \frac{\hbar^2 k^2}{2m} \tag{3.4}$$

where k is the recoil momentum and $d = \lambda/2 = \pi/k$. Typically we express E_r in units of $h\times$ kHz.

The lattice depth can then be expressed in units of the recoil energy, as $s = V_0/E_r$ where V_0 is the amplitude in eq. 3.1. When $s \gg 1$, the system is called 'tightly confined' so that there is very little natural tunneling from lattice site to site, when measured on the time scale $\hbar/E_r$. The harmonic oscillator length a_{ho} can be also defined in terms of s, as

$$a_{\text{ho}} = \sqrt{\frac{\hbar}{m\omega_{\text{ho}}}} = \sqrt{\frac{\hbar}{2m\omega_r}} s^{-1/4} \tag{3.5}$$

where $\omega_{\text{ho}} = 2\omega_r\sqrt{s}$ and $\omega_r = E_r/\hbar$ is the recoil frequency.

Since the system is periodic, we can solve the Hamiltonian by only looking at the first Brillouin-zone $[-k, \cdots, k]$. Depending on the properties of the single atom and its confining potential, the energy eigenvalue $\varepsilon_n(q)$ is continuous in certain energy ranges which form the energy bands with index n. The Bloch waves are then written as $\phi_q^{(n)}(z)$. The regions between the separated bands where no eigenvalue for Hamiltonian exists are called band-gaps.

The general dispersion relation expressed in the first Brillouin-zone is shown in fig. 3.1. Two extreme cases are very easy to catch here. In case of a free particle where $V_0 = 0$ as in fig. 3.1 (A), there is no bandgap and the energy is continuous. In the case of a deep lattice where $s \gg 1$ (see fig. 3.1 (C)), the ground energy band is very flat, approaching the energy of the harmonic oscillator ground-state, with a diverging effective mass $m^* = \hbar^2(\partial^2 E/\partial k^2)^{-1}$. For most cases where the confining potential is finite, however, a level splitting exists at the band edge, in analogy to an avoided crossing, and a bandgap is induced (see fig. 3.1 (B)).

When the lattice is deep enough, it is convenient to represent the system using localized wavefunctions, the so-called Wannier functions (discussed in detail at sec.3.1.1). This is particularly true when motion is confined to the ground band, $n = 1$. In this case, the Wannier function localized at site j with

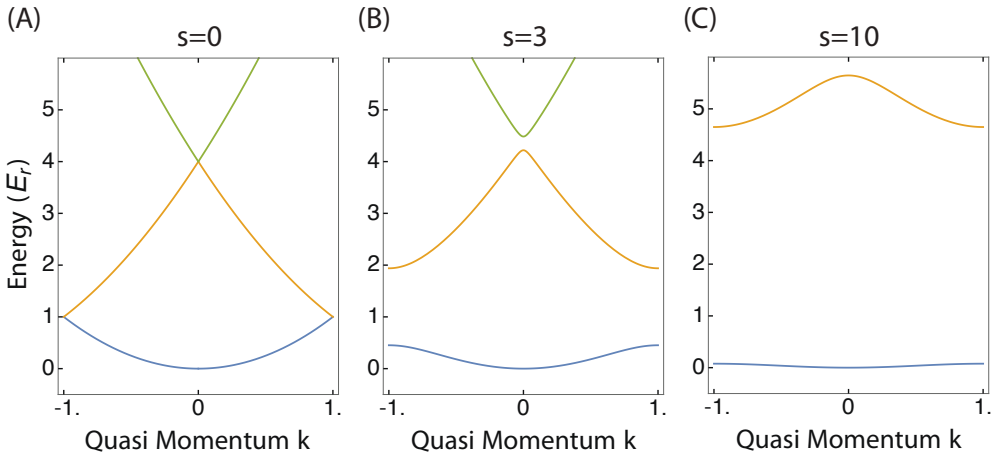

Figure 3.1: Energy band structure for 1D lattice system with different lattice depths ($s = V_{latt}/E_r = 0, 3, 10$ for (A, B, C)). The energy bands are plotted in the first Brillouin-zone. The dispersion is expressed in quasi-momentum $k = \pi/d$ where $d = \lambda/2$, and energy E_r.

position x_j can be calculated by the Bloch waves as

$$w(x - x_j) = \frac{1}{\sqrt{N}} \sum_q \phi_q^{(1)}(x - x_j) = \frac{1}{\sqrt{N}} \sum_q \exp^{-iqx_j} \phi_q^{(1)}(x - x_j) \tag{3.6}$$

where N is a normalization constant (number of sites).

The tunneling between neighboring sites is determined by the overlap of adjacent Wannier functions,

$$t = \langle w(z)| \hat{H} |w(z + d)\rangle \tag{3.7}$$

where $\hat{H}$ is the system Hamiltonian and $w(z)$ is the Wannier function at position z. This will be discussed in more detail below section. We note that t can also be calculated from the width $[\varepsilon_1(k) - \varepsilon_1(0)] = w_1$ of the ground band as $t = w/4$.

3.1.1 The tight-binding limit

In our optical lattice, especially in the case of 1D, the tight-binding approximation is very useful for understanding the dynamics of localized atom. It is generally applicable when the leakage of the Wannier functions into neighboring sites is not too large (i.e. the Wannier functions are approximately

harmonic-oscillator ground state) but also not too small to neglect the correction to the picture of isolated sites.

In detail, we first consider the single particle Hamiltonian of a full periodic crystal is given as

$$H = H_{at} + \Delta U(z) \tag{3.8}$$

where H_{at} is the Hamiltonian of the fully localized single atom, and $\Delta U(z)$ contains all corrections to the potential due to its sinusoidal nature, beyond the harmonic approximation. We can assume that $\Delta U \to 0$ at the center of each site. Under the assumption that the full periodic Hamiltonian H can be approximated as H_{at} [133], we have

$$H_{at}\psi_n = E_n\psi_n \tag{3.9}$$

where $\psi_n(z)$ is localized in each lattice site, E_n is the energy of the n-th energy level of a localized atom. In this case, we have a very small overlap integral γ_n,

$$\gamma(Z)_n = \int dz\, \psi_n^*(z) H \psi_n(z - Z). \tag{3.10}$$

We now want to make the connection between these localized wavefunctions to the Bloch waves. To do this, recall here the Bloch condition eq.3.3; we want to satisfy the condition for N linear combinations, which gives

$$\phi_q(z) = \sum_Z \mathrm{e}^{iqz}\psi(z - Z) \tag{3.11}$$

where $\psi(z)$ is indeed a Wannier function of eq.3.6, which can be expanded as a sum of localized orbital wave functions

$$\psi(z) = \sum_n b_n \psi_n(z) \tag{3.12}$$

which is not necessarily a stationary-state wave function. The validity of this approximation mainly relies on following two assumptions. The first one is an assumption of small overlaps (γ_n) as stated above, and the second one is the small correction of the potential at large distance from center [133], say

$$\sum_n \left(\int \psi_m^*(z) \Delta U(z) \psi_n(z) dz \right) b_n \ll (\varepsilon(k) - E_m) b_m \tag{3.13}$$

where Bloch energy $\varepsilon(k)$ is the eigenvalue of the total Hamiltonian $H = H_{at} + \Delta U(z)$ and k is a wavevector.

We now discuss the difference of the Wannier function from the tight-binding atomic function. The Wannier functions at different sites are orthogonal which is not the case for the other, and the complete set of the Bloch wave can be expressed as the set of Wannier functions and vise versa.

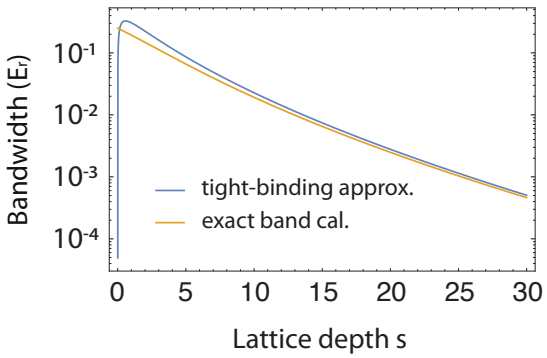

Figure 3.2: Calculated band width from the tight-binding approximation and exact band calculation (from Mathieu function). For low depth, the tight-binding model fails due to the invalid assumption. As the lattice gets deeper, the model converges to the exact model.

In the tight-binding regime, we can calculate the dispersion of the lowest Bloch band, where the bandwidth is given as [134]

$$4J = \frac{4}{\sqrt{\pi}} s^{3/4} \exp\{-2(s)^{1/2}\} \tag{3.14}$$

where J is the tunneling coefficient and $s = V_{latt}/E_r$ is the lattice depth. This is a good approximation in large order, but it is always better to calculate the bandwidth from the exact band structure analytically from the Mathieu function for example [134], see fig. 3.2.

3.2 Bose-Hubbard model

A BEC in the optical lattices is a great platform to study experimentally the Bose-Hubbard Hamiltonian (BHM) [50]. Based on the experimental implementation of the BHM, the transition from superfluid (SF) to Mott-insulator (MI) [135] has been studied experimentally [49, 136] which opened up new possibilities toward the use of ultracold atoms as test-bench for theoretical models from solid state physics.

In case of interacting scalar bosons, with the atom-atom contact interaction $V_{col}(x) = g\delta(x)$, the Hamiltonian in second quantization can be expressed as

$$\hat{H} = \int d^3r[\hat{\psi}^\dagger(\boldsymbol{r})(\frac{\hbar^2\nabla^2}{2m} + V)\hat{\psi}(\boldsymbol{r}) + \frac{g}{2}\hat{\psi}^\dagger(\boldsymbol{r})\hat{\psi}^\dagger(\boldsymbol{r})\hat{\psi}(\boldsymbol{r})\hat{\psi}(\boldsymbol{r})], \tag{3.15}$$

where g is the coupling constant from the atom-atom collision $g = 4\pi\hbar^2 a_s/m$, a_s is the s-wave scattering length, and $\hat{\psi}^\dagger(\boldsymbol{r})$ and $\hat{\psi}(\boldsymbol{r})$ are the creation and annihilation operators of the bosonic field.

Here we can expand the field operator $\hat{\psi}^\dagger(\boldsymbol{r})$ in the basis of Wannier function as

$$\hat{\psi}^\dagger(\boldsymbol{r}) = \sum_{j=1} \hat{a}_j^\dagger w_j(\boldsymbol{r}) \tag{3.16}$$

where $w_j(\boldsymbol{r}) = w(\boldsymbol{r} - \boldsymbol{r}_j)$ is the localized Wannier function and $\hat{a}_j^\dagger$ is the creation operator for boson on site j.

Then by defining the tunneling coefficient J and on-site interaction energy U as

$$J = J_{i,j} = -\int d^3r\, w_i^*(\frac{\hbar^2\nabla^2}{2m} + V)w_j, \tag{3.17}$$

$$U = g\int d^3r\, w_i^* w_i^* w_i w_i, \tag{3.18}$$

the Hamiltonian can be rewritten as

$$\hat{H} = -J\sum_{<i,j>} \hat{a}_i^\dagger \hat{a}_j + \frac{U}{2}\sum_j \hat{n}_j(\hat{n}_j - 1), \tag{3.19}$$

where $\hat{n}_i = \hat{a}_i^\dagger \hat{a}_i$ is the number operator.

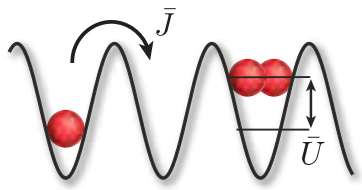

Figure 3.3: Illustration of the Bose-Hubbard Hamiltonian schematic. J is the tunneling between the lattice sites and U is the onsite-interaction energy.

With the consideration of the chemical potential of the system, we indeed

have the Bose-Hubbard Hamiltonian as

$$\hat{H}_{\mathrm{BH}} = -J \sum_{<i,j>} \hat{a}_i^\dagger \hat{a}_j + \frac{U}{2} \sum_j \hat{n}_j(\hat{n}_j - 1) - \mu \sum_j \hat{n}_j \tag{3.20}$$

where J is the tunneling between the lattice sites and U is the onsite-interaction energy. Note that μ fixes the atom number in a trap. Fig. 3.3 shows a Bose-Hubbard Hamiltonian schematic.

3.2.1 Mean-field treatment and quantum phase transition

The BHM carries interesting many-body physics emerging from the presence of collisional interactions. The quantum phase transition between the superfluid and Mott-insulator is one of the most significant observations that has been achieved in the optical lattice context. To find an approximate phase diagram, we first apply the assumption of mean field approximation [137–140], which averages out the all effects from each individual atom. Then the many-body problem turns effectively into a one-body problem.

In detail, let's first take a look how the two extreme regimes for competing parameter ratios give each quantum phase. For the weakly interacting regime, $J \gg U$, the interaction is negligible and atoms are all in same phase. Here atoms occupy the lowest kinetic energy state as

$$|\psi\rangle = \frac{1}{N!}(a_{k=0}^\dagger)^N |0\rangle \tag{3.21}$$

where N is a total atom number, $|0\rangle$ is a vacuum state, and the operator $a_k^\dagger$ creates a particle with momentum k (eq.3.20). This eq. 3.21 is a coherent (superfluid) state, and we can express it alternatively as a sum of the atoms at all lattice sites as

$$|\psi_{SF}\rangle = \frac{1}{N_{\mathrm{site}}} \sum_i a_i^\dagger |0\rangle \tag{3.22}$$

where i is a site index.

For the strongly interacting regime, $J \ll U$, we can neglect J so that the Hamiltonian eq.3.20 gives

$$\hat{H} = \frac{U}{2} \sum_j \hat{n}_j(\hat{n}_j - 1) - \mu \sum_j \hat{n}_j \tag{3.23}$$

in which all lattice sites are isolated from each other. In each individual site

with n atoms, the energy is then given as

$$E_n = -n\mu + \frac{U}{2}n(n-1). \tag{3.24}$$

Thus the energy states are separated and gapped, which gives a stable state against small perturbation like small tunneling, which is a Mott state. Note here that this Mott state only has an integer filling n. The eigenfunction of the Mott state can be represented as

$$|\psi_{\mathrm{MI}}\rangle \propto \frac{1}{N_{site}} \prod_i (a_i^\dagger)^{N/N_{\mathrm{site}}} |0\rangle \,. \tag{3.25}$$

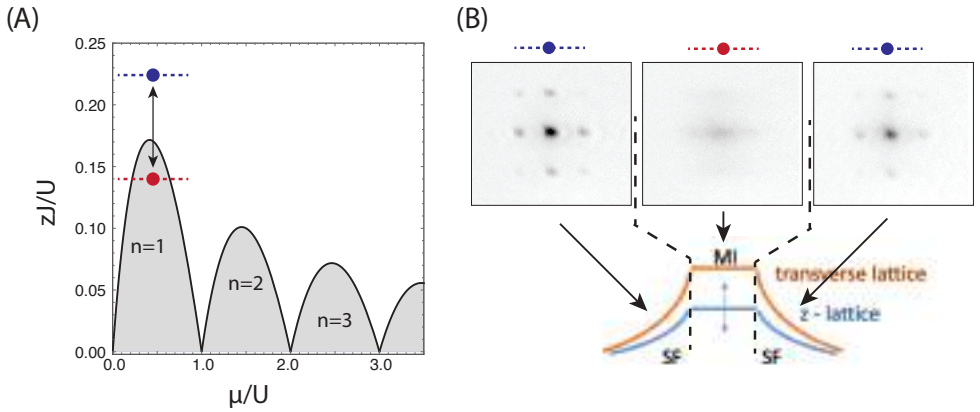

Figure 3.4: Quantum phase transition. (A) Phase diagram plotted as a function of the chemical potential μ and a scaled tunneling coefficient zJ where z is a number of the nearest neighbor sites, both are scaled by the interaction energy U. The colored areas are Mott-insulating regions whereas the white area is the superfluid region. Mott-insulating regions are limited to integer n which is an atom number per site. (B) Quantum phase transition in the experiment. By ramping up and down the confined lattice in all 3 axes, the system experiences superfluid-Mott insulator-superfluid transition. Red and blue dashed line above the time of flight image roughly remarks the regime where the system is, corresponding to the phase diagram in (A). For the superfluid regime, the data (left and right) are taken 15ms before (and after) the lattice depths reach the maximum (middle, $s_\perp = 18E_r$, $s_z = 10E_r$) which gives about half of maximum lattice depths.

Fig. 3.4 (A) is a phase diagram plotted as a function of the chemical potential μ and a scaled tunneling coefficient zJ, both are scaled by the interaction

energy U. Here z is a number of the nearest neighbor sites which is 2 in a 1D system. The Mott-insulator region is colored in grey, and each lobe corresponds to the the integer number n which is an atom number per each site. The rest area of white represents the superfluid regime.

In the case of a trapped BEC, there is a mean-field potential that is calculated from the Gross-Pitaevskii equation as [141]

$$\mu_0 = \frac{\hbar\omega_{\rm ho}}{2}\left(\frac{15Na_s}{a_{\rm ho}}\right)^{2/5} \tag{3.26}$$

where N is the total atom number, $\omega_{\rm ho} = (\omega_x\omega_y\omega_z)^{1/3}$ is the mean harmonic trapping frequency, $a_{\rm ho} = \sqrt{\hbar/m\omega_{\rm ho}}$ is the mean harmonic oscillator length.

For a large number of atoms where the kinetic energy ($\propto N$) is negligibly smaller than the interaction energy ($\propto N^2$), we can use 'local chemical potential '

$$\mu(z) = \mu_0 - \frac{1}{2}m(\omega z)^2 \tag{3.27}$$

where the chemical potential is given by the peak density of condensate, which is called local-density approximation or Thomas-Fermi approximation. This approximation is generally valid in the center region, but fails at the boundary of the atomic cloud where sharp density profile exists.

Fig. 3.4 (B) illustrated a typical experimental observation of the superfluid $\rightarrow$ Mott-insulator $\rightarrow$ superfluid transition, which is done by changing the effective tunneling coefficient J by ramping up and down the confining lattice depths in all 3D axes. A time of flight image is taken which gives the coherence of the system from the diffraction peaks. In the superfluid regime, the diffraction pattern displays clearly visible peaks. In contrast, in the Mott-insulator regime, the incoherence of the wave function from each site averages out the diffraction and what left is a diffuse blurb centered around 0 in momentum space. While the transition can also be seen by only changing the lattice depth in 1D, here we changed all 3 lattices to observe clear diffraction in both horizontal and vertical axes, following the sequence in [83]. When the lattice depth is low in the beginning (B, left), the wave functions on each site are still coherent and the system is in the superfluid regime, which is depicted as a blue dashed line in a phase diagram fig. 3.4 (A). As the lattices get deeper and all wave functions are tightly confined in each site, the time of flight image becomes diffuse due to the loss of coherence (B, middle). This is the case of the red dashed line in (A); a deep lattice decreases the tunneling coefficient J which displaces the blue line down to the red line as depicted. As the lattices get shallower again, the system recovers coherence (B, right) and as a result,

the time of flight pattern is again comparable with the initial state. Note here that the system in phase diagram is represented as a line, which is due to the inhomogeneity of the system.

In general, it is relatively easy to control the total atom number, but it is impossible to achieve uniform μ over the size of the sample due to the harmonic optical trap. Thus depending on the structure of the chemical potential, the density distribution of the atom gives well-known 'wedding-cake' shape [50, 142, 143]; highest density with integer n at the center and layered by lower n to the side and they give plateaus (Mott regime), meanwhile the space between layers is filled by a smoothly varying density (superfluid regime).

The theoretical concepts described in this chapter are applied to analyze experimental results in Chapter 5. Especially fig. 3.4 is directly related to the phase transition that is experimentally observed.

Chapter 4

The matter-wave platform

To discuss the main topic of this dissertation on the formation of matter-wave polaritons in chapter 5, it is crucial to understand our matter-wave platform. This chapter gives a short review of the approach and detail results detailed in our publication *Spontaneous emission of matter waves from a tunable open quantum system*, Ludwig Krinner, Michael Stewart, Arturo Pazmiño, Joonhyuk Kwon, Dominik Schneble, Nature, **559**, 589 (2018) [86] (sections 4.3 and 4.4) and our publication *Dynamics of matter-wave quantum emitters in a structured vacuum*, Michael Stewart, Joonhyuk Kwon, Alfonso Lanuza, Dominik Schneble, Phys. Rev. Res. **2**, 043307 (2020) [87] (sections 4.3 and 4.5). Details can be found in the PhD theses of Ludwig Krinner [113] and Michael Stewart [115].

4.1 Introduction

The spontaneous photon emission into the vacuum due to the decay of an excited atom is very sensitive to the density of states of the radiation field. Depending on whether the emission is into free space or structured vacuum, the emission behavior can be dramatically different. Here, one of the most interesting phenomena is the formation of the atom-photon bound state [107, 144, 145] in photonic bandgap systems [90, 146, 147].

We demonstrated a platform that is analogous to an atom in a photonic bandgap material, and in which the photon is replaced with a matter-wave. With our ultra-cold atom system, we can tune the vacuum coupling and excitation energy freely, providing us with a direct measurement of the atomic bound-state. Moreover, depending on the relative amplitude between the vacuum coupling and the coupled bandwidth, the system exhibits the transition from Markovian decay to the fully non-Markovian dynamics, which

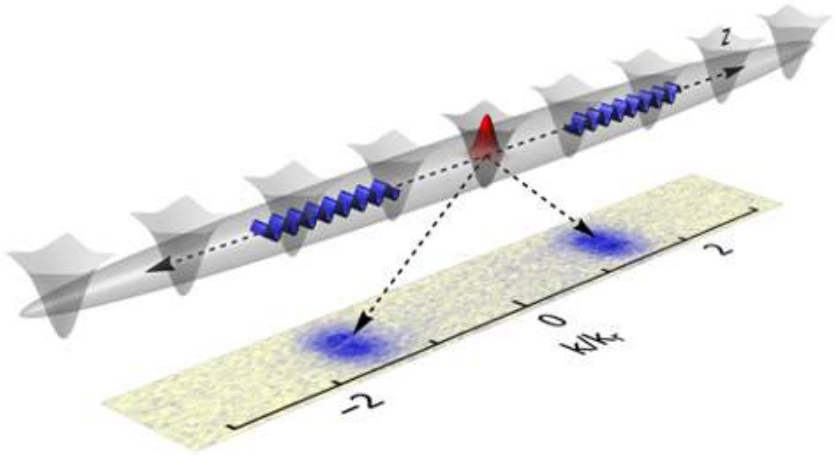

Figure 4.1: Schematic illustration of the quantum-emitter platform [86]. The quantum emitters (gray wells) contain $|r\rangle$ (red) atoms that are tightly confined with the state-selective optical potential. With a microwave coupling (coupling strength Ω, detuning Δ), $|r\rangle$ atoms undergo a transition to the emitted matter-wave states $|b\rangle$ (blue), which are free to propagate along the 1D tube. The momentum distribution of emitted $|b\rangle$ atoms is observed in time of flight image as shown in figure, depending on the excitation state energy of the quantum emitter. There is a natural left/right symmetry in the momentum space.Illustration adapted from Krinner et al., Nature **559**, 589 (2018) [113].

gives the demonstration of the transition from spontaneous decay as the Rabi-oscillation.

4.2 Theory: Weisskopf-Wigner model

Spontaneous emission, leading to the irreversible decay in quantum mechanics, can be described by the Weisskopf-Wigner Model [89]. In quantum optics, we consider a two-level system characterized by the excited and the ground state that is coupled to the vacuum. The atom starts out with the excited state $|e\rangle$ and spontaneously decays into $|g\rangle$. Here we review the standard description, and we will make connection to our system. The detailed approach is also well described in textbooks such as [148, 149] and in the PhD thesis of L. Krinner [113].

To begin with, we start with the Hamiltonian of a particle under the clas-

sical electromagnetic field as

$$\hat{H} = \frac{(\boldsymbol{p} - q\boldsymbol{A})^2}{2m} + V(\boldsymbol{r}) \tag{4.1}$$

where q is the particle charge, A is the vector potential and V is the scalar potential. With the assumption of the Coulomb gauge ($\nabla \cdot \boldsymbol{A} = 0$), and for a single-electron atom, i.e. $q = -e$, we have our Hamiltonian

$$\hat{H} = \hat{H}_0 + \frac{e}{m}\boldsymbol{A} \cdot p = \hat{H}_0 + \hat{H}_I \tag{4.2}$$

where $\hat{H}_0 = \frac{\boldsymbol{p}^2}{2m} + V(\boldsymbol{r})$ is the atomic and $\hat{H}_I$ is the interaction Hamiltonian. Under the dipole approximation ($\boldsymbol{k} \cdot \boldsymbol{r} \approx 0$) and the assumption that only two states are coupled, we can indeed obtain the transition matrix element of $\hat{H}_I$ [149] as

$$\hat{H}_I = -i \langle g | \hat{\boldsymbol{d}} | e \rangle \boldsymbol{\varepsilon}_{k,s} \boldsymbol{E} \tag{4.3}$$

in two-level system where $\varepsilon_{k,s}$ is the polarization vector of the photon and $\boldsymbol{E} = -\frac{\partial}{\partial t}\boldsymbol{A}$ is the classical electric field.

Now we can apply the above with the Hamiltonian of two-level system with the excited state $|e\rangle$ and the ground state $|g\rangle$ in a quantized electromagnetic vacuum,

$$\hat{H} = \hbar\omega_0 |e\rangle \langle g| + \sum_{\boldsymbol{k},s} \hbar\omega_{\boldsymbol{k}} (\hat{b}^\dagger_{\boldsymbol{k},s} \hat{b}_{\boldsymbol{k},s} + \frac{1}{2}) + \hat{H}_I \tag{4.4}$$

where $\hbar\omega_0$ is the excited state energy, $\hbar\omega_{\boldsymbol{k}}$ is the energy of the photon with the wave-vector $\boldsymbol{k}$, s is the polarization state and $\hat{b}^\dagger$ ($\hat{b}$) is the creation (annihilation) operator of a single excitation (i.e. photon) with given wave-vector and polarization. Here the last term of 4.4 is again the interaction Hamiltonain that couples the excited atom and the excitation (photon) mode as

$$\hat{H}_I = \sum_{\boldsymbol{k},s} (-\hbar g_{\boldsymbol{k},s} \hat{b}^\dagger_{\boldsymbol{k},s} |g\rangle \langle e| + H.c.). \tag{4.5}$$

Here $g_{\boldsymbol{k},s}$ is the interaction strength between the excited state and the ground state, which is given by [149]

$$g_{\boldsymbol{k},s} = -iE_0 \boldsymbol{\varepsilon}_{\boldsymbol{k},s} \langle g | \hat{\boldsymbol{d}} | e \rangle \tag{4.6}$$

with the (zero-point) vacuum field $E_0 = \sqrt{\hbar\omega_{\boldsymbol{k}}/2\epsilon_0 V}$, where ϵ_0 is the permittivity of free space and V is system volume.

The interaction Hamiltonian 4.5 provides the basic description of spon-

taneous decay under the Weisskopf-Wigner Hamiltonian; by de-exciting the excited state into the ground state, an excitation distributed over all accessible modes is generated by the creation operators $\hat{b}^{\dagger}_{\boldsymbol{k},s}$. This can be seen more clearly by the general solution of the time-dependent Schrödinger equation $i\hbar\partial_t |\Psi(t)\rangle = \hat{H} |\Psi(t)\rangle$ as

$$|\Psi(t)\rangle = A(t)e^{-i\omega_0 t} |e,0\rangle + \sum_{\boldsymbol{k},s} B_k(t)e^{-i\omega_{\boldsymbol{k}} t} |g,1_{\boldsymbol{k},s}\rangle \tag{4.7}$$

where $|e,0\rangle$ is the state having excited atom without photon and $|g,1_{\boldsymbol{k},s}\rangle$ is the state having ground state with a single photon with given wave-vector and polarization. Putting this ansatz into the Schrödinger equation gives the following equation directly

$$\dot{A}(t) = i\sum_{\boldsymbol{k},s} g^{*}_{\boldsymbol{k},s} e^{-i(\omega_{\boldsymbol{k}}-\omega_0)t} B_{\boldsymbol{k},s}(t) \tag{4.8}$$

$$\dot{B}_{\boldsymbol{k},s}(t) = ig_{\boldsymbol{k},s} e^{i(\omega_{\boldsymbol{k}}-\omega_0)t} A(t) \tag{4.9}$$

with the initial condition $A = 0|_{t=0}$ and $B_k = 0|_{t=0}$ which means that the system starts with the initially excited atom state.

Details for obtaining the analytic solution above is well-described in [150] and in the PhD thesis of Michael Stewart [115]. In the usual Markovian approximation, we assume that $A(t)$ in eq. 4.8 varies slowly in time which enables to take $A(t)$ out of the time-integral while solving analytically, and it gives an exponential decay.

4.3 Experimental platform

Two of our prior publications that we will briefly review in the following sections (sec.4.4, sec.4.5) share almost the same experimental platform. Most of the universal features of our matter-wave emission experiments were already described in [86]. Here we review some of the special experimental techniques that make our measurements possible.

4.3.1 Magnetic field stablization

Magnetic field tagging [151]

Changes of magnetic field directly affect the spacing between different m_F sublevels and the absolute detuning which indeed changes the excitation energy. We thus need to characterize and stabilize the field as much as possible.

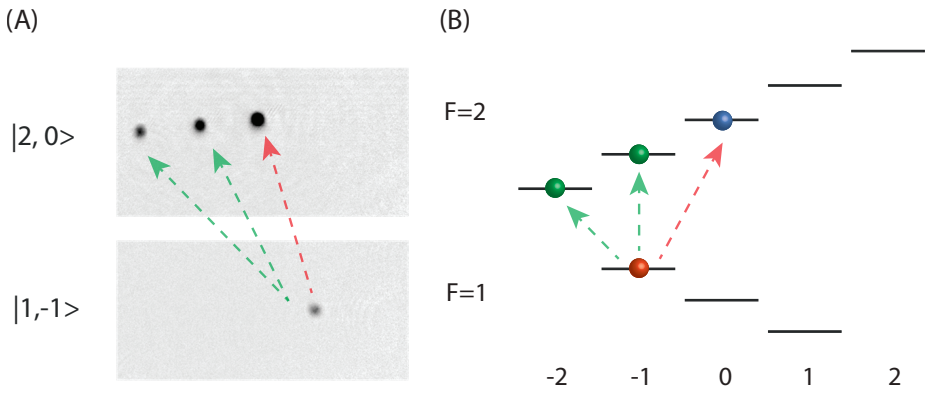

Figure 4.2: Magnetic field tagging. (A) Time of flight images of 2−way field tagging. Starting from $|1,-1\rangle$ the target experiment transfer atoms to $|2,0\rangle$, and the leftover population at $|1,-1\rangle$ state is used as a field tag by transferring to $|2,-1\rangle$ and $|2,-1\rangle$ states. (B) Schematic illustration of 2−way field tagging in energy level diagram.

Generally, one of the most direct ways to characterize magnetic fields at the position of the atoms is to use the atomic cloud itself as a field sensor. For an optically trapped BEC, we measure the Rabi spectrum. By taking a number of (typically 6) different data points around the resonance frequency, we can calculate and fit the Rabi frequency of the coupling and corresponding magnetic field. The shortcoming of this method is, however, that the measurement is not on-time with the experimental data. Since each of this measurement is destructive, there is a temporal gap about $30 \times 6 = 180$s between when the data is taken and when the calibration is done. Thus we would better know the exact magnetic field when the data has taken, and the magnetic field tagging technique (described in [151] and L. Krinner's thesis in detail) provides it.

Fig. 4.2 shows the mechanism of 2−way magnetic field tagging. When the experiment (between $|1,-1\rangle$ and $|2,0\rangle$) is done, the information we generally want to obtain for the experiments in this section is mostly the population of each state and the momentum distribution of the emitted "blue" ($|2,0\rangle$) atoms. Thus we are free to control the "red" ($|1,-1\rangle$) atoms as long as the total population information is conserved, and this is a good condition to adopt a modified field-tagging method [151] that only uses a transition from two states instead of 6. By sending $|1,-1\rangle$ atoms into $|2,-1\rangle$ and $|2,-2\rangle$ states with microwave coupling immediately before the time-of-flight imaging, we can obtain the information of magnetic field at the moment (more precisely,

about 100μs delayed) of the measurement. The assumption that we should consider here is that this concise version of field-tagging is more fragile on the large magnetic field fluctuation, since the fitting basically assumes that the magnetic field moves with in the right shoulder of the Rabi spectrum for each transition (cf. Figure 1(d) of [151]). Thus once the assumption fails due to the large scale of field fluctuation, it is easy to be misguided from the field tagging.

Magnetic field following

In general, it is very easy to overlook the noise that comes from the 60Hz-110V power source for electronics. In our experiment, however, the magnetic field that is induced by this 60Hz noise is critical. We typically maintain our bias magnetic field of 5G in order to supply the quantization axis, and the fluctuation of input source 60Hz gives the fluctuation of the magnetic field up to mG order.

One good thing that we have is that the noise is given with the harmonic of 60Hz and all the electronics in the lab share the same power sources, which means that all those noises are in phase. Thus by triggering the noise so that matching the phase perfectly in 180°, the system always experience the same fluctuation which is easy to handle by sending our the compensating magnetic field from the small Helmholtz configuration coil. Again, details can be found in the PhD thesis of Ludwig Krinner [113].

4.3.2 Preparation of atomic quantum emitters

This subsection will explain how we prepare the atomic quantum emitter that is an analogue to a photonic two-level system that emits matter waves instead of the photon. The schematic diagram is given in fig. 4.3. We start with two different ground states, $|r\rangle = |1, -1\rangle$ and $|b\rangle = |2, 0\rangle$ of ^{87}Rb atoms. By coupling them with the microwave of $\sim$6.8GHz, with the coupling strength Ω and detuning Δ, we can control the relative energy level of two states in the co-rotating frame as shown in fig. 4.3. We then apply the state-selective potential that only traps the $|r\rangle$ state, so that the red atoms are confined in each site of the optical lattice along the z-axis while the blue atoms are free to move. Then in terms of the energy levels, the microwave couples the confined $|r\rangle$ states to free $|b_k\rangle$ states with momentum k and kinetic energy $\epsilon_k = \hbar^2 k^2/2m$.

In practice, starting from an optically trapped BEC of $|1, -1\rangle$, we ramp up the optical lattice in all three dimensions simultaneously for 90 ms. For x-y plane, we use far-detuned optical lattice with $\lambda = 1064$nm which confines

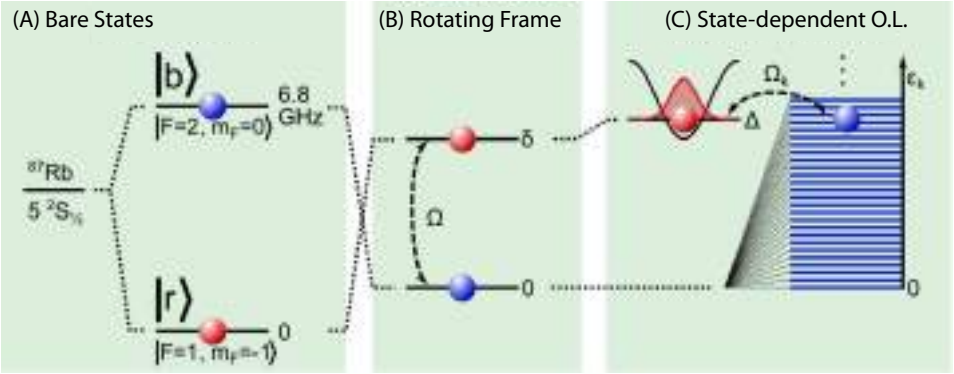

Figure 4.3: Realization of atomic quantum emitters (A) The bare hyperfine states pair (ground states $|r\rangle = |1, -1\rangle$ (red) and $|b\rangle = |2, 0\rangle$ (blue)) of ^{87}Rb is chosen. Both states are confined in tubes along z-axis. (B) With $\sim$ 5G bias magnetic field, microwave coupling $\omega_\mu \sim 6.8$ GHz, variable coupling strength Ω with detuning δ is applied. In the rotating frame, $|r\rangle$ is detuned from $|b\rangle$ by an amount δ. (C) The state-dependent optical lattice is applied along z axis, and only the red state is trapped with this lattice. The zero-point energy of $|r\rangle$ atoms $\omega_0/2$ shifts δ to $\Delta = \delta + \omega_0/2$. The microwave then couples trapped $|r\rangle$ states to free $|b\rangle$ states with a continuum of momentum states $|b_k\rangle$ and kinetic energy ε_k with free dispersion relation. Illustration adapted from Krinner, et al., Nature **559**, 589 (2018) [86].

both red and blue atoms with same potential, $s_\perp = 40E_r$ in our case, where $E_{r,\perp} = h^2/2m\lambda^2 \sim h \times 1.98$ kHz. For the z-axis, we use state-selective lattice with $\lambda = 790.0$nm that only traps red with $s_r = 30E_r$, here $E_{r,z} \sim h \times 3.66$ kHz. Then the system is in a deeply confined Mott-insulating regime.

After loading the $|1, -1\rangle$ atoms, we send most of the atoms (~ 0.82) to the $|2, 1\rangle$ state by using two-photon process with RF-pulse, and then blow the transferred atoms away by illuminating the resonance imaging light on the D_2 cycling transition. This process gives a stochastically populated lattice with an average site occupation of $< n_i > \lesssim 0.5$, which means that every next site is emptied out. Thus the experiment is effectively in a single-particle regime that for which the effects from the mean field or collective motion are not relevant.

4.4 Matter-wave decay in the continuum

This section reviews the experimental results based on our publication *Spontaneous emission of matter waves from a tunable open quantum system*, Ludwig Krinner, Michael Stewart, Arturo Pazmiño, Joonhyuk Kwon, Dominik

Schneble, Nature, **559**, 589 (2018) [86].

4.4.1 Spontaneous emission

Here, we will see how the system we describe here is an analogue to the spontaneous emission from the Weisskopf-Wigner Hamiltonian described in the previous section. We start from the interaction Hamiltonian of vacuum Rabi coupling of two states $|r\rangle$ and $|b\rangle$ under the state-selective potential as described above,

$$\hat{H}_I = \sum_{\boldsymbol{k}} \hbar g_{\boldsymbol{k}} e^{i\Delta_k t} \hat{r} \hat{b}^\dagger_{\boldsymbol{k}} + H.c. \tag{4.10}$$

where $\hbar g_{\boldsymbol{k}} = \hbar\Omega\gamma_{\boldsymbol{k}}/2$, $\Delta_k = \hbar^2 k^2/m$ with the consideration of zero-energy shift of $\Delta = \delta + \omega/2$, and $\gamma_{\boldsymbol{k}} = \langle k|\psi_e\rangle$ is the Frank-Condon overlap factor. Here we can describe the annihilation operator $\hat{r}$ as $\hat{r} = |g\rangle\langle e|$ since the trapped red atom turns into the free-propagating blue atom. Then we have

$$\hat{H}_I = \sum_{\boldsymbol{k}} \frac{\hbar\Omega}{2} \gamma_{\boldsymbol{k}} e^{i\Delta_k t} \hat{b}^\dagger_{\boldsymbol{k}} |g\rangle\langle e| + H.c. \tag{4.11}$$

which represents the Weisskopf-Wigner Hamiltonian of spontaneous emission.

The experimental results in fig. 4.4 (A) confirm that our atomic quantum emitter system reproduces the spontaneous emission as expected; the normalized population of the red atom decays exponentially in time-domain as it supposed. There is an offset, however, that the population decays not all the way down to 0 but to 0.5, which we think is the effect of the neighboring empty sites. The emitted blue atom can always be re-absorbed, which gives the average 0.5 red atoms in the end. This was tested by comparing the theoretical models for 1-site and 3-site emitter cases as shown in an inset of fig. 4.4 (A) . With the presence of empty neighbor sites that act as ground state emitters, the simulation gives both the offset and the small oscillations which is the sign of re-absorption.

The time scale of the decay, τ, is given by the Markovian dynamics as $\sim 1/\Gamma = 2$ms, where $\Gamma = \Omega^2_{\bar{k}}/\sqrt{\omega_0\Delta}$. Here, $\Omega_{\bar{k}} = \Omega\gamma_{\bar{k}}$ and $\bar{k} = \sqrt{2m\Delta/\hbar}$.

We can also see how the emitted blue atoms behave. As for a two-level photonic system, the emitted "blue" atom in our case carries away the effective energy difference between the quantum emitter states, Δ. Fig. 4.4 (B) shows that the observed momentum distribution of the emitted blue atom which agrees with the single-particle dispersion relation that is parabolic.

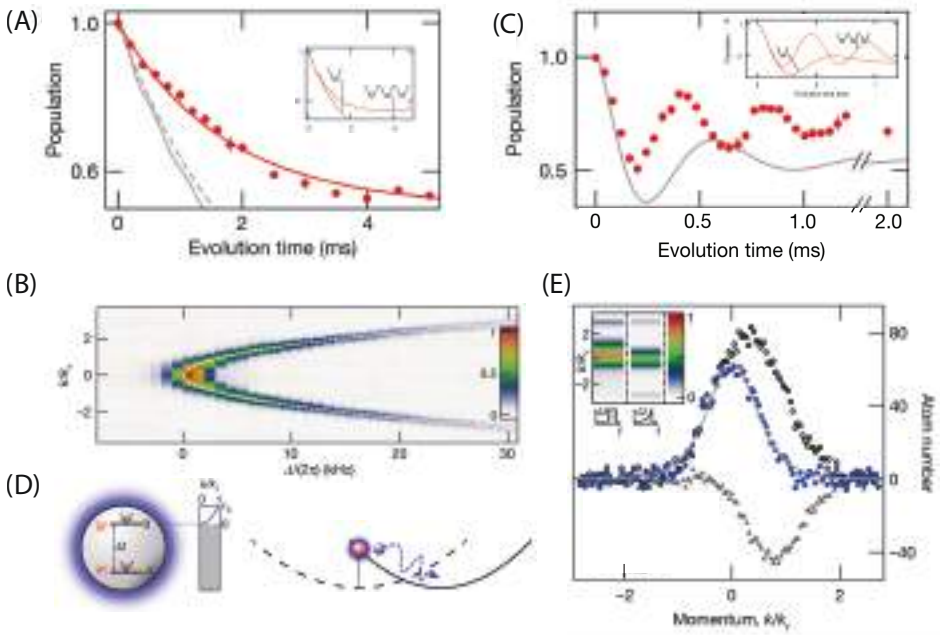

Figure 4.4: Results of Krinner et al. [86] (A) Spontaneous decay in the Markovian regime. The time evolution of the lattice population is shown in red circles. Here the coupling strength $\Omega = 2\pi \times 0.74$ kHz and detuning $\Delta = 2\pi \times 1.9$ kHz, which gives (quasi-)Markovian regime ($(\Omega/\Delta)^2 \ll 1$). The red line is our experimental fit for exponential decay and gray line is theoretical model from the Markovian approximation (dashed) and the isolated emitter model from [150] (solid). (Inset) Simulated decay dynamics for 1-site and 3-site model. (B) Momentum space profile of emitted blue atom for the same parameters as (A). The white dashed line is the single particle dispersion, based on the energy conservation from the positive detuning. (C) Non-Markovian dynamics. Same measurement with (A) for different parameters ($\Delta = -2\pi \times 1.7$ kHz, $\Omega = 2\pi \times 3.0$ kHz). The inset shows the results of a numerical simulation. (D) Bound state for negative excitation energy (left), and the separation of the bound state by using adiabatic/non-adiabatic preparation of the system using gravitational sag (right). The bound state is frozen in space, but the non-adiabatically released fraction rolls down the potential hill along the tube with accelerated non-zero momentum. (E) Momentum distribution of $|b\rangle$ atoms for adiabatic/non-adiabatic preparations. Open (filled) circles represent the sudden (adiabatic) turn-on of the coupling, and triangles show the difference of the two datasets. The solid line represents the square of the Fourier transform of the analytical evanescent wavefunction of the bound state.

4.4.2 Non-Markovian regime and the bound state

One interesting feature of our system is the tunability of the energy difference between the excited and ground states of the atomic quantum emitter.

As the detuning becomes small compared with the coupling strength, $\Delta/\Omega \ll 1$, the decay dynamics experiences the effect of the edge of the continuum. Instead of the exponential decay as traditionally seen for weak coupling (Markovian: memory-less), the dynamics become oscillatory. This non-Markovian oscillation qualitatively agreed with the theoretical prediction [150], and we were able to observe a similar oscillation with higher frequency for negative detuning as shown in fig. 4.4 (C).

Compared to the fact that it is very natural to visualize the case of positive detuning case where the emitted matter-wave carries the excess momentum, it is not straight-forward to imagine the case of negative detuning since emitting something with the negative energy is not physically allowed physically. Instead of the emission, what is observed is the bound-state, which is a natural form of the evanescent waves with a binding energy $\hbar\omega_B \approx \hbar\Delta$, where the negative detuning $\Delta = -2\pi \times 1.7$ kHz is used. Fig. 4.4 (D) shows the illustration of the bound-state formation with negative excitation energy, and this bound-state is localized with the localization length $\xi = 1/\sqrt{2m|\omega_B|/\hbar} \sim 142$nm.

4.5 Decay in a structured vacuum

This section reviews experimental results from our publication *Dynamics of matter-wave quantum emitters in a structured vacuum*, Michael Stewart, Joonhyuk Kwon, Alfonso Lanuza, Dominik Schneble, Phys. Rev. Res., **2**, 043307 (2020) [87]. The author of this dissertation contributed equally to taking experimental data for this publication alongside Michael Stewart, who in addition elaborated on important theoretical aspects in his thesis [115]. A more general theoretical analysis can also be found in a very recent theory paper of our group (A. Lanuza et al., [152])

4.5.1 Realization of single-band structure

In the previous section, we studied the atomic quantum emitter system that is analogous to an atom coupled to a photonic band-gap material. The difference is, however, that there is only one band-edge in our case (the continuum edge at zero energy), which is not the same as a real 'band'. To make a more realistic case, we extended the previous research toward the single band case.

The experimental realization is a straightfoward modification from the previous experiment; instead of a state-selective potential, we here apply a

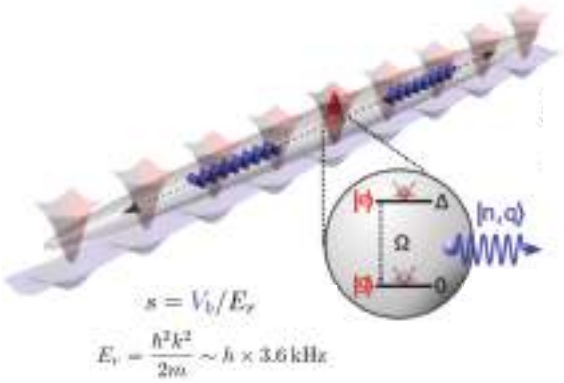

Figure 4.5: Illustration of the experimental configuration for implementing a band structure. Here both $|r\rangle$ (red) and $|b\rangle$ (blue) states are confined along the 1D tube, but with different lattice depths from the state-dependent optical lattice. Red atoms are tightly confined with $s_r = 20$, while blue atoms see a very shallow lattice $s_b \approx 2.5$, and the coupling between two states brings the system into two-level atomic quantum emitter as sec.4.4 with coupling strength Ω and detuning Δ. Illustration adapted from Stewart, et al., Phys. Rev. Res. **2**, 043307 (2020) [87].

merely state-dependent potential by choosing a slightly different wavelength (790.4nm), based on Sec. 2.5. This gives a shallow "blue" lattice $s_b = 2.5E_r$ (where red is still tightly confined with $s_r = 20E_r$, and the ground band has the width of $W_1 = 0.5E_r \approx h \times 1.8$ kHz. Fig. 4.5 shows a schematic illustration of the configuration.

Here with the shallow band structure $\varepsilon_{n,q}$, the dynamics is governed by the Weisskopf-Wigner Hamiltonian now involving Bloch waves instead of plane waves

$$\hat{H} = \sum_{n,q} \hbar g_{n,q} e^{i\Delta_{n,q}t} |\mathrm{g}\rangle \langle \mathrm{e}| \hat{b}^\dagger_{n,q} + \mathrm{H.c.} \tag{4.12}$$

where n is a band index, q is a quasi-momentum, $\Delta_{n,q} = \Delta - \varepsilon_{n,q}/\hbar$ is the effective detuning of the emitter (excitation energy $\hbar\Delta$) from the Bloch state $|n,q\rangle = \hat{b}^\dagger_{n,q}|0\rangle$, the effective vacuum coupling $g_{n,q} = \gamma_{n,q}\Omega/2$ contains the Franck-Condon overlap $\gamma_{n,q} = \langle n,q|\psi_\mathrm{e}\rangle$.

Depending on the phase between the red and the blue lattice, the coupling to the band structure that we can spectroscopically access is different due to the Frank-Condon overlap factor between the wavefunction in the deep lattice and the momentum modes in question. As shown in fig. 4.6 (A, B),

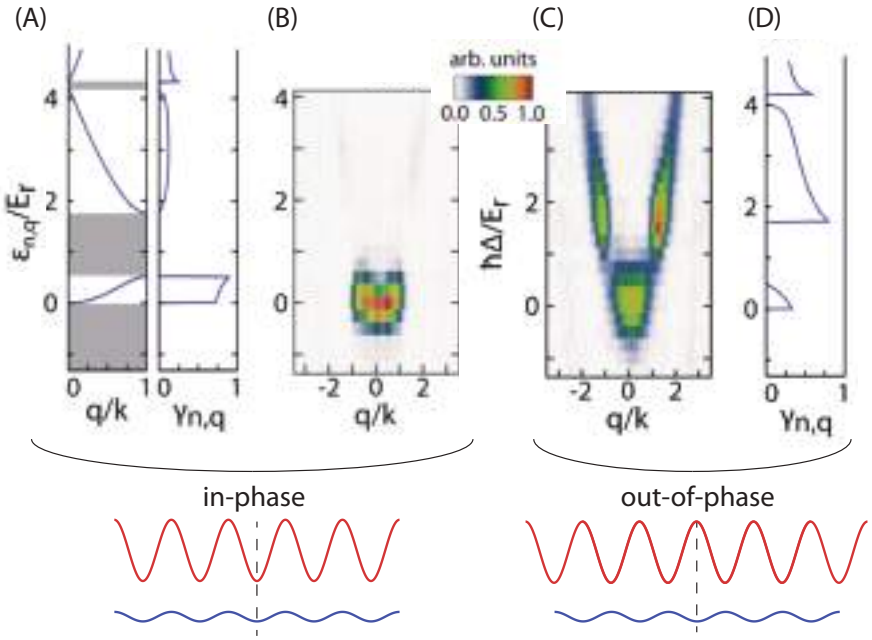

Figure 4.6: Realization of band structure for emission of matter waves. (A) Band structure $\varepsilon_{n,q}$ and corresponding Frank-Condon overlap $\gamma_{n,q} = \langle n, q|\psi_e\rangle$ for the case that the periodicity of the red lattice and blue lattice are in-phase. The higher band is suppressed from the Frank-Condon overlap factor due to the parity. (B) Momentum spectrum of the emitted matter wave. (C) Same measurement as (B) but for the case of an out-of-phase lattice, as depicted in bottom. Here we set the wavelength $\lambda = 789.8$nm to put the blue lattice as displaced (see sec. 2.5). Strong emission is measured in the first excited band. (D) Corresponding Frank-Condon overlap γ for (C). Illustration reproduced from Stewart, et al., Phys. Rev. Res. **2**, 043307 (2020) [87].

for $s_b = 2.5E_r$ (in phase), the emission into the ground band is much stronger than that into the excited bands, as the Frank-Condon factor $\gamma_{n,q}$ for those bands is strongly suppressed. The suppression of the first excited band (or higher even n-th band) is due to the odd parity of the relevant Bloch states, and the suppression of the next excited band is caused by the low density of states and finite momentum width of the excited wave function.

By shifting the sign of the state-dependent lattice potential, we can set the two lattices out of the phase which gives the negative effective lattice to blue. Fig. 4.6 (C) shows the momentum distribution and the corresponding Frank-Condon overlap for $s_b = -2.6E_r$ (out of phase), where the emission into the excited band is significant compared with the other case. This also agrees

with the calculated $\gamma_{n,q}$ as in fig. 4.6 (D).

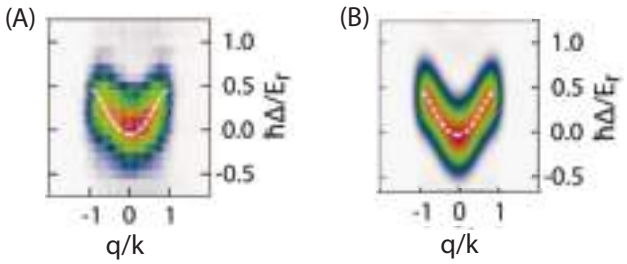

Figure 4.7: Single band emission spectrum. (A) The same measurement of fig. 4.6 (B) but with a smaller step size for better energy resolution ($0.1E_r$): the dashed line in the zoom in is theoretically calculated band structure. (B) Theoretical prediction of the momentum distribution with the consideration of experimental Gaussian blurs with $\sigma_E = 0.1E_r$ and $\sigma_q = 0.15k$ for energy and quasi-momentum, respectively. The results are compatible with the measurement in (A). Illustrations are reproduced from Stewart, et al., Phys. Rev. Res. **2**, 043307 (2020) [87].

In our experiment, by limiting the state-dependent lattice as positive for $|b\rangle$ atoms, we were able to safely focus the system into the single-band case without the concern of a contamination from the higher band. The width of our ground band is $\sim 0.5E_r \approx h \times 1.8$ kHz. Fig. 4.7 (A) shows the emission spectrum focused on the single band with finer resolution ($0.1E_r$). From the theoretical calculation of $|B_q(\tau)|^2$, we calculated the quasimomentum distribution for the comparison as shown in fig. 4.7 (B). Here we blurred the Gaussian for the better comparison with the real measurement, by $\sigma_E = 0.1E_r$ in energy and $\sigma_q = 0.15k$ in quasimomentum.

4.5.2 Transition from Markovian to non-Markovian dynamics

Since a single-band scenario is accessible now, we can play with the competing parameters, the coupling strength Ω and the bandwidth $2\bar{\omega}$ for the sinusoidal band $\varepsilon(q) = -\hbar\bar{\omega}\cos(q\pi/k) + \hbar\bar{\omega}$. We measured the time dynamics of the population as in the previous experiment but by tuning the excitation energy to the center of the band and changing the vacuum coupling versus bandwidth ratio $g/\bar{\omega}$. The decay here is incomplete due to the presence of the bound state.

Fig. 4.8 (A) shows that the decay dynamics display a transition from the Markovian to non-Markovian limit. In the case of weak coupling $g/\bar{\omega} \ll 1$ as

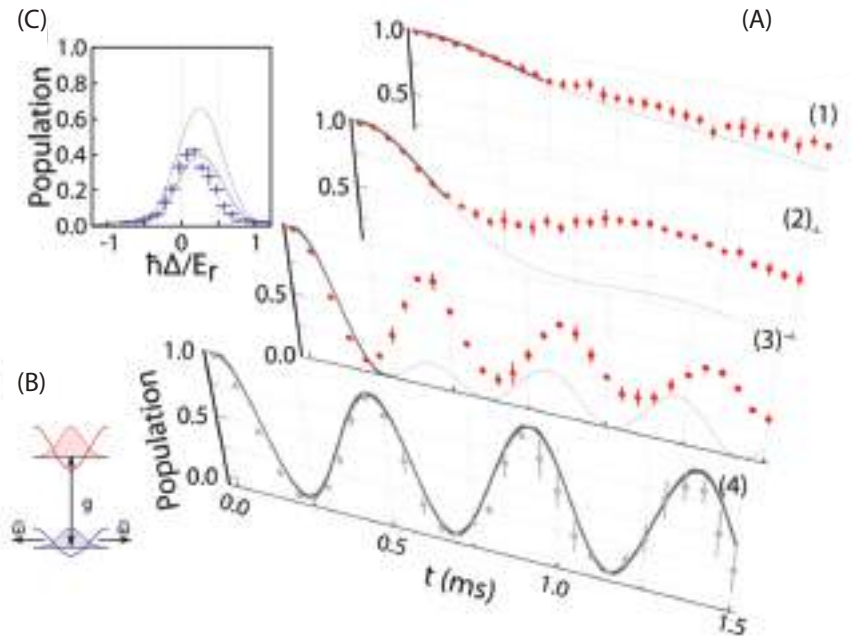

Figure 4.8: (A) Transition from Markovian to non-Markovian time dynamics at the band center $\Delta = \bar{\omega}$ for various couplings. (1) weak coupling case $\Omega = 2\pi \times 0.4$ kHz ($g/\bar{\omega} = 0.18$) (2) intermediate-weak coupling case $\Omega = 2\pi \times 1.0$ kHz ($g/\bar{\omega} = 0.43$) (3) intermediate-weak coupling case $\Omega = 2\pi \times 2.3$ kHz ($g/\bar{\omega} = 1.0$) (4) strong coupling case $\Omega = 2\pi \times 2.2$ kHz ($g/\bar{\omega} = 4.9$). The error bar represents the standard error of the mean. The gray curves are theoretical prediction from isolated-emitter model, and the bold line is the regime where the model is valid. (B) Illustration of the relation between g and $\bar{\omega}$. Here $\bar{\omega}$ is in the order of the tunneling between the blue lattice sites. (C) Ground-band emission spectrum for intermediate coupling case (A(2)) for $\tau = 400\mu$s, obtained from fig. 4.7 (A) by summing over quasi-momenta. The dashed line is the isolated-emitter model, and the solid line is the same model but reduced by 40%. Illustration is taken from Stewart, et al., Phys. Rev. Res. **2**, 043307 (2020) [87].

shown in Fig. 4.8 (A) (1), the data approximates Markovian decay which is irreversible. As the coupling gets stronger $g/\bar{\omega} \sim 1$, we observed a damped oscillation (see (A) (2, 3)), and the strong coupling $g/\bar{\omega} \gg 1$ gives undamped oscillation (A) (4). The two extreme cases (weak and strong coupling) represents the spontaneous decay and vacuum Rabi oscillation in cavity-QED limit, and the intermediate coupling is the crossover between those cases.

We also can predict the time dynamics of the excitation amplitude theo-

retically by

$$A(t) = \frac{i}{2\pi}\int_{-\infty}^{\infty} d\omega G(\omega + i0^{+})e^{i(\Delta-\omega)t} \tag{4.13}$$

where $G(\omega) = 1/[\omega - \Delta - \Sigma(\omega)/\hbar]$ is the Green's function and $\Sigma(\omega) = -i\hbar g^2/\sqrt{\omega(2\bar{\omega}-\omega)}$ is the self-energy. We can note here that the singularity lies on $\omega = 0$ and $\omega = 2\bar{\omega}$ where are the edges of the single band as measured. More details can be found in the publication [87] and M. Stewart's thesis [115].

There is a qualitative agreement between the experiment and the single-emitter model (eq.4.13), which is drawn as gray line in figure. However, there is still a deviation and it gets bigger as the system goes more to the non-Markovian side. This is due to the re-absorption from the neighboring empty sites. This deviation can be reduced by considering a multi-emitter model. This was confirmed recently by our group's new preprint [152] (work spearheaded by A. Lanuza) which considers array and bandstructure effects and successfully recovers most of the observed behavior.

4.5.3 Bound-state in a band-gap

Achieving a single-band structure provides a natural benefit; a new band edge above the band, which didn't exist in previous experiment. This is indeed natural to discuss how is bound-state formed in each band gap and how they affect the system dynamics.

With the same steps as in [150], we found a bound state of the form

$$\left|\psi_B^{\pm}\right\rangle = N\left[|\mathrm{e};0\rangle + \frac{g}{2k}\int_{-k}^{k} dq \frac{|\mathrm{g};1,q\rangle}{\omega_B^{\pm} - \omega(q)}\right] \tag{4.14}$$

where N is a normalization constant, $\omega_B^{\pm}$ is the bound state energy, $\omega(q) = \varepsilon(q)/\hbar$. Here, $|\mathrm{e};0\rangle$ is a lattice site occupied by a red atom (zero momentum), and $|\mathrm{g};1,q\rangle$ is an emitted blue atom (and empty lattice site) with momenta q.

Note here that we now can apply the above-band bound state case. For the upper bound state, $\omega_B^{\pm} - \omega(q)$ goes to zero near $q = \pm k$ so that the amplitude of the quasi-momentum probability diverges at two finite quasi-momenta that are not zero. Fig. 4.9 shows the experimental results which confirms the theoretical prediction. Here, we adiabatically ramp up the microwave coupling in order to minimize the contamination of the momentum space from the gravitational sag effect.

For the bound state below the band, the case is exactly similar with one-edge case in previous section; the momentum distribution of the bound state

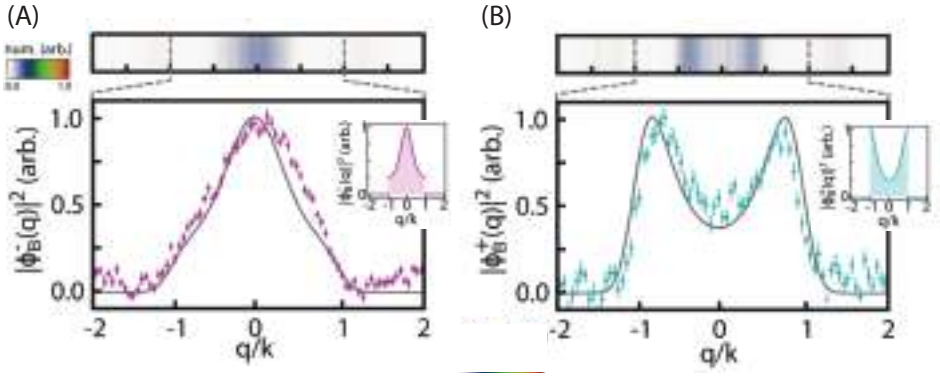

Figure 4.9: Bound states in bandgap. (A) Momentum distribution of the bound state below the band edge, $\hbar\Delta^- = -0.5E_r$. The bound state is prepared by adiabatically ramped up microwave coupling over 2ms with the maximum coupling $g/\bar{\omega} = 0.43$ ($\Omega = 2\pi \times 1.0$kHz). The colored bar is the density plot that is averaged from the time-of-flight image. The gray curve is the Gaussian blurred quasi-momentum distribution of the inset in a same way of fig. 4.7 (B). (Inset) Calculated quasi-momentum distribution below the band at $\hbar\omega_B^- = -2\hbar\bar{\omega} \approx h \times -1.9$kHz. (B) The same measurement but above the band edge, $\hbar\Delta^+ = 1.0E_r$. The bound state has two peaks unlike the below the edge case (A). (Inset) Same calculation as an inset of (A), but with $\hbar\omega_B^+ = 4\hbar\bar{\omega} \approx h \times 3.9$kHz. Illustration is reproduced from Stewart, et al., Phys. Rev. Res. **2**, 043307 (2020) [87].

is centered at zero quasi-momentum and single-peaked. For the bound state above the band, we observed a double-peaked momentum distribution, which was not previously discussed in the literature. We simulated the momentum distribution of the bound state in each side with our isolated-emitter model [87, 115] which is shown as inset for both fig. 4.9 (A) and (B). We applied the finite volume effect and imaging resolution to convolve the toy model into a realistic prediction, and that is the grey curve in the main plots in fig. 4.9, which shows qualitative agreements between the theory and the measurement.

In our paper [87], we also discussed the relationship between the bound states and the observed dynamics. For very strong coupling $g/\bar{\omega} \gg 1$ with Rabi dynamics, each atom oscillates between the "red" and the "blue" lattice, such that the oscillation can be interpreted as resulting from their dressed states, where the spatial wavefunctions are the Wannier state of the corresponding lattice potential. For weaker couplings $g/\bar{\omega} \approx 1$, the blue Wannier functions (which have an equal contribution of all Bloch states) are replaced by the evanescent waves of the bound states.

Chapter 5

Formation of matter-wave polaritons

This chapter reproduces our publication *Formation of Matter-Wave Polaritons in an Optical Lattice*, arXiv:2109.02243 (2021), with co-authors Y. Kim, A. Lanuza, and D. Schneble [88]. Most text and figures are quoted verbatim from the publication, and the author of this dissertation gratefully acknowledges the contribution of his co-authors. Additional figures are marked with an asterisk (*) in the figure caption. D. Schneble, the author of this dissertation, and Y. Kim designed the experiments. The author and Y. Kim took the measurements. Data analysis was performed by the author, Y. Kim and A. Lanuza. Theoretical modeling was done by A. Lanuza. The results were discussed and interpreted by all authors. Figures were created by the author and A. Lanuza. D. Schneble supervised the project. The manuscript was written by the author and D. Schneble with contributions from A. Lanuza and Y. Kim.

5.1 Introduction

The polariton, a quasiparticle formed by strong coupling of a photon to a matter excitation, is a fundamental ingredient of emergent photonic quantum systems ranging from semiconductor nanophotonics to circuit quantum electrodynamics [102, 153]. Exploiting the interaction between polaritons has led to the realization of superfluids of light [96, 101] as well as of strongly correlated phases in the microwave domain [154], with similar efforts underway for microcavity exciton-polaritons [97]. Here, we develop an ultracold-atom analogue of an exciton-polariton system in which interacting polaritonic phases can be studied with full tunability and without dissipation. In our optical-

lattice system, the exciton is replaced by an atomic excitation, while an atomic matter wave is substituted for the photon under a strong dynamical coupling. We access the band structure of the matter-wave polariton spectroscopically by coupling the upper and lower polariton branches, and explore polaritonic many-body transport in the superfluid and Mott-insulating regimes, finding quantitative agreement with our theoretical expectations. Our work opens up novel possibilities for studies of polaritonic quantum matter.

Since their first description as a superposition of light and matter excitations [91, 92], polaritons have been an essential key for understanding the nature of strong light-matter couplings in solids. While the polariton concept [93] has been broadly expanded to various fields and contexts [95], its essence is captured by the microcavity polariton, whose realization in a semiconductor [94] first revealed exciton-photon mode splitting as the signature of a mobile, dynamically-coupled quasi-particle with a dispersion relation that hybridizes those of its two constituents.

Polariton interactions, mediated by the excitation, open up novel possibilities for engineering effective photon-photon interactions that can lead to Bose-Einstein condensation [96, 101] and strongly interacting many-body states [102, 154]. In this context, several polariton platforms including semiconductor microcavities [153], Rydberg polaritons [101], as well as waveguide [108] and circuit [102] quantum electrodynamics, provide breakthrough possibilities for quantum simulations [103, 155]. Here, it is an important challenge to achieve strong coupling [145] and interactions [156] with tunable parameters while managing dissipation [154] and assuring scalability [157].

In this chapter, using a recently developed experimental approach [86, 87] with ultracold atoms in an optical lattice, we introduce a scalable polariton platform featuring full flexibility and no intrinsic losses, in which the photonic constituent is replaced by a matter wave. While replicating the fundamental features of conventional polaritons [95], the ratio of effective mass and interactions of these novel matter-wave polaritons is fully tunable, and the system is dissipation-free with an infinite Purcell factor. By controlling the parameters in the regime of interest, our system can simulate polaritonic manybody properties in the regime of strong interactions [99, 100, 158].

In analogy to an exciton-polariton, we realize a quasiparticle that hybridizes the quadratic dispersion relations of two constituents of disparate mass. While the light constituent playing the role of the photon in the microcavity is a free-space atomic matter wave, the other constituent, replacing the exciton, is an atom with high effective mass induced by an optical lattice, that is coupled to the matter wave via an effective dipole moment. The coupling hybridizes the two dispersion relations into lower (LP) and upper (UP)

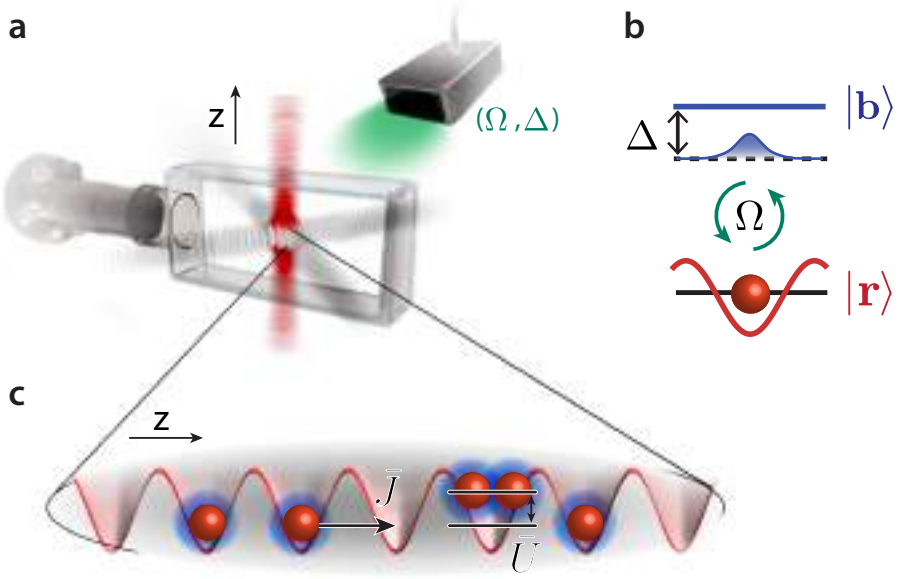

Figure 5.1: **Experimental scheme and polariton formation**. **a,b,** An $|r\rangle$ (red) atom in the ground band of a deep state-selective optical lattice (red) is coupled through a microwave field (green) with strength Ω and detuning $\Delta < 0$ to an unconfined state $|b\rangle$ (blue) with energy below the edge of the continuum of motional states. The atomic ensemble is confined to a system of tightly confining tubes created with state-independent transverse lattices (gray). **c,** In each tube, the coupling results in a polaritonic superposition of lattice-trapped atoms and matter-wave modes with quasi-particle hopping $\bar{J}$ and on-site interaction $\bar{U}$.

polariton branches. The optical lattice confining the atom not only increases its effective mass but also provides an analog of strongly-correlated polaritonic arrays [153], in which the interaction between excitons is replaced by the natural collisional interaction between the heavy atoms in the lattice. We create a system of strongly-interacting polaritons, in which the competition between hopping and interactions lead to a tunable phase transition from a polaritonic superfluid to a Mott insulator, in agreement with expectations based on the polariton band structure [152, 158].

5.2 Experimental setup

The scheme for our experiments is illustrated in Fig. 5.1. Using an optically-trapped Bose-Einstein condensate of around 10^4 ^{87}Rb atoms in the hyperfine

ground state $|r\rangle \equiv |F = 1, m_F = -1\rangle$, we load an array of 10^3 red-detuned, tightly-confining optical lattice tubes with depth $s_\perp \gg 1$ measured in terms of the recoil energy $E_{r\perp} = h^2/2m\lambda_\perp^2$, where $\lambda_\perp = 1064$ nm is the lattice laser wavelength and m the atomic mass. Another lattice ("z-lattice") with variable depth s, in terms of a corresponding recoil energy $E_r = \hbar\omega_r$ at wavelength λ, additionally confines the $|r\rangle$ atoms along the vertical z axis aligned with the tubes. The $|r\rangle$ atoms hop between sites of the z lattice with finite tunnel coefficient J, while transport across tubes is negligible on experimentally relevant time scales. The atoms are coupled to a second hyperfine ground state, $|b\rangle \equiv |F = 2, m_F = 0\rangle$ via a 6.8 GHz microwave field of strength Ω and negative detuning Δ from the atomic resonance in the z-lattice, which is shifted by the difference in zero-point energy. The wavelength $\lambda = 790.0$ nm and polarization (σ^-) of the z-lattice (for which $E_r = h \times 3.67$ kHz) are chosen such that it is fully state-selective and $|b\rangle$ atoms do not experience its potential at all, and can freely move along the tubes (for times smaller than $2\pi/\omega_z \sim 10$ ms) occupying a continuum of modes $|p\rangle$ with momentum p.

As observed in [86], for the radiative decay of an atom from a lattice well, the coupling to the free modes for $\Delta < 0$ induces the formation of a bound state containing an evanescent $|b\rangle$ matter wave with decay length $\sim \sqrt{\hbar/2m|\Delta|}$. If now the evanescent wave starts to leak into neighboring sites, the coupling between the two components can induce an effective tunneling of the $|r\rangle$ atom, and since the evanescent wave remains localized around the atom, this process then corresponds the hopping of a quasiparticle. In a many-body system, such matter-wave polaritons will be characterized by an effective tunneling matrix element $\bar{J}$ and an onsite interaction $\bar{U}$. Here we explore the signatures of polariton formation in a Bose-Hubbard scenario in which the overall state of the system is tuned via the ratio between tunneling and onsite interactions.

5.3 Measurement of the onsite-interaction energy

To explore the effects of the vacuum coupling, we first measure the excitation spectrum deep in the Mott regime with a small ratio $J/U \sim 5 \times 10^{-3}$ between atomic tunneling and onsite interactions. The procedure is summarized in Fig. 5.2**a** and **b**. After preparing the system at $s_z = 14$ and $s_\perp = 40$ (where $U = h \times 1.7$ kHz), we exponentially ramp up Ω at fixed Δ on a time scale $\tau \gg 1/|\Delta|$ that is long enough to preclude nonadiabatic shedding of matter waves [86]. With the coupling Ω applied, we sinusoidally modulate $s_\perp$ at variable frequency $\bar{\omega}$ in order to induce resonant excitations of the gapped

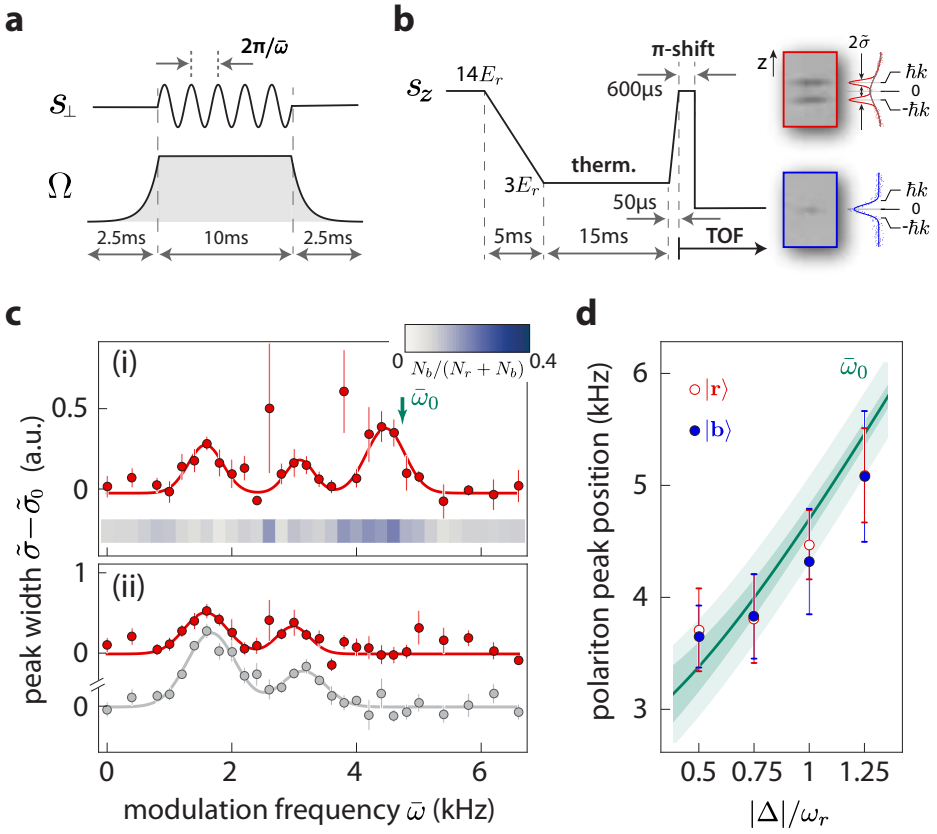

Figure 5.2: **Excitation spectra in the Mott regime** ($s_\perp = 40$, $s_z = 14$). **a,** Excitation: after ramping up Ω, $s_\perp$ is modulated by $\pm 30\%$ at variable frequency $\bar{\omega}$ for 10 ms. **b,** Detection sequence involving rethermalization and a gravitational π-phase shift for the $|r\rangle$ atoms after the coupling is turned off (details see sec. 5.7). The two panels display the $|r\rangle$ and $|b\rangle$ momentum distributions measured after resonant excitation at detuning $\Delta/\omega_r = -1.00(7)$ and coupling $\Omega/\omega_r = 1.09(2)$. The width $\tilde{\sigma}$ is extracted through Gaussian fits to the 1D density along z. **c,** Excitation spectra (i) for Δ, Ω as in **b**, with the inset stripe showing the number of $|b\rangle$ atoms; (ii) for the uncoupled case $\Omega = 0$ (red) and additionally s_z=10 (gray). **d,** Detuning dependence of the third excitation feature. Open red circles denote the $|r\rangle$ peak position, and blue dots denote the position of the maximum transfer of $|b\rangle$ atoms, as extracted from Gaussian fits, with error bars giving the spectral width of the excitation. The green curve is the calculated polariton excitation energy $\bar{\omega}(\Delta, \Omega)$, where the shaded areas include the width of the ground band (darker green) and the uncertainties in Δ (± 0.27 kHz) and Ω ($\pm 2\%$) (lighter green).

Mott phase [159] (we note that, while varying $s_\perp$ changes the polariton onsite interaction $\bar{U}$, it does not directly affect the single-polariton feature Δ). After ramping Ω back down, we enter the superfluid regime in which we characterize the effects of the modulation, which are in the form of a reduction of coherence, via time-of-flight (ToF) measurements.

The effects of the coupling on the excitation spectrum are shown in Fig. 5.2**c**. In a reference run without coupling, we observe excitation peaks near $\bar{\omega} = U/\hbar$ and $2U/\hbar$, as expected from resonant atom redistribution between sites [160]. The coupling has no noticeable effect on the position of the peaks, suggesting that for the parameters used ($\Omega, |\Delta| \sim \omega_r$) the change of the on-site energy is small. However, an additional feature appears, centered at a larger modulation frequency $\bar{\omega}$ not far from $|\Delta|$ (see Fig. 5.2**d**), accompanied by excess $|b\rangle$ population left after the coupling is ramped back down.

5.4 Theoretical approach

In order to discuss these observations further, we first develop a quantitative description of the expected polariton features, following the general approach of [158]. We first consider a $|r\rangle$ atom coherently distributed over the sites of the z-lattice, such that the system Hamiltonian takes the form of a series of coupled Weisskopf-Wigner models. By expressing the momentum of the vacuum modes $p_{n,q}$ in terms of a quasimomentum $q \in [-k, k]$ and an integer band index $n \geq 1$, the non-interacting part of the Hamiltonian decouples as

$$\hat{H} = \sum_{n,q} \varepsilon_{n,q} \hat{c}^\dagger_{n,q} \hat{c}_{n,q}, \tag{5.1}$$

where

$$\hat{c}^\dagger_{n,q} = \alpha_{n,q} \hat{r}^\dagger_q + \sum_{n\prime} \beta_{n,n\prime,q} \hat{b}^\dagger_{n\prime,q} \tag{5.2}$$

creates a matter-wave polariton as a (Ω, Δ)-dependent superposition of a $|r\rangle$ Bloch wave and all $|b\rangle$ modes of the same q. The corresponding polariton dispersion relation $\varepsilon_{n,q}$ emerges from the equation

$$\varepsilon_{n,q} - \hbar\Delta_q = \sum_{n'} \hbar^2 g^2_{n',q} / \left(\varepsilon_{n,q} - E_{n',q}\right) \tag{5.3}$$

(see sec. 5.7 and [152]), where $g_{n,q} = \Omega \langle \phi_0 | n, q \rangle / 2$ is the coupling strength between the originating lattice Wannier function $|\phi_0\rangle$ and the free-momentum mode $|n, q\rangle$ normalized to a Wigner-Seitz cell, $E_{n,q} = p^2_{n,q}/2m$ is the free-atom dispersion, and $\Delta_q = \Delta + 4J \sin^2(\pi q/2k)$ a q-dependent detuning from

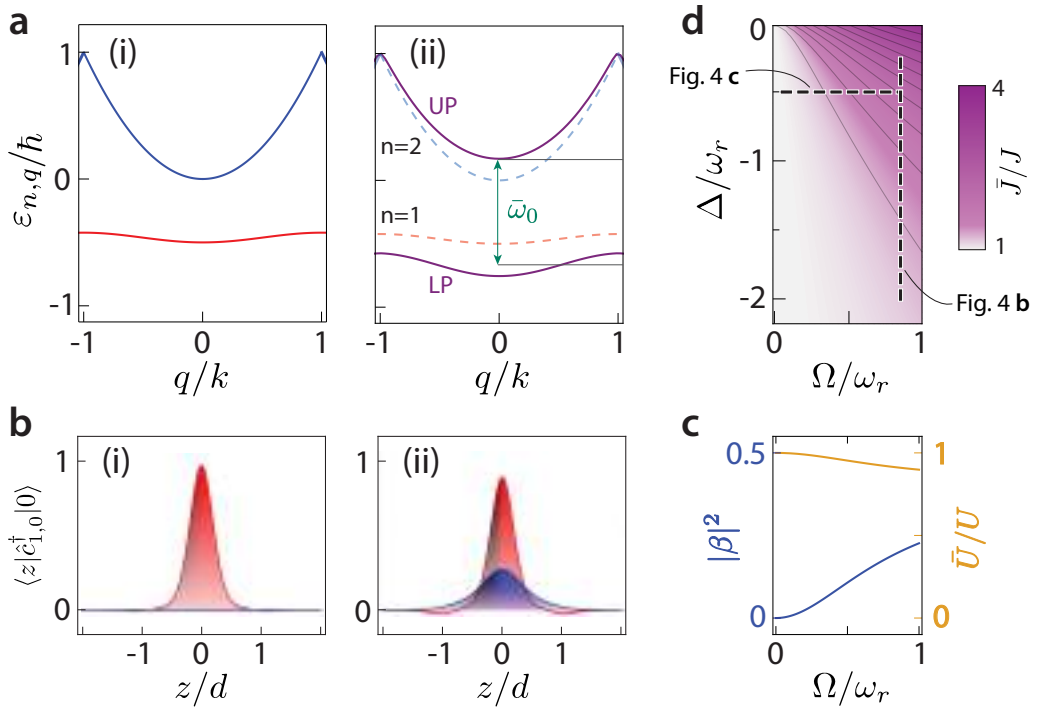

Figure 5.3: **Polariton band structure**, calculated for $s_z = 10$. **a,** (i) Uncoupled band structure for lattice-trapped atoms in $|r\rangle$ (red curve) and free atoms $|b\rangle$ (blue curve). (ii) Band structure for a coupling $\Omega/\omega_r = 1$ and a detuning $\Delta/\omega_r = -0.5$, with the two lowest polariton bands ($n = 1, 2$) shown as purple curves. The green arrow denotes the separation $\bar{\omega}_0$ from the middle of the lower band to the bottom of the upper band. The dashed curves reproduce the atomic band structure. **b,** Wannier functions obtained for the two scenarios of **a**, containing $|r\rangle$ (red) and $|b\rangle$ (blue) components, where $d = \lambda/2$. **c,** Fraction of the $|b\rangle$ component $|\beta|^2$ and polariton interaction energy $\bar{U}$ as a function of Ω for $\Delta/\omega_r = -0.5$. **d,** Polariton ground-band tunneling coefficient $\bar{J}$ relative to J as a function of Ω and Δ. The dashed lines correspond to measurements shown in Fig. 5.4**b** and **c**.

the continuum edge that accounts for the bandwidth $4J$ of the z-lattice (for details see appendix). The $n = 1$ band is the LP branch of the matter-wave polariton, while the bands with $n \geq 2$ produce a series of UP branches.

Fig. 5.3**a** depicts the ground (lower) and first excited (upper) polariton bands, $\varepsilon_{0,q}$ and $\varepsilon_{1,q}$ at a typical detuning. In real space, taking an atom localized in site j, the coupling induces, via $\hat{c}^\dagger_{n,j} = \sum_q \hat{c}^\dagger_{n,q} e^{-iqz_j}$, the formation of a matter-wave polariton as a localized quasi-particle. Its ground-band Wannier

function $\langle z|\hat{c}^{\dagger}_{1,j=0}|0\rangle$ is shown in Fig. 5.3**b**. As a result of the coupling, the $|r\rangle$ component acquires additional amplitude in neighboring sites, which can be seen as being due to a re-coupling of the evanescent $|b\rangle$ tail into the lattice potential.

We estimate the effect of the coupling on the on-site interaction in the z-lattice by setting $\bar{U} \approx \bar{g} \int \| \langle z|\hat{c}^{\dagger}_{1,j}|0\rangle \|^4 dz$, where we take the one-dimensional collisional strength $\bar{g}$ as state-independent (for ^{87}Rb, the differences are on the percent level) , such that we capture the dominant effects of the modified spatial overlap between the components. The magnitude of the shift $\delta U = (U - \bar{U})$ depends on both the extent of the evanescent tail and its amplitude; results for our parameters are shown in Fig. 5.3**c**. Consistent with our observation, the maximum shift $\delta U/U \sim 0.1$ is below what our spectroscopy method can systematically resolve, as is also evidenced in a reference measurement without coupling in which we correspondingly lowered U by reducing the z-lattice depth (see Fig. 5.2**c**).

Based on the polariton band structure, we now discuss the mechanism responsible for the resonant excitation of $|r\rangle$ atoms in the lattice that is accompanied by the appearance of $|b\rangle$ atoms. Polaritons in the lower band are mostly in the $|r\rangle$ state, which is tightly confined. As they are periodically squeezed in the orthogonal direction, they are subject to a strong perturbation of their interaction energy $\bar{U}$. If this is done resonantly ($\bar{\omega} \approx \bar{\omega}_0$), they can be excited into the upper band, as it is mostly composed of the unconfined $|b\rangle$ state and thus is less sensitive to such perturbations. The third peak in the excitation spectrum (see Fig. 5.2**c**) located around the frequency difference $\bar{\omega}_0$ between the bottom of the UP band and the center of the LP band, $\hbar\bar{\omega}_0 = \varepsilon_{2,0} - \sum_q \varepsilon_{1,q}$ corresponds to a conversion from the deeply-bound Wannier polariton state to quasi-free states in the region where the density of states is highest. The band gap increases with $|\Delta|$, requiring higher modulation frequencies $\bar{\omega}$ to excite this resonance (c.f. Fig. 5.2**d**). Because the UP is dominated by $|b\rangle$, the excitation from the LP leaves $|r\rangle$ vacancies in the z-lattice, and atoms are instead observed as excess $|b\rangle$ population around zero momentum, as seen in the inset in Fig. 5.2**b**.

5.5 Measurement of transport behavior

To further elucidate these features, we study the hopping in a polariton Bose-Hubbard model. Compared to the modification of the onsite interaction $\bar{U}$, the renormalization of J for the atoms to $\bar{J} = -\sum_q \varepsilon_{1,q} e^{i\pi q/k}$ for the polaritons can be significant. In order to test the magnitude of this effect, we compare the degree of coherence of the $|r\rangle$ component at different lattice depths s_z with that

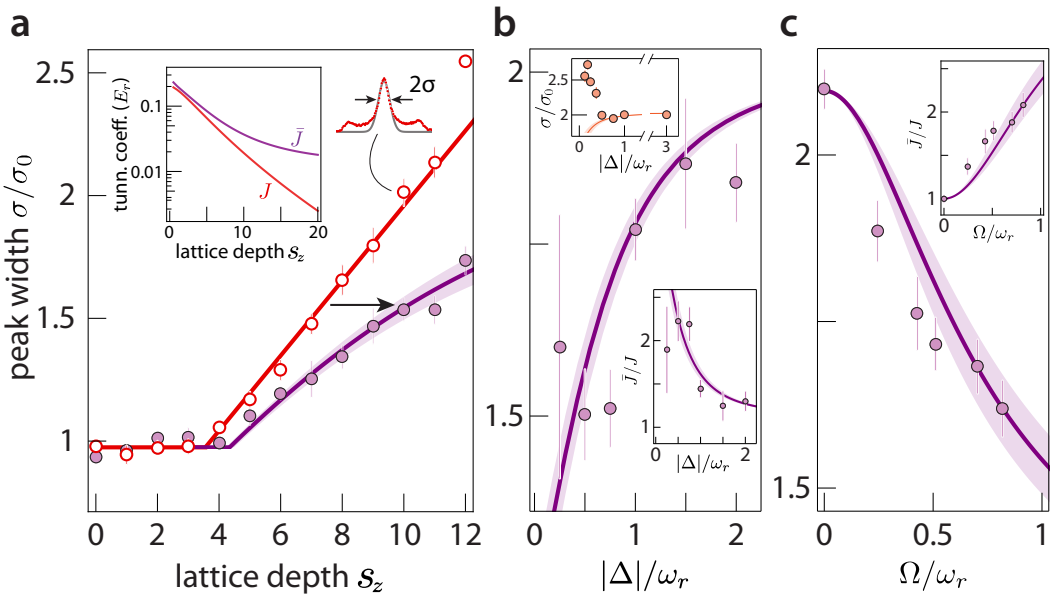

Figure 5.4: **Renormalization of hopping** extracted from the coherence of the $|r\rangle$ component at $s_\perp = 18$. **a,** Scan over s_z for $\Delta/\omega_r = -0.50(7)$, $\Omega/\omega_r = 0.84(2)$ (purple), compared to a reference measurement with $\Omega = 0$ (red). Plotted is the fitted 1D Gaussian width σ along z of the central diffraction peak in time-of-flight (see inset). The red curve is a piece-wise linear fit to the reference, with slope set to zero left of the kink, which is used to establish the relationship between σ and s_z. The purple curve is obtained from the red curve after shifting $s_z(J)$ (black arrow) according to the expected rescaling of J to $\bar{J}$; the shaded area accounts for the experimental uncertainties in Δ and Ω. Inset: tunneling coefficients J (red) and $\bar{J}$ (purple) as a function of s_z. **b, c,** Parameter scans at $s_z = 10$ according to the traces shown in Fig. 5.3**d**, with variable Δ at $\Omega/\omega_r = 0.84(2)$ (**b**), and with variable Ω at $\Delta/\omega_r = -0.50(7)$ (**c**). The theoretical prediction reflecting experimental uncertainties is shown as a solid purple line surrounded by shaded areas; the insets in the bottom half of **b** and in **c** show the corresponding ratios $\bar{J}/J$. The inset in the top half of **b** shows the peak width for $\Omega/\omega_r = 0.28(1)$ (and $\hbar\Omega/U = 1.01(1)$). Vertical error bars show the standard error of the mean; horizontal error bars are less than the size of the data points. All data points are the average over at least 3 runs.

of the (coupling-free) atomic reference with known $J \equiv J(s_z)$. Using the width of the central peak of the $|r\rangle$ diffraction pattern as a proxy [161], we record the ToF distribution after switching off the optical potential and the coupling and removing the $|b\rangle$ component with resonant light (to eliminate four-wave

mixing [82]). The results for $\Delta/\omega_r = -0.5$ and $\Omega/\omega_r = 0.8$ are shown in Fig. 5.4**a**. The peak width σ of the reference is well fit by a piecewise-linear function with fixed zero slope in the superfluid region, and positive slope in the Mott regime [66]. When we turn on the coupling, the measured peak width $\bar{\sigma}$ is comparable in the superfluid region and then increases with s_z, but not as much as the reference.

We use the fitted reference curve and the functional dependence $J(s_z)$ obtained from the uncoupled band structure to obtain an operational relationship $\sigma(J)$ between peak width and hopping. Under the assumption that the onsite interaction remains unchanged, the same relationship should hold between $\bar{\sigma}$ and $\bar{J}$ obtained from the polariton band structure, and indeed we find that the rescaled reference curve quantitatively reproduces the observed peak widths for the experimental coupling parameters. In the $|r\rangle$ basis, the polariton formation effectively renormalizes the depth of the applied lattice, leading to a horizontal shift of points of a given peak width towards increasingly larger lattice depths. Near the kink at $s_z = 4$, the rescaling of hopping implies both the presence of a superfluid-to-Mott transition of polaritons, and of a vacuum-coupling driven transition from the singly-occupied atomic Mott lobe to a polariton superfluid.

The dependence of the hopping on the coupling parameters Δ and Ω is shown in Fig. 5.4 (b, c). The measured peak width changes as expected from the rescaled reference curve, and the inferred polaritonic enhancement $\bar{J}/J$ of the hopping agrees well with the prediction of the polariton band structure. In particular, unlike J, $\bar{J}$ saturates for large s_z as a result of matter-wave-induced hopping.

In Fig. 5.4, there is good agreement between experiment and theory if at least one of the coupling parameters is comparable to ω_r. However, for weaker couplings near the continuum edge, a reduction of $|\Delta|$ can lead to an increase of the peak width, as seen in the upper inset of Fig. 5.4**b**, a behavior that cannot be explained by a violation of adiabaticity in applying the coupling ($1/\tau \sim 0.02\ \omega_r$). For small Ω and $|\Delta|$, the $|b\rangle$ component of the LP has large spatial extent and low density, such that the collisional on-site interaction between the tightly confined $|r\rangle$ atoms can lead to an effective change of the detuning. Indeed, the divergence of the peak width occurs near $|\Delta|/\omega_r \sim U/E_r = 0.28$, consistent with a shift to effectively positive detunings, at which we expect radiative matter-wave decay to give rise to a quantum Zeno effect [162]. We note that similar interaction-activated dissipation that inhibits transport in a Bose-Hubbard model has recently been observed using photon-induced losses [163].

5.6 Experimental details

5.6.1 System preparation

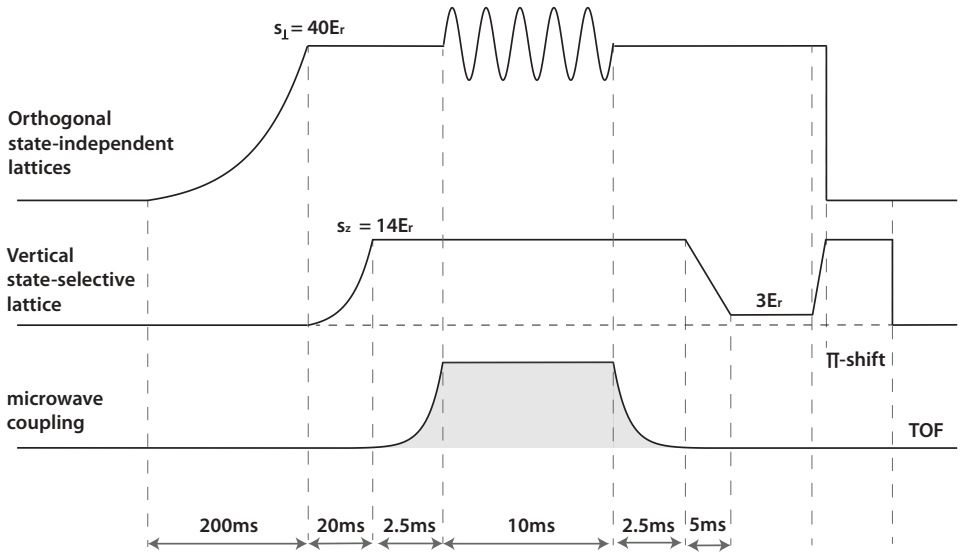

Figure 5.5: (*) Full experimental sequence for onsite-interaction energy measurement. Fig. 5.2 shows the crucial part of this whole sequence.

Our experiments start with BECs of 1×10^4 $|r\rangle$ atoms in an optical trap [86]. For the measurements of Fig. 5.2, the full experimental sequence is shown in fig. 5.5. We first ramp up the tubes over 150 ms to $s_\perp = 40$ using an exponential ramp, followed by an exponential ramp of the z lattice to $s_z = 14$ over 25 ms. Following with the reversibly-applied microwave coupling (see Fig. 5.6) and lattice modulation spectroscopy, we detect excitations through changes in the coherence back in the superfluid phase [66]. We first linearly ramp down the z-lattice to $s_z = 3$ over 5 ms followed by 15 ms of thermalization. The tubes and the optical trap are then switched off and the z-lattice depth is jumped to $s_z = 14$ (in 50 μs) and held for 600 μs to induce a gravitationally-induced π shift between the wells. The resulting diffraction pattern of $|r\rangle$ atoms features two zeroth-order peaks separated by $2\hbar k$ in the z direction. We sum over the transverse direction, fit the two peaks on top of a thermal background with three Gaussians, and extract the width $\bar{\sigma}$ as the average over the two peaks. We note that the momentum distribution of the $|b\rangle$ atoms remains unaffected by the changes in s_z, since resonant collisions during the rethermalization phase, as well as collinear four-wave mixing in time-of-flight [82], are both suppressed due to the mismatch of the $|r\rangle$ and $|b\rangle$ dispersion relations [84], and the strong

confinement in the tubes limiting coherence, respectively.

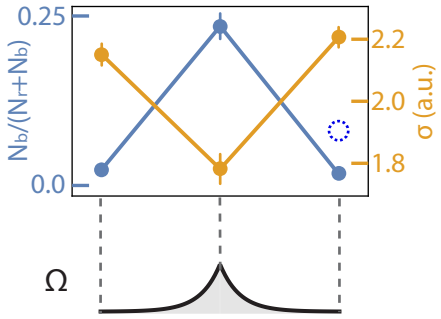

Figure 5.6: Fraction of $|b\rangle$ atoms (blue) and peak width of $|r\rangle$ atoms (orange) after a symmetric microwave ramp up and down (each over 2.5 ms) for the parameters of Fig. 5.4 at $s_z = 10$. The dotted open blue circle is the blue atom fraction for the sequence of Fig. 5.2 **c** without lattice modulation applied. We suspect that the degradation comes from magnetic-field noise that is able to drive LP→UP transitions by directly affecting Δ.

5.6.2 Atom detection

The full experimental sequence for the measurements in Fig. 5.2 is shown in Fig. 5.5, we use a smaller tube depth, $s_\perp = 18$, and ramp up the z lattice more slowly, over 80 ms (starting in the middle of the $s_\perp$ ramp) in order to maximize the system coherence over a large range of parameters. After switching off all potentials, we fit the 1D diffraction patterns using a single background-free Gaussian to extract the width σ of the central peak after summing up over the transverse direction. To eliminate possible effects of collinear four-wave mixing in ToF expansion, the $|b\rangle$ atoms are removed using a short blast pulse of resonant cycling light [82].

For atom detection, we use standard absorption imaging on the $F = 2 \rightarrow F' = 3$ cycling transition after a ToF of 15 ms, preceded by Stern-Gerlach separation of the $|r\rangle$ and $|b\rangle$ states. The $F = 1$ atoms are detected after transferring them to $F = 2$ using a short repump pulse.

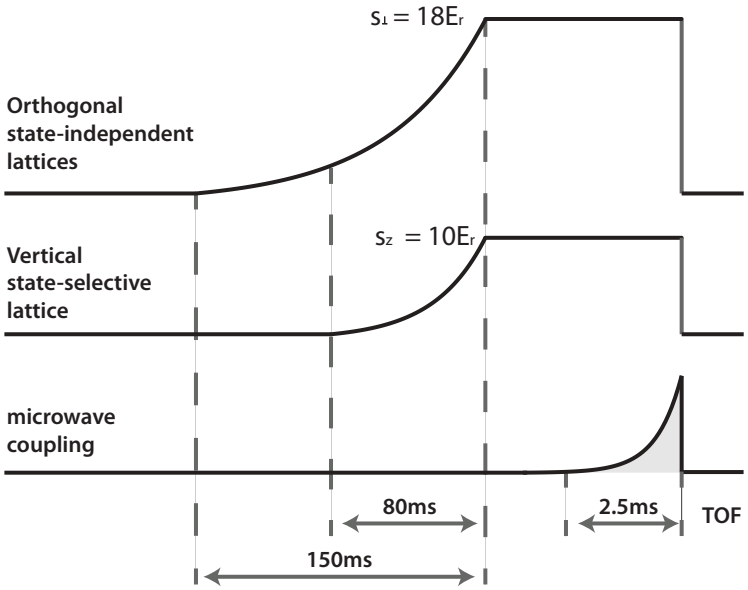

Figure 5.7: (*) Full experimental sequence for quantum transport. Measurements in fig. 5.4 are based on this experimental sequence.

5.6.3 Resonance condition

In our experiments, we need to accurately determine and maintain the resonance condition ($\Delta = 0$) between the $|r\rangle$ in the z-lattice and the $|b\rangle$ mode continuum edge. We use lattice transfer spectroscopy [85] to adjust and monitor the resonance condition interleaved with a set of measurements, with an extrapolated drift of maximally 300 Hz between shots. For this purpose, we prepare the BEC in the $|b\rangle$ state, and then apply $400\mu s$ long Rabi pulses ($\Omega = 2\pi \times 1.0$ kHz) to transfer a small fraction ($< 30\%$) of atoms into the z lattice, with calculated mean-field shifts well below 100 Hz.

5.7 Theoretical details

5.7.1 Polariton band structure

In the Schrödinger picture, our system Hamiltonian takes the form [150]

$$\begin{aligned}\hat{H}_S = &\sum_j \hbar\omega_0^{(r)} \hat{r}_j^\dagger \hat{r}_j + \sum_{n,q} \hbar\omega_{n,q}^{(b)} \hat{b}_{n,q}^\dagger \hat{b}_{n,q} \\ &+ \sum_j \sum_{n,q} \hbar g_{n,q} \left(e^{-i(\omega_\mu t + q z_j)} \hat{r}_j \hat{b}_{n,q}^\dagger + \text{H.c.} \right),\end{aligned} \tag{5.4}$$

where $\hbar\omega_{n,q}^{(b)} = \hbar\omega_0^{(b)} + E_{n,q}$ is the energy (internal plus kinetic) of the $|b\rangle$ atoms, $\hbar\omega_0^{(r)}$ is the energy of the $|r\rangle$ atoms, ω_μ is the frequency of the microwave which determines the detuning through $\Delta = \omega_\mu - (\omega_0^{(b)} - \omega_0^{(r)})$, $z_j = j\pi/k$ is the position of the j^{th} site, $\sum_j \equiv \sum_{j=-\infty}^{+\infty}$ and $\sum_{n,q} \equiv \sum_{n=1}^{\infty} \int_{-k}^{+k} \frac{\mathrm{d}q}{2k}$. The external action of the microwave makes this Hamiltonian time-dependent. However, by writing $\hat{H}_S = \hat{H}_{0,S} + \hat{H}_{1,S}$ with

$$\hat{H}_{0,S} = \sum_j \hbar(\omega_0^{(b)} - \omega_\mu)\hat{r}_j^\dagger \hat{r}_j + \sum_{n,q} \hbar\omega_0^{(b)} \hat{b}_{n,q}^\dagger \hat{b}_{n,q} \tag{5.5}$$

one gets the time-independent interaction Hamiltonian

$$\hat{H} \equiv \hat{H}_{1,I} = e^{i\hat{H}_{0,S}t/\hbar} \hat{H}_{1,S} e^{-i\hat{H}_{0,S}t/\hbar} \tag{5.6}$$

so that

$$\begin{aligned} \hat{H} = &\sum_j \hbar\Delta \hat{r}_j^\dagger \hat{r}_j + \sum_{n,q} E_{n,q} \hat{b}_{n,q}^\dagger \hat{b}_{n,q} \\ &+ \sum_j \sum_{n,q} \hbar g_{n,q} \left(e^{-iqz_j} \hat{r}_j \hat{b}_{n,q}^\dagger + \text{H.c.} \right). \end{aligned} \tag{5.7}$$

Following the approach of [158] (see [152] for an alternative), it is then possible to study the emergence of polaritons. Fourier-transforming the operators

$$\hat{r}_q = \sum_j e^{-iqz_j} \hat{r}_j, \qquad \hat{r}_j = \sum_q e^{iqz_j} \hat{r}_q \tag{5.8}$$

leads to

$$\begin{aligned} \hat{H} = &\sum_q \hbar\Delta \hat{r}_q^\dagger \hat{r}_q + \sum_{n,q} E_{n,q} \hat{b}_{n,q}^\dagger \hat{b}_{n,q} \\ &+ \sum_{n,q} \hbar g_{n,q} \left(\hat{r}_q \hat{b}_{n,q}^\dagger + \text{H.c.} \right) \equiv \sum_q \hat{H}_q \end{aligned} \tag{5.9}$$

such that the Hamiltonian decouples into independent quasimomenta $[\hat{H}_q, \hat{H}_{q'}] = 0$, where

$$\begin{aligned} \hat{H}_q = &\hbar\Delta \hat{r}_q^\dagger \hat{r}_q + \sum_n E_{n,q} \hat{b}_{n,q}^\dagger \hat{b}_{n,q} \\ &+ \sum_n \hbar g_{n,q} \left(\hat{r}_q \hat{b}_{n,q}^\dagger + \text{H.c.} \right). \end{aligned} \tag{5.10}$$

If we take $\hat{c}_{n,q}^\dagger = \alpha_{n,q} \hat{r}_q^\dagger + \sum_{n'} \beta_{n,n',q} \hat{b}_{n',q}^\dagger$ to create a quasiparticle (polariton) in the band n with quasimomentum q, then the eigenvalue condition $\hat{H}_q \hat{c}_{n,q}^\dagger |0\rangle =$

$\varepsilon_{n,q}\hat{c}^\dagger_{n,q}|0\rangle$ leads to the secular equations [158]

$$\begin{cases} (\varepsilon_{n,q} - \hbar\Delta)\alpha_{n,q} = \sum_{n'} \hbar g_{n',q}\beta_{n,n',q} \\ (\varepsilon_{n,q} - E_{n',q})\beta_{n,n',q} = \hbar g_{n',q}\alpha_{n,q} \end{cases} \tag{5.11}$$

which allow for the determination of the amplitudes $\alpha_{n,q}$ and $\beta_{n,n',q}$ (which alternatively follow from Eq. (27) in [152]) and yield the equations for the polariton dispersion relation

$$\varepsilon_{n,q} - \hbar\Delta = \sum_{n'} \frac{\hbar^2 g^2_{n',q}}{\varepsilon_{n,q} - E_{n',q}}. \tag{5.12}$$

as given in the main text.

5.7.2 Polariton Bose-Hubbard Hamiltonian

Here we show how the band structure and interactions derived above leads to a polariton Bose-Hubbard Hamiltonian. Since the non-interacting Hamiltonian in lattice-momentum space is quadratic and has energies given by (5.12), it reduces to

$$\hat{H} = \sum_{n,p} \varepsilon_{n,q}\hat{c}^\dagger_{n,p}c_{n,p}. \tag{5.13}$$

Thanks to the independence between quasimomenta, if there is some hopping J for $|r\rangle$ atoms, this can be accounted for by simply making the detuning q-dependent, $\Delta \to \Delta_q = \Delta + 4J\sin^2\left(\frac{\pi q}{2k}\right)^2$.

Reapplying (5.8) to the $\hat{c}_{n',p}$ operators, one can write the Hamiltonian in position space as

$$\hat{H} = -\sum_{n,j,j'} \bar{J}_{n,j-j'}\hat{c}^\dagger_{n,j}\hat{c}_{n,j'} \tag{5.14}$$

in terms of the hopping coefficients

$$\bar{J}_{n,j-j'} = -\sum_q \varepsilon_{n,q}e^{i\pi(j-j')q/k}. \tag{5.15}$$

For negative detunings and modest microwave couplings ($\Omega/|\Delta| < 1$) an experimental run that starts with $|r\rangle$ atoms remains dominated by $|r\rangle$, corresponding to a ground polariton band ($n = 1$) that is roughly sinusoidal, meaning that we can approximate as if there is only nearest neighbor hopping ($\bar{J}_{1,\pm1} \equiv \bar{J}$ and $\bar{J}_{1,|n|>1} \approx 0$). The constant $-\bar{J}_{1,0} = \sum_q \varepsilon_{n,q}$ is the energy of a polariton Wannier function, which is relevant for the calculation of $\bar{\omega}_0$ in Fig. 5.2. This can be combined with the local energy shift generated by

the harmonic confinement of the experiment into a site-dependent energy $\bar{\varepsilon}_j$. Omitting the band indices ($\hat{c}_{1,j} \equiv \hat{c}_j$), the above Hamiltonian then reduces to

$$\hat{H} = -\bar{J}\sum_j (\hat{c}_{j+1}^\dagger \hat{c}_j + \hat{c}_j^\dagger \hat{c}_{j+1}) + \sum_j \bar{\varepsilon}_j \hat{c}_j^\dagger \hat{c}_j, \tag{5.16}$$

which together with the polariton interaction $\hat{H}_{\text{int}}$ gives the Bose-Hubbard Hamiltonian. The interaction itself is given by

$$\hat{H}_{\text{int}} = \frac{\bar{U}}{2}\sum_j \hat{c}_j^\dagger \hat{c}_j^\dagger \hat{c}_j \hat{c}_j \tag{5.17}$$

where we calculate

$$\begin{aligned}\bar{U} \equiv & \frac{1}{2}\langle 0|\hat{c}_0 \hat{c}_0 \hat{H}_{\text{int}} \hat{c}_0^\dagger \hat{c}_0^\dagger|0\rangle \\ &= \bar{g}\left(\int \mathrm{d}z |\psi_r(z)|^4 + \int \mathrm{d}z |\psi_b(z)|^4 \right. \\ &\quad \left. + 2\int \mathrm{d}z |\psi_r(z)|^2 |\psi_b(z)|^2\right)\end{aligned} \tag{5.18}$$

in terms of the $|r\rangle$ and $|b\rangle$ components of the Wannier function, $\psi_r(z) = \langle z, r|\,\hat{c}_0^\dagger\,|0\rangle$ and $\psi_b(z) = \langle z, b|\,\hat{c}_0^\dagger\,|0\rangle$, respectively. Here $\bar{g} = 2\hbar^2 a/(m a_{0x} a_{0y})$ depends on the harmonic confinement in the tubes (a_{0x} and a_{0y}) and the (small) dependence of the scattering length $a \approx 5.3$ nm on the internal state of the atom is neglected.

5.8 Conclusion and outlook

In this work, we focused on the lower polariton branch, corresponding to renormalized hopping of excitons in a material system [153], which has allowed us to realize a polaritonic quantum phase transition as well as a transition from an atomic Mott insulator to a polariton superfluid. By exploiting the lattice band structure and applying specific couplings, exotic polariton band structures can be implemented [152], including those featuring frustration. We can also focus on the upper branch dominated by $|b\rangle$ atoms, which corresponds to the renormalized transport of photons. Making the z-lattice state-dependent (instead of state-selective [87]) will allow us to create the equivalent of coupled-cavity arrays, and implement the analogue of photon blockade [164] for $|b\rangle$ atoms, with the strongly interacting $|r\rangle$ state playing the role of a nonlinearity. Introducing couplings between more than two excitonic or photonic bands should

enable studies of analogues of multiexciton polaritons [165], multimode strong coupling [166], and spin-orbit coupling [167]. This may open up possibilities for studying topological polaritonic systems in higher dimensions [168].

Chapter 6

Toward future experiments

With our established platform, we can think about studies beyond the regime that we have dealt with so far. In this chapter, we will discuss some ideas for future experiments that should be feasible with only a small amount of modification.

6.1 Coherent dynamics in a matter-wave platform

Our matter-wave platform is very promising for studies of coherent dynamics in 1D waveguide-QED. In the following section, we will introduce some qualitative ideas that could possibly guide future experiments.

6.1.1 Collective dynamics

Arguably, one of the most interesting feature of 1D waveguide quantum electrodynamics is collective dynamics that produce super-radiant and sub-radiant phenomena. Our matter-wave platform has unique benefits since what is radiated are massive particles so that are easy to measure and control.

In general, the Dicke model [169] gives a superradiant phase in a photonic system under the collective light-matter interaction [170] when the photons share a single mode over the size of the sample. Given that the deBroglie wavelength of our system is relatively short, the Dicke model is generally not directly applicable. Instead, we can apply superradiance in the timed-Dicke model [171] that the radiation from one site is in phase with the radiation from the next site so that collective emission occurs. Then depending on the phase of the initial state (red) and the momentum of emitted matter-wave (blue), we can induce subradiant dynamics as shown in fig. 6.2.

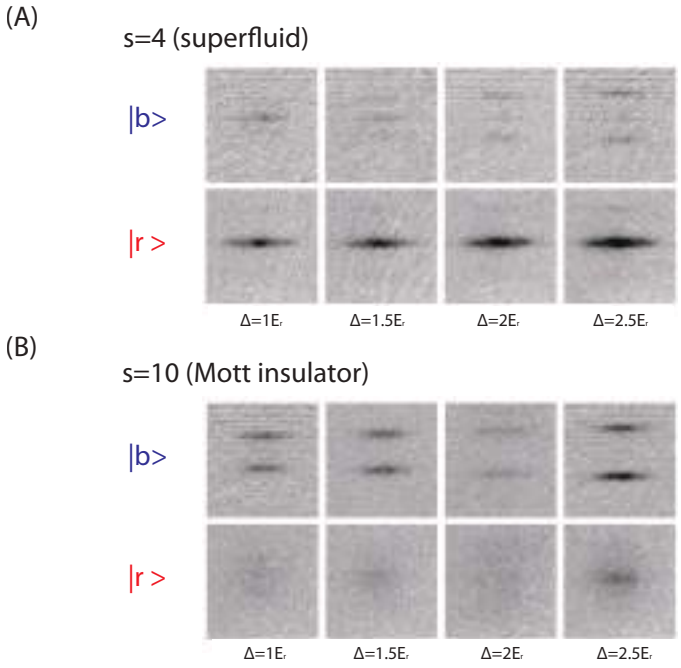

Figure 6.1: Time-of-flight image of emitted blue atoms for different initial states. The system is prepared in the same way as the matter-wave polariton experiment (see chap. 5) but the coupling here is set as positive ($\Delta > 0$), which is varied to check the momentum of emitted blue atoms. (A) For an initially coherent state (superfluid) with low red lattice depth ($s = 4$), the emission is suppressed and most of the population remains red. (B) For the incoherent state (Mott-insulator) with strong confinement ($s = 10$), the emission is more significant. For all measurements, atom number is controlled $n \sim 1.2 \times 10^4$.

In fig. 6.1, the fraction of emitted blue atoms changes whether the initial red state is coherent or not. Here the coupling is weak ($\Omega/\Delta < 1$), and the detuning is varied from $\Delta = 1E_r$ to $\Delta = 2.5E_r$. As theoretically expected, the emission from the initial coherent state is suppressed (fig. 6.1 (A)) which is different from the initial incoherent case (fig. 6.1 (B)) similar to the one studied previously (see sec. 4.4, 4.5). In case of the initial coherent state, we also expect the superradient phenomena for a certain detuning ($\Delta = 4E_r$ for this case) which is not shown here. It will be interesting to study the collective behavior more precisely, and also with controlling the superradiant condition.

Coupling scan

Still, there is a practical limitation to this experiment, which is the presence of empty quantum emitters. This was already the case for the spontaneous decay experiment in sec.4.4 that the empty quantum emitter (re-)absorbs the propagating matter-wave from the neighboring sites. This reabsorption can be very critical for the measurement of superradiant since it will limit any collective motion by eliminating the emitted matter-wave. This concern becomes more serious if combined with the non-uniform lattice system in practice from the harmonic trap, see fig. 6.2 (A).

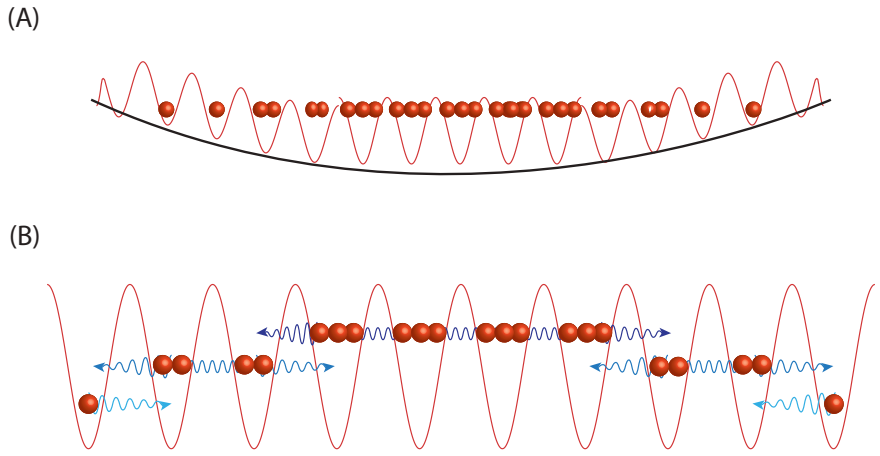

Figure 6.2: (A) Atoms located in the lattice under the harmonic trap potential. The black solid line represents the harmonic trap potential, red line is an optical lattice in 1D that confines red atoms. (B) Illustration of superradiant experiment scheme. Three colored arrows represents the emitted matter-wave (radiant) where they occur in different sequential time zone (dark blue $\rightarrow$ light blue) to avoid re-absorption from the neighboring sites.

This non-box potential shifts up the lowest energy of the edge side, which eventually induces the non-uniform atom population for each site. Thus any Dicke-related model that requires a uniform site population (mostly $< n_i >= 1$) is not directly applicable (or hard to expect clean measurement), since the presence of the empty sites (which is a ground-state quantum emitter) at the edge prohibits the analogy to the Dicke state that requires the same number of emitters and atoms. A similar problem can also occur in any other cases of lattice with non-uniformly populated atoms.

Here, we propose a concept that might be able to solve the problem.

Fig. 6.2 (B) shows a schematic illustration of the idea. Instead of populating on average one atom per site, we start with relatively many atoms per site $n_{avg} = 2 \sim 3$ with a very tight confinement from the lattice. Then each of lattice site will have a different energy from the onsite-interaction energy shift depending on the populated atom number. To induce the collective radiation, starting from the frequency that couples the highest atom number populated site, one can sweep the coupling resonance frequency (detuning) in a quantized way with the corresponding energy shift ($n = 3$ to $n = 2$, and then $n = 1$).

With this quantized detuning scan, when the emitted matter-wave from the highly populated site reaches to the next site, the detuning is lowered so that only the next populated site can emit without the re-absorption. The key here is thus the control of changing the detuning of coupling on a proper time corresponding to the emitted matter-wave, and this will be controlled by tuning the momentum of the matter-wave.

This proposed technique should be widely applicable since it does not necessarily assume the harmonic trap. The drawback is, however, that the time window of the measurement is limited by the atom number (or the maximum onsite energy) since once the coupling frequency reaches the $n = 1$ case, there is no other way to lower the coupling frequency to prohibit re-absorption. In practice, about 40,000 atoms will provide $n = 4$ atoms per site in the center of the harmonic trap, and this gives 4 emission cycles until the frequency sweep reaches the lowest order, which is long enough and the technique is indeed applicable. However this is not the case for the experiment that starts with a relatively small atom number ($\lesssim 1.2 \times 10^4$).

6.1.2 State purification

Much of the work described in this dissertation is focused on the emitted blue atoms, and red atoms are only used as a measure of the population dynamics of quantum emitter. If we focus on the red state, however, we can also study the coherent state of the untransferred red atoms. Especially since we know that the coherence of the initial state changes the emission of the blue atoms, we can use this in a way to purify the initial state.

In detail, in case of the localized red atoms as in Ch. 4 where all wave functions of red atoms are incoherent over the sites as a case of Mott-insulator, the red atoms are free to be transferred to emitted blue state via spontaneous decay. This is because the coupling between red and blue state in Weisskopf-Wigner model assumes a single, localized function as an emitter. If we start from a coherent red distribution, however, the situation is different. The coherent atoms form an extended polariton that cannot decay (unless the superraidant condition is met), but all incoherent parts should be able to be

emitted. This might eventually work as a 'purification' of red state as pure coherent system. This is basically what happens in fig. 6.1.

The idea is then pretty straightforward. By positively coupling the red state with the blue state, the incoherent red state will be emitted and what is left in red should only be the coherent state. By comparing the coherence of the red state before/after this state-purification, we can experimentally confirm it.

There are some practical issues though. The first issue is the preparation of an adiabatic coupling. From our previous studies, we know that it is required to couple the red and the blue adiabatically for a system to exhibit the theoretical prediction, and this requires non-negligible time (2.5ms for previous cases) which can induce additional collisional heating. This is also related with the second issue that it is not easy to tell the incoherence of the Mott-insulator regime from the thermalization. It is therefore not trivial to check the coherence of the final state, but more carefully designed experiments in the future will be able to resolve the current technical issue and generate a clear result as the author of this dissertation hope.

6.2 Frictionless impurity motion in 1D

The mobility of impurities in ultracold atomic systems has been studied in a wide range with various platform, since it shows un-intuitive interesting phenomena [172–175]. In this section, we will briefly discuss the plan for an experiment on frictionless motion of impurities in a 1D system. The basic idea is based on [176], that dissipation can be suppressed by tuning the relative scattering length between the impurity and the background atoms.

6.2.1 Critical velocity

Since we will discuss the motion of impurity, it is crucial to understand the critical velocity. We here start from the very basic description of the BEC; the Gross-Pitaevskii equation

$$i\hbar\dot{\phi} = \left[-\frac{\hbar^2}{2m}\nabla^2 + V_{trap}(r) + g|\phi|^2\right]\phi \tag{6.1}$$

where $g = 4\pi\hbar^2 a/m$ is an interaction parameter and a is the scattering length.

In the presence of the weak perturbation like density dip, $\phi = \phi_0 + \delta\phi$, we can expand the eq. 6.1 with the ansatz of Bogoliubov transformation [141]

$$\delta\phi = e^{-i\mu t/\hbar}(u(r)e^{-i\omega t} - v^*(r)e^{i\omega t}) \tag{6.2}$$

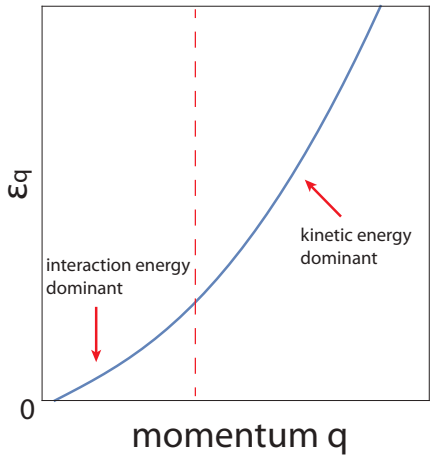

Figure 6.3: Dispersion of Bogoliubov excitation. Depends on the momentum q, the ratio of corresponding kinetic energy $(\hbar q)^2/2m$ and the interaction energy gn_0 gives two regime in the dispersion. For small q, the dispersion relation is linear and the slope gives the speed of sound v_S whereas large q gives parabolic free-particle like dispersion.

and with the assumption of the perturbation as a running wave $u(r) \propto u_q e^{iq\cdot r}$, which indeed gives the dispersion relation of the Bogoliubov excitation

$$\omega(q) = \frac{1}{\hbar}\sqrt{\frac{(\hbar q)^2}{2m}\left(\frac{(\hbar q)^2}{2m} + 2gn_0\right)} \tag{6.3}$$

as shown in fig. 6.3. The two terms inside the square-root gives two extreme limits. For large q, the dispersion relation is more or less quadratic, corresponding to the excitation of a free particle. On the other hand, small q gives the linear (sound-like) dispersion relation near 0 as

$$\omega(q) \backsimeq q\sqrt{\frac{gn_0}{m}}, \tag{6.4}$$

from which we can define the speed of sound as $c_S = \sqrt{gn_0/m}$.

We now can apply the Landau criterion [177] to this dispersion relation, the minimum (critical) velocity for excitation is given as

$$v \leq \frac{\epsilon_q}{p} = v_{min} \tag{6.5}$$

from the resonant excitation (in moving impurity frame) $\epsilon_q(v) = 0$ that gives

$\epsilon_q - \boldsymbol{p}\cdot\boldsymbol{v} = 0$ where ϵ_q is the dispersion relation given by eq. 6.3. When the velocity of the impurity is less than the minimum velocity ($v < v_{min}$), the motion of impurity cannot excite the BEC. Note that for $v > v_{min}$ in 3D, the excitation comes off at an angle.

This critical velocity depends on the regime as discussed above. In a case of large q, i.e. kinetic energy is dominant and the interaction is negligible ($\frac{(\hbar q)^2}{2m} \gg 2gn_0$), the critical velocity is proportional to p which means that the effective critical velocity is zero. Thus any motion in this regime will create excitation, which is very intuitive. For small q regime, the strongly interacting case ($\frac{(\hbar q)^2}{2m} \ll 2gn_0$), the critical velocity is indeed given by the speed of sound v_S from eq.6.4. Thus the impurity motion that is slower than v_S will not create excitation, i.e. there is no heating from the motion.

However, this is only the case for 3D system, unfortunately. 1D has a totally different physics for the impurity motion, and we will discuss it in following subsection.

6.2.2 Basic description of 1D system

To discuss the specialty of 1D, let us first take a look the basic description of 1D. In 1D system such as in a lattice tube, the Hamiltonian is given as [141, 178, 179]

$$H_{1D} = -\sum_j \frac{\hbar^2}{2m}\partial_{z_j}^2 + \sum_{i<j} g_{1D}\delta(z_i - z_j) \tag{6.6}$$

where i, j are the particle indices, $g_{1D} = \frac{\hbar^2}{m}\left[\frac{2a}{a_\perp^2}\right]$ is the interaction parameter and a is the related scattering length.

We can compare the two different energies here: the interaction energy $E_{int} = n_{1D}g_{1D}$ and the kinetic energy $E_{kin} = \frac{\hbar^2}{2m}\left(\frac{\pi}{n_{1D}}\right)^2$. From the ratio, one can extract the Lieb-Liniger parameter γ [180] as

$$\frac{E_{int}}{E_{kin}} = \frac{2}{\pi}\left(\frac{2a}{a_\perp^2}\right)n_{1D} \equiv \frac{2}{\pi}\gamma \tag{6.7}$$

where n is the atom number. The system is in the superfluid regime when $\gamma \ll 1$, while $\gamma \gg 1$ gives the Tonk-Girardeau (TG) regime [181, 182].

In TG regime, there are many interesting studies for the impurity such as quantum transport phenomena [183] and induced Bloch oscillation [175]. However those studies are based on the property of impurity as an obstacle that changes the dynamics of the environment, and this is generally true because any motion in 1D will eventually create an excitation no matter with the

speed of the impurity. At a glance, this looks like a contradiction with eq.6.5, the critical velocity. However, this is due to the unique property of 1D system which does not have enough degrees of freedom to resolve the quantum fluctuation. Based on [184], there is a drag force on impurity in 1D system even below the critical velocity that induces the energy dissipation, the quantum fluctuation. This force is due to the quantum fluctuations that is reflected from the impurity for each side.

6.2.3 Yang-Gaudin model toward frictionless motion

There is a way, however, to overcome the inevitable excitation from the motion of the impurity. Yang and Gaudin's work [185, 186] in 1960s gives us a clue that in an integrable system with equal mass, the friction can be suppressed. The recent research [176] calculated from the idea and claimed that the friction constant κ is given by

$$\kappa \sim T^4 \left(\frac{a_{bb}}{a_{rb}} - 1 \right)^2 \tag{6.8}$$

where a is the scattering length between subscripts r and b, which denotes each of the two constituents of the system respectively, and T is the system temperature. The integrability is naturally provided by the ultracold atom system in 1D, since s-wave scattering is the only effective collision in TG limit.

Thus by controlling the scattering length between the impurity and the bath as equal to the one between bath atoms, one can make the friction negligible, i.e. dissipation-free impurity motion. Using the pair of $|2,0\rangle$ (bath) and $|1,1\rangle$ (impurity) might be the most appropriate choice since the scattering length of $|1,1\rangle \leftrightarrow |1,1\rangle$ and $|1,1\rangle \leftrightarrow |2,0\rangle$ are compatible (100.4 and 97.7, respectively [187]). The difference can be adjusted by using the Feshbach resonance that gives

$$a(B) = a_{BG} \left(\frac{\Delta}{B - B_0} \right) \tag{6.9}$$

where B is the bias magnetic field and Δ is the difference of magnetic field from the resonance [37]. From the calculation, $\sim$ 9G of bias magnetic field brings the two scattering length to the same value.

6.3 Technical development

This section will explain the technical improvements and/or efforts in the direction of such experiments. The work in the following subsections describes

some earlier work of the author of dissertation that can be applied for future experiment (see previous section, sec.6.2). The other minor technical works that might be potentially useful in the future are noted in the appendix (A).

6.3.1 Moving lattice system

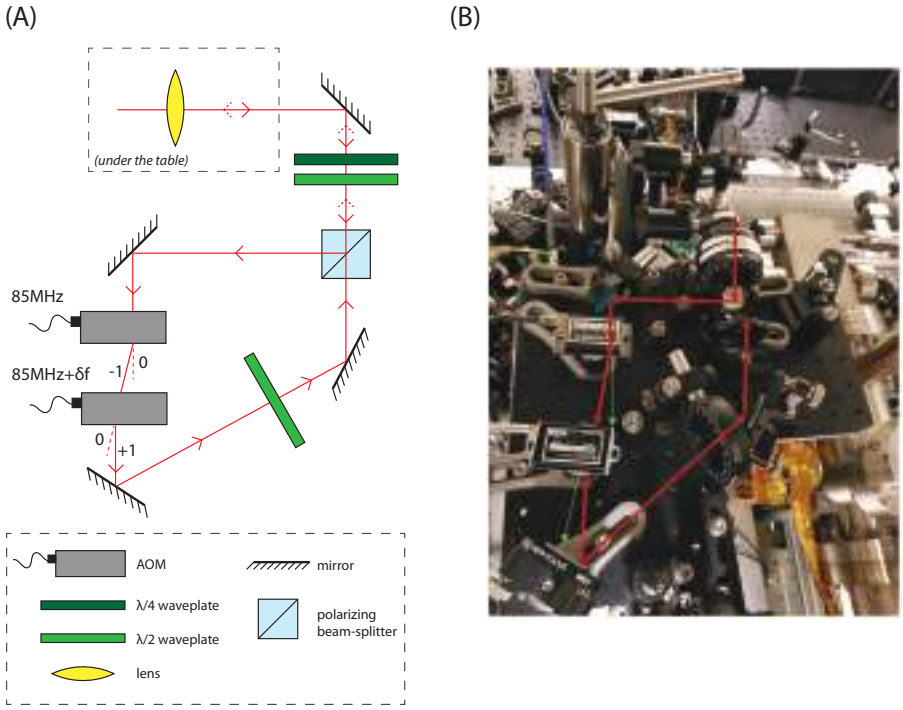

Figure 6.4: Moving state-dependent lattice setup. (A) Illustration of the setup. The structure is similar to that discussed in the thesis of B. Gadway (2012), but the system has been re-built from scratch with modified details. (B) Experimental realization of (A). Red line with arrows describes the guided beam path. Green arrows after each AOM shows the non-deflected path, and we are taking the -1 and the $+1$ order of diffraction for each AOM (this is the opposite order from the plan depicted in (A).

There are several ways to launch the atoms along the tube such as giving a momentum kick. In order to control the motion precisely, however, it is better to control the confining lattice itself. In our target experiment, especially, we only want to make a relative movement for the impurity, i.e. a certain hyperfine state, we need to move the state-dependent lattice.

The mechanism of moving lattice system which follows an earlier implementation [111] is quite simple as shown in fig. 6.4 (A). Since the optical lattice is based on the standing wave, if there is a slight frequency difference between the beams generating the lattice, the node moves together. To achieve this, we used acousto-optic modulator (AOM) for shifting the frequency slightly. When the light passes through AOM, the frequency for the diffracted order is changed by absorbing the phonon that AOM is driven by, which is generally around 80MHz (In our setup, we use 85MHz for optimizing the diffraction efficiency). Since the retro-reflecting laser should have equal polarization and wavelength to be interfered with the forwarding laser, double-path AOM system is required; by choosing -1 and $+1$ diffraction order for each of AOM path, the total wavelength is basically unchanged. Fig. 6.4 (B) shows the realized setup for the moving state-dependent lattice system. The choice of AOM order is different from fig. 6.4 (A) due to the practical reasons, which does not affect to the result.

We here apply the additional frequency δf which is negligibly small but only large enough to make the optical lattice moving with the speed of $v = \delta f \lambda/2$ for fixed f. If we modulate the frequency δf in time domain, we can even accelerate the moving lattice. This can be used to double or cancel out the gravity by moving lattice in z-axis.

Bibliography

[1] A. Einstein. Quantentheorie des einatomigen idealen Gases. *Sitzungsber. Preuss. Akad.*, pages 261–267, 1924.

[2] S. N. Bose. Plancks Gesetz und Lichtquantenhypothese. *Z. Phys.*, 26: 178ñ–181, 1924.

[3] F. Dalfovo, S. Giorgini, L. P. Pitaevskii, and S. Stringari. Theory of Bose–Einstein condensation in trapped gases. *Rev. Mod. Phys.*, 71:463–512, 1999.

[4] M. H. Anderson, J. R. Ensher, M. R. Matthews, C. E. Wieman, and E. A. Cornell. Observation of Bose–Einstein condensation in a dilute atomic vapor. *Science*, 269:198–201, 1995.

[5] C. C. Bradley, C. A. Sackett, J. J. Tollett, and R. G. Hulet. Evidence of Bose–Einstein condensation in an atomic gas with attractive interactions. *Phys. Rev. Lett.*, 75:1687–1690, 1995.

[6] K. B. Davis, M. O. Mewes, M. R. Andrews, N. J. van Druten, D. S. Durfee, D. M. Kurn, and W. Ketterle. Bose–Einstein condensation in a gas of sodium atoms. *Phys. Rev. Lett.*, 75:3969–3973, 1995.

[7] C. C. Bradley, C. A. Sackett, and R. G. Hulet. Bose–Einstein condensation of lithium: Observation of limited condensate number. *Phys. Rev. Lett.*, 78:985–989, 1997.

[8] Enrico Fermi. Zur Quantelung des idealen einatomigen Gases. *Zeitschrift für Physik*, 36(11-12):902–912, 1926.

[9] Paul Adrien Maurice Dirac. On the theory of quantum mechanics. *Prococeedings of the Royal Society of London A*, 112(762):661–677, 1926.

[10] S. Giorgini, L. P. Pitaevskii, and S. Stringari. Theory of ultracold atomic Fermi gases. *Rev. Mod. Phys.*, 80:1215–1274, 2008.

[11] B. DeMarco and D. S. Jin. Onset of Fermi degeneracy in a trapped atomic gas. *Science*, 285:1703–1706, 1999.

[12] Giovanni Modugno, Gabriele Ferrari, Giacomo Roati, Robert J Brecha, A Simoni, and Massimo Inguscio. Bose-Einstein condensation of potassium atoms by sympathetic cooling. *Science*, 294(5545):1320–1322, 2001.

[13] Tino Weber, Jens Herbig, Michael Mark, Hanns-Christoph Nägerl, and Rudolf Grimm. Bose-Einstein condensation of cesium. *Science*, 299 (5604):232–235, 2003.

[14] Sebastian Kraft, Felix Vogt, Oliver Appel, Fritz Riehle, and Uwe Sterr. Bose-Einstein condensation of alkaline earth atoms: Ca 40. *Physical Review Letters*, 103(13):130401, 2009.

[15] Simon Stellmer, Meng Khoon Tey, Bo Huang, Rudolf Grimm, and Florian Schreck. Bose-Einstein condensation of strontium. *Physical Review Letters*, 103(20):200401, 2009.

[16] YN Martinez De Escobar, Pascal Gerry Mickelson, M Yan, BJ DeSalvo, Sarah B Nagel, and TC Killian. Bose-Einstein Condensation of Sr 84. *Physical Review Letters*, 103(20):200402, 2009.

[17] Dale G Fried, Thomas C Killian, Lorenz Willmann, David Landhuis, Stephen C Moss, Daniel Kleppner, and Thomas J Greytak. Bose-Einstein condensation of atomic hydrogen. *Physical Review Letters*, 81 (18):3811, 1998.

[18] Alice Robert, Olivier Sirjean, Antoine Browaeys, Julie Poupard, Stephan Nowak, Denis Boiron, Christoph I Westbrook, and Alain Aspect. A Bose-Einstein condensate of metastable atoms. *Science*, 292(5516):461–464, 2001.

[19] Axel Griesmaier, Jörg Werner, Sven Hensler, Jürgen Stuhler, and Tilman Pfau. Bose-Einstein condensation of chromium. *Physical Review Letters*, 94(16):160401, 2005.

[20] Yosuke Takasu, Kenichi Maki, Kaduki Komori, Tetsushi Takano, Kazuhito Honda, Mitsutaka Kumakura, Tsutomu Yabuzaki, and Yoshiro Takahashi. Spin-singlet Bose-Einstein condensation of two-electron atoms. *Physical Review Letters*, 91(4):040404, 2003.

[21] K Aikawa, A Frisch, M Mark, S Baier, A Rietzler, R Grimm, and F Ferlaino. Bose-Einstein condensation of erbium. *Physical Review Letters*, 108(21):210401, 2012.

[22] Mingwu Lu, Nathaniel Q Burdick, Seo Ho Youn, and Benjamin L Lev. Strongly dipolar Bose-Einstein condensate of dysprosium. *Physical Review Letters*, 107(19):190401, 2011.

[23] MR Andrews, CG Townsend, H-J Miesner, DS Durfee, DM Kurn, and W Ketterle. Observation of interference between two Bose condensates. *Science*, 275(5300):637–641, 1997.

[24] M-O Mewes, MR Andrews, DM Kurn, DS Durfee, CG Townsend, and W Ketterle. Output coupler for Bose-Einstein condensed atoms. *Physical Review Letters*, 78(4):582, 1997.

[25] Immanuel Bloch, Theodor W Hänsch, and Tilman Esslinger. Atom laser with a cw output coupler. *Physical Review Letters*, 82(15):3008, 1999.

[26] Edward W Hagley, Lu Deng, M Kozuma, J Wen, Kristian Helmerson, SL Rolston, , and William D Phillips. A well-collimated quasi-continuous atom laser. *Science*, 283(5408):1706–1709, 1999.

[27] S. Inouye, A. P. Chikkatur, D. M. Stamper-Kurn, J. Stenger, D. E. Pritchard, and W. Ketterle. Superradiant Rayleigh scattering from a Bose–Einstein condensate. *Science*, 285:571, 1999.

[28] D. Schneble, Y. Torii, M. Boyd, E. W. Streed, D. E. Pritchard, and W. Ketterle. The onset of matter-wave amplification in a superradiant Bose–Einstein condensate. *Science*, 300:457, 2003.

[29] M-O Mewes, MR Andrews, NJ Van Druten, DM Kurn, DS Durfee, CG Townsend, and W Ketterle. Collective excitations of a Bose-Einstein condensate in a magnetic trap. *Physical Review Letters*, 77(6):988, 1996.

[30] MR Andrews, DM Kurn, H-J Miesner, DS Durfee, CG Townsend, S Inouye, and W Ketterle. Propagation of sound in a Bose-Einstein condensate. *Physical Review Letters*, 79(4):553, 1997.

[31] S Burger, K Bongs, S Dettmer, W Ertmer, K Sengstock, A Sanpera, GV Shlyapnikov, and M Lewenstein. Dark solitons in Bose-Einstein condensates. *Physical Review Letters*, 83(25):5198, 1999.

[32] Kevin E Strecker, Guthrie B Partridge, Andrew G Truscott, and Randall G Hulet. Formation and propagation of matter-wave soliton trains. *Nature*, 417(6885):150, 2002.

[33] Michael Robin Matthews, Brian P Anderson, PC Haljan, DS Hall, CE Wieman, and Eric A Cornell. Vortices in a bose-einstein condensate. *Physical Review Letters*, 83(13):2498, 1999.

[34] K. W. Madison, F. Chevy, V. Bretin, and J. Dalibard. Stationary states of a rotating Bose-Einstein condensate: Routes to vortex nucleation. *Phys. Rev. Lett.*, 86:4443–4446, 2001.

[35] Jamil R Abo-Shaeer, Chandra Raman, Johnny M Vogels, and Wolfgang Ketterle. Observation of vortex lattices in bose-einstein condensates. *Science*, 292(5516):476–479, 2001.

[36] S Inouye, MR Andrews, J Stenger, H-J Miesner, DM Stamper-Kurn, and W Ketterle. Observation of Feshbach resonances in a Bose-Einstein condensate. *Nature*, 392(6672):151, 1998.

[37] C. Chin, R. Grimm, P. Julienne, and E. Tiesinga. Feshbach resonances in ultracold gases. *Rev. Mod. Phys.*, 82:1225–1286, 2010.

[38] J. Stenger, S. Inouye, A. P. Chikkatur, D. M. Stamper-Kurn, D. E. Pritchard, and W. Ketterle. Bragg spectroscopy of a Bose-Einstein condensate. *Phys. Rev. Lett.*, 82:4569–4573, 1999.

[39] M. Bartenstein, A. Altmeyer, S. Riedl, S. Jochim, C. Chin, J. Hecker Denschlag, and R. Grimm. Crossover from a molecular Bose–Einstein condensate to a degenerate Fermi gas. *Phys. Rev. Lett.*, 92:120401, 2004.

[40] G. B. Partridge, K. E. Strecker, R. I. Kamar, M. W. Jack, and R. G. Hulet. Molecular probe of pairing in the BEC-BCS crossover. *Phys. Rev. Lett.*, 95:020404, 2005.

[41] K-K Ni, S Ospelkaus, D Wang, G Quéméner, B Neyenhuis, MHG De Miranda, JL Bohn, J Ye, and DS Jin. Dipolar collisions of polar molecules in the quantum regime. *Nature*, 464(7293):1324, 2010.

[42] S Ospelkaus, K-K Ni, D Wang, MHG De Miranda, B Neyenhuis, G Quéméner, PS Julienne, JL Bohn, DS Jin, and J Ye. Quantum-state controlled chemical reactions of ultracold potassium-rubidium molecules. *Science*, 327(5967):853–857, 2010.

[43] M. A. Baranov, A. Micheli, S. Ronen, and P. Zoller. Bilayer superfluidity of fermionic polar molecules: Many-body effects. *Phys. Rev. A*, 83: 043602, 2011.

[44] Bo Yan, Steven A Moses, Bryce Gadway, Jacob P Covey, Kaden RA Hazzard, Ana Maria Rey, Deborah S Jin, and Jun Ye. Observation of dipolar spin-exchange interactions with lattice-confined polar molecules. *Nature*, 501(7468):521, 2013.

[45] Yu. B. Ovchinnikov, J. H. Müller, M. R. Doery, E. J. D. Vredenbregt, K. Helmerson, S. L. Rolston, and W. D. Phillips. Diffraction of a released Bose-Einstein condensate by a pulsed standing light wave. *Phys. Rev. Lett.*, 83:284–287, 1999.

[46] O. Morsch and M. Oberthaler. Dynamics of Bose-Einstein condensates in optical lattices. *Rev. Mod. Phys.*, 78:179–215, 2006.

[47] Richard P Feynman. Simulating physics with computers. *International Journal of Theoretical Physics*, 21(6-7):467–488, 1982.

[48] J. Hubbard and Brian Hilton Flowers. Electron correlations in narrow energy bands. *Proceedings of the Royal Society of London. Series A. Mathematical and Physical Sciences*, 276(1365):238–257, 1963. doi: 10.1098/rspa.1963.0204.

[49] M. Greiner, O. Mandel, T. Esslinger, T. W. Hänsch, and I. Bloch. Quantum phase transition from a superfluid to a Mott insulator in a gas of ultracold atoms. *Nature*, 415:39, 2002.

[50] I. Bloch, J. Dalibard, and W. Zwerger. Many-body physics with ultracold gases. *Rev. Mod. Phys.*, 80:885–964, 2008.

[51] Patrick Windpassinger and Klaus Sengstock. Engineering novel optical lattices. *Reports on Progress in Physics*, 76(8):086401, jul 2013. doi: 10.1088/0034-4885/76/8/086401.

[52] Omjyoti Dutta, Mariusz Gajda, Philipp Hauke, Maciej Lewenstein, Dirk-Sören Lühmann, Boris A Malomed, Tomasz Sowiński, and Jakub Zakrzewski. Non-standard hubbard models in optical lattices: a review. *Reports on Progress in Physics*, 78(6):066001, may 2015. doi: 10.1088/0034-4885/78/6/066001.

[53] K. Singh, K. Saha, S. A. Parameswaran, and D. M. Weld. Fibonacci optical lattices for tunable quantum quasicrystals. *Phys. Rev. A*, 92: 063426, Dec 2015. doi: 10.1103/PhysRevA.92.063426. URL `https://link.aps.org/doi/10.1103/PhysRevA.92.063426`.

[54] Konrad Viebahn, Matteo Sbroscia, Edward Carter, Jr-Chiun Yu, and Ulrich Schneider. Matter-wave diffraction from a quasicrystalline optical lattice. *Phys. Rev. Lett.*, 122:110404, Mar 2019. doi: 10.1103/PhysRevLett.122.110404. URL `https://link.aps.org/doi/10.1103/PhysRevLett.122.110404`.

[55] Gregor Jotzu, Michael Messer, Rémi Desbuquois, Martin Lebrat, Thomas Uehlinger, Daniel Greif, and Tilman Esslinger. Experimental realization of the topological Haldane model with ultracold fermions. *Nature*, 515(7526):237, 2014.

[56] Monika Aidelsburger, Marcos Atala, Michael Lohse, Julio T Barreiro, B Paredes, and Immanuel Bloch. Realization of the Hofstadter Hamiltonian with ultracold atoms in optical lattices. *Physical Review Letters*, 111(18):185301, 2013.

[57] Hirokazu Miyake, Georgios A Siviloglou, Colin J Kennedy, William Cody Burton, and Wolfgang Ketterle. Realizing the Harper Hamiltonian with laser-assisted tunneling in optical lattices. *Physical Review Letters*, 111 (18):185302, 2013.

[58] Y.-J. Lin, K. Jiménez-Garcia, and I. B. Spielman. Spin-orbit-coupled Boseñ-Einstein condensates. *Nature*, 471:83–ñ86, 2011.

[59] Victor Galitski and Ian B Spielman. Spin-orbit coupling in quantum gases. *Nature*, 494(7435):49, 2013.

[60] Lianghui Huang, Zengming Meng, Pengjun Wang, Peng Peng, Shao-Liang Zhang, Liangchao Chen, Donghao Li, Qi Zhou, and Jing Zhang. Experimental realization of two-dimensional synthetic spin-orbit coupling in ultracold Fermi gases. *Nature Physics*, 12(6):540, 2016.

[61] Daniel Greif, Thomas Uehlinger, Gregor Jotzu, Leticia Tarruell, and Tilman Esslinger. Short-range quantum magnetism of ultracold fermions in an optical lattice. *Science*, 340(6138):1307–1310, 2013.

[62] Russell A Hart, Pedro M Duarte, Tsung-Lin Yang, Xinxing Liu, Thereza Paiva, Ehsan Khatami, Richard T Scalettar, Nandini Trivedi, David A Huse, and Randall G Hulet. Observation of antiferromagnetic correlations in the Hubbard model with ultracold atoms. *Nature*, 519(7542): 211, 2015.

[63] Anton Mazurenko, Christie S Chiu, Geoffrey Ji, Maxwell F Parsons, Márton Kanász-Nagy, Richard Schmidt, Fabian Grusdt, Eugene Demler, Daniel Greif, and Markus Greiner. A cold-atom Fermi-Hubbard antiferromagnet. *Nature*, 545(7655):462, 2017.

[64] Timon A Hilker, Guillaume Salomon, Fabian Grusdt, Ahmed Omran, Martin Boll, Eugene Demler, Immanuel Bloch, and Christian Gross. Revealing hidden antiferromagnetic correlations in doped Hubbard chains via string correlators. *Science*, 357(6350):484–487, 2017.

[65] J. Billy, V. Josse, Z. Zuo, A. Bernard, B. Hambrecht, P. Lugan, D. Clément, L. Sanchez-Palencia, P. Bouyer, and A. Aspect. Direct observation of Anderson localization of matter waves in a controlled disorder. *Nature*, 453:891, 2008.

[66] Bryce Gadway, Daniel Pertot, Jeremy Reeves, Matthias Vogt, and Dominik Schneble. Glassy behavior in a binary atomic mixture. *Physical Review Letters*, 107:145306, Sep 2011.

[67] P. W. Anderson. Absence of diffusion in certain random lattices. *Phys. Rev.*, 109:1492–1505, 1958.

[68] G. Roati, C. D'Errico, L. Fallani, M. Fattori, C. Fort, M. Zaccanti, G. Modugno, M. Modugno, and M. Inguscio. Anderson localization of a non-interacting Bose–Einstein condensate. *Nature*, 453:895, 2008.

[69] S. S. Kondov, W. R. McGehee, J. J. Zirbel, and B. DeMarco. Three-dimensional Anderson localization of ultracold matter. *Science*, 334: 66–68, 2011.

[70] S. Aubry and G. André. Analyticity breaking and Anderson localization in incommensurate lattices. *Ann. Israel Phys. Soc.*, 3:133–140, 1980.

[71] Sajeev John. Electromagnetic absorption in a disordered medium near a photon mobility edge. *Phys. Rev. Lett.*, 53:2169–2172, Nov 1984. doi: 10.1103/PhysRevLett.53.2169.

[72] Sajeev John. Electromagnetic absorption in a disordered medium near a photon mobility edge. *Physical Review Letters*, 53:2169–2172, Nov 1984.

[73] Giulia Semeghini, Manuele Landini, Patricia Castilho, Sanjukta Roy, Giacomo Spagnolli, Andreas Trenkwalder, Marco Fattori, Massimo Inguscio, and Giovanni Modugno. Measurement of the mobility edge for 3d anderson localization. *Nature Physics*, 11(7):554–559, 2015.

[74] Eric J. Meier, Fangzhao Alex An, Alexandre Dauphin, Maria Maffei, Pietro Massignan, Taylor L. Hughes, and Bryce Gadway. Observation of the topological anderson insulator in disordered atomic wires. *Science*, 362(6417):929–933, 2018. ISSN 0036-8075. doi: 10.1126/science.aat3406. URL `https://science.sciencemag.org/content/362/6417/929`.

[75] Waseem S Bakr, Jonathon I Gillen, Amy Peng, Simon Fölling, and Markus Greiner. A quantum gas microscope for detecting single atoms in a hubbard-regime optical lattice. *Nature*, 462(7269):74–77, 2009.

[76] W. S. Bakr, A. Peng, M. E. Tai, R. Ma, J. Simon, J. I. Gillen, S. Fölling, L. Pollet, and M. Greiner. Probing the superfluid-to-Mott insulator transition at the single-atom level. *Science*, 329:547–550, 2010.

[77] J. F. Sherson, C. Weitenberg, M. Endres, M. Cheneau, I. Bloch, and S. Kuhr. Single-atom-resolved fluorescence imaging of an atomic Mott insulator. *Nature*, 467:68–72, 2010.

[78] Lawrence W Cheuk, Matthew A Nichols, Melih Okan, Thomas Gersdorf, Vinay V Ramasesh, Waseem S Bakr, Thomas Lompe, and Martin W Zwierlein. Quantum-gas microscope for fermionic atoms. *Physical Review Letters*, 114(19):193001, 2015.

[79] Maxwell F Parsons, Florian Huber, Anton Mazurenko, Christie S Chiu, Widagdo Setiawan, Katherine Wooley-Brown, Sebastian Blatt, and Markus Greiner. Site-resolved imaging of fermionic Li 6 in an optical lattice. *Physical Review Letters*, 114(21):213002, 2015.

[80] Ahmed Omran, Martin Boll, Timon A Hilker, Katharina Kleinlein, Guillaume Salomon, Immanuel Bloch, and Christian Gross. Microscopic observation of Pauli blocking in degenerate fermionic lattice gases. *Physical Review Letters*, 115(26):263001, 2015.

[81] Elmar Haller, James Hudson, Andrew Kelly, Dylan A Cotta, Bruno Peaudecerf, Graham D Bruce, and Stefan Kuhr. Single-atom imaging of fermions in a quantum-gas microscope. *Nature Physics*, 11(9):738, 2015.

[82] Daniel Pertot, Bryce Gadway, and Dominik Schneble. Collinear four-wave mixing of two-component matter waves. *Physical Review Letters*, 104:200402, May 2010.

[83] Bryce Gadway, Daniel Pertot, René Reimann, and Dominik Schneble. Superfluidity of interacting bosonic mixtures in optical lattices. *Physical Review Letters*, 105:045303, Jul 2010.

[84] Bryce Gadway, Daniel Pertot, Jeremy Reeves, and Dominik Schneble. Probing an ultracold-atom crystal with matter waves. *Nature Physics*, 8(7):544–549, 2012. ISSN 1745-2473. doi: 10.1038/nphys2320.

[85] J. Reeves, L. Krinner, M. Stewart, A. Pazmiño, and D. Schneble. Nonadiabatic diffraction of matter waves. *Physical Review A*, 92:023628, Aug 2015. doi: 10.1103/PhysRevA.92.023628.

[86] L. Krinner, M. Stewart, A. Pazmiño, J. Kwon, and D. Schneble. Spontaneous emission of matter waves from a tunable open quantum system. *Nature*, 559:589–592, Jul 2018. doi: 10.1038/s41586-018-0348-z. URL `https://www.nature.com/articles/s41586-018-0348-z`.

[87] Michael Stewart, Joonhyuk Kwon, Alfonso Lanuza, and Dominik Schneble. Dynamics of matter-wave quantum emitters in a structured vacuum. *Physical Review Research*, 2(4):043307, 2020. doi: 10.1103/PhysRevResearch.2.043307.

[88] Joonhyuk Kwon, Youngshin Kim, Alfonso Lanuza, and Dominik Schneble. Formation of matter-wave polaritons in an optical lattice. *arXiv preprint arXiv:2109.02243*, 2021.

[89] V. Weisskopf and E. Wigner. Berechnung der natürlichen linienbreite auf grund der diracschen lichttheorie. *Zeitschrift für Physik*, 63(1):54–73, 1930.

[90] Vladimir P Bykov. Spontaneous emission from a medium with a band spectrum. *Soviet Journal of Quantum Electronics*, 4(7):861, 1975.

[91] J. J. Hopfield. Theory of the contribution of excitons to the complex dielectric constant of crystals. *Phys. Rev.*, 112:1555–1567, Dec 1958. doi: 10.1103/PhysRev.112.1555.

[92] S.I. Pekar. Theory of electromagnetic waves in a crystal with excitons. *Journal of Physics and Chemistry of Solids*, 5(1):11–22, 1958. ISSN 0022-3697. doi: https://doi.org/10.1016/0022-3697(58)90127-6.

[93] D. L. Mills and E. Burstein. Polaritons - electromagnetic modes of media. *Reports on Progress in Physics*, 37(7):817–926, 1974. ISSN 0034-4885. doi: 10.1088/0034-4885/37/7/001.

[94] C. Weisbuch, M. Nishioka, A. Ishikawa, and Y. Arakawa. Observation of the coupled exciton-photon mode splitting in a semiconductor quantum microcavity. *Phys. Rev. Lett.*, 69:3314–3317, Dec 1992. doi: 10.1103/PhysRevLett.69.3314.

[95] D. N. Basov, Ana Asenjo-Garcia, P. James Schuck, Xiaoyang Zhu, and Angel Rubio. Polariton panorama. *Nanophotonics*, 10(1):549–577, 2021. doi: doi:10.1515/nanoph-2020-0449.

[96] Hui Deng, Hartmut Haug, and Yoshihisa Yamamoto. Exciton-polariton bose-einstein condensation. *Rev. Mod. Phys.*, 82:1489–1537, May 2010. doi: 10.1103/RevModPhys.82.1489.

[97] Álvaro Cuevas, Juan Camilo López Carreño, Blanca Silva, Milena De Giorgi, Daniel G. Suárez-Forero, Carlos Sánchez Muñoz, Antonio Fieramosca, Filippo Cardano, Lorenzo Marrucci, Vittorianna Tasco, Giorgio Biasiol, Elena del Valle, Lorenzo Dominici, Dario Ballarini, Giuseppe Gigli, Paolo Mataloni, Fabrice P. Laussy, Fabio Sciarrino, and Daniele Sanvitto. First observation of the quantized exciton-polariton field and effect of interactions on a single polariton. *Science Advances*, 4(4), 2018. doi: 10.1126/sciadv.aao6814.

[98] I. Carusotto, T. Volz, and A. Imamoğlu. Feshbach blockade: Single-photon nonlinear optics using resonantly enhanced cavity polariton scattering from biexciton states. *EPL (Europhysics Letters)*, 90(3):37001, 2010. ISSN 0295-5075 1286-4854. doi: 10.1209/0295-5075/90/37001. URL `http://dx.doi.org/10.1209/0295-5075/90/37001`.

[99] Michael J. Hartmann, Fernando G. S. L. Brandão, and Martin B. Plenio. Strongly interacting polaritons in coupled arrays of cavities. *Nature Physics*, 2(12):849–855, 2006.

[100] Andrew D. Greentree, Charles Tahan, Jared H. Cole, and Lloyd C. L. Hollenberg. Quantum phase transitions of light. *Nature Physics*, 2(12): 856–861, 2006. ISSN 1745-2481. doi: 10.1038/nphys466.

[101] Iacopo Carusotto and Cristiano Ciuti. Quantum fluids of light. *Reviews of Modern Physics*, 85(1):299–366, 2013.

[102] Iacopo Carusotto, Andrew A. Houck, Alicia J. Kollár, Pedram Roushan, David I. Schuster, and Jonathan Simon. Photonic materials in circuit quantum electrodynamics. *Nature Physics*, 16(3):268–279, 2020.

[103] Changsuk Noh and Dimitris G. Angelakis. Quantum simulations and many-body physics with light. *Reports on Progress in Physics*, 80(1): 016401, 2016. ISSN 0034-4885 1361-6633. doi: 10.1088/0034-4885/80/1/016401.

[104] E. M. Purcell. Spontaneous emission probabilities at radio frequencies. *Physical Review*, 69:681, 1946.

[105] E. Vetsch, D. Reitz, G. Sagué, R. Schmidt, S. T. Dawkins, and A. Rauschenbeutel. Optical interface created by laser-cooled atoms trapped in the evanescent field surrounding an optical nanofiber. *Physical Review Letters*, 104(20):203603, 2010. doi: 10.1103/PhysRevLett.104.203603. URL `https://link.aps.org/doi/10.1103/PhysRevLett.104.203603`.

[106] J. S. Douglas, H Habibian, C. L. Hung, A. V. Gorshkov, H. J. Kimble, and D. E. Chang. Quantum many-body models with cold atoms coupled to photonic crystals. *Nature Photonics*, 9(5):326–331, 2015.

[107] Jonathan D. Hood, Akihisa Goban, Ana Asenjo-Garcia, Mingwu Lu, Su-Peng Yu, Darrick E. Chang, and H. J. Kimble. Atom–atom interactions around the band edge of a photonic crystal waveguide. *Proceedings of the National Academy of Sciences*, 113(38):10507–10512, 2016.

[108] D. E. Chang, J. S. Douglas, A. González-Tudela, C.-L. Hung, and H. J. Kimble. Colloquium: Quantum matter built from nanoscopic lattices of atoms and photons. *Rev. Mod. Phys.*, 90:031002, Aug 2018.

[109] S. G. Albert. Cooling, trapping, and transport of atom clouds in a new BEC apparatus. Master's thesis, Stony Brook University, 2007.

[110] D. A. Pertot. *Two-Component Bosons in State-Dependent Optical Lattices*. PhD thesis, Stony Brook University, 2011.

[111] B. R. Gadway. *Bose Gases in Tailored Optical and Atomic Lattices*. PhD thesis, Stony Brook University, 2012.

[112] J. B. Reeves. *Dynamics of Atomic Matter Waves in Optical Lattices*. PhD thesis, Stony Brook University, 2015.

[113] L. Krinner. *Exploring Spontaneous Emission Phenomena using Ultracold Atomic Matter Waves*. PhD thesis, Stony Brook University, 2018.

[114] A Pazmiño. *Towards studies of the Aubry-Andr e model with ultracold atoms in optical lattices*. PhD thesis, Stony Brook University, 2019.

[115] M Stewart. *Dynamics of Matter-Wave Quantum Emitters in Engineered Reservoirs*. PhD thesis, Stony Brook University, 2020.

[116] Daniel Pertot, Daniel Greif, Stephan Albert, Bryce Gadway, and Dominik Schneble. Versatile transporter apparatus for experiments with optically trapped bose–einstein condensates. *Journal of Physics B: Atomic, Molecular and Optical Physics*, 42(21):215305, 2009.

[117] H. Metcalf and P. van der Straten. *Atoms and Molecules Interacting with Light*. Cambridge University Press, University Printing House, CB2 8BS, United Kingdom, 2016.

[118] D. A. Steck. Rubidium 87 D line data. available online at `http://http://steck.us/alkalidata`. (revision 2.1.4, 23 December 2010).

[119] Paul D Lett, Richard N Watts, Christoph I Westbrook, William D Phillips, Phillip L Gould, and Harold J Metcalf. Observation of atoms laser cooled below the doppler limit. *Physical review letters*, 61(2):169, 1988.

[120] Jean Dalibard and Claude Cohen-Tannoudji. Laser cooling below the doppler limit by polarization gradients: simple theoretical models. *JOSA B*, 6(11):2023–2045, 1989.

[121] A. L. Migdall, J. V. Prodan, W. D. Phillips, T. H. Bergeman, and H. J. Metcalf. First observation of magnetically trapped neutral atoms. *Phys. Rev. Lett.*, 54:2596–2599, 1985.

[122] W. Ketterle, D. S. Durfee, and D. M. Stamper-Kurn. Making, probing, and understanding bose-einstein condensates. *arXiv*, pages 9904034v2 [cond–mat], 1999.

[123] W. Petrich, M. H. Anderson, J. R. Ensher, and E. A. Cornell. Stable, tightly confining magnetic trap for evaporative cooling of neutral atoms. *Phys. Rev. Lett.*, 74:3352–3355, 1995.

[124] G. Breit and I. I. Rabi. Measurement of nuclear spin. *Phys. Rev.*, 38: 2082–2083, 1931.

[125] M.-O. Mewes, M. R. Andrews, D. M. Kurn, D. S. Durfee, C. G. Townsend, and W. Ketterle. Output coupler for Bose-Einstein condensed atoms. *Phys. Rev. Lett.*, 78:582–585, 1997.

[126] Lev Landau. Zur theorie der energieubertragung. ii. *Physikalische Zeitschrift der Sowjetunion*, 2:46–51, 1932.

[127] Clarence Zener. Non-adiabatic crossing of energy levels. *Proceedings of the Royal Society of London. Series A, Containing Papers of a Mathematical and Physical Character*, 137(833):696–702, 1932.

[128] Cosma Rohilla Shalizi. *Advanced Data Analysis from an Elementary Point of View*. Cambridge University Press, 2015.

[129] Ian Jolliffe. *Principal component analysis*. Springer, 2011.

[130] Ivan H. Deutsch and Poul S. Jessen. Quantum-state control in optical lattices. *Phys. Rev. A*, 57:1972–1986, Mar 1998. doi: 10.1103/PhysRevA.57.1972. URL `http://link.aps.org/doi/10.1103/PhysRevA.57.1972`.

[131] R. Grimm, M. Weidemuller, and Y. B. Ovchinnikov. Optical dipole traps for neutral atoms. *Advances in Atomic Molecular, and Optical Physics*, 42:95–170, 2000. ISSN 0065-2199. doi: 10.1016/s1049-250x(08)60186-x. URL `<GotoISI>://WOS:000085557900004`.

[132] Felix Schmidt, Daniel Mayer, Michael Hohmann, Tobias Lausch, Farina Kindermann, and Artur Widera. Precision measurement of the ^{87}Rb tune-out wavelength in the hyperfine ground state $f = 1$ at 790 nm. *Phys. Rev. A*, 93:022507, Feb 2016. doi: 10.1103/PhysRevA.93.022507. URL `https://link.aps.org/doi/10.1103/PhysRevA.93.022507`.

[133] N. W. Ashcroft and N. D. Mermin. *Solid State Physics*. Holt–Saunders International Editions, London, 1976.

[134] W. Zwerger. Mottñ-Hubbard transition of cold atoms in optical lattices. *J. Opt. B: Quantum Semiclass. Opt.*, 5:S9–S16, 2003.

[135] M. P. A. Fisher, P. B. Weichman, G. Grinstein, and D. S. Fisher. Boson localization and the superfluid-insulator transition. *Phys. Rev. B*, 40: 546–570, 1989.

[136] M. Greiner, I. Bloch, O. Mandel, T. W. Hänsch, and T. Esslinger. Exploring phase coherence in a 2D lattice of Bose–Einstein condensates. *Phys. Rev. Lett.*, 87:160405, 2001.

[137] D. Jaksch, C. Bruder, J. I. Cirac, C. W. Gardiner, and P. Zoller. Cold bosonic atoms in optical lattices. *Phys. Rev. Lett.*, 81:3108–3111, 1998.

[138] W. Krauth, M. Caffarel, and J.-P. Bouchaud. Gutzwiller wave function for a model of strongly interacting bosons. *Phys. Rev. B*, 45:3137–3140, 1992.

[139] K. Sheshadri, H. R. Krishnamurthy, R. Pandit, and T. V. Ramakrishnan. Superfluid and insulating phases in an interacting-boson model: Mean-field theory and the RPA. *Europhys. Lett.*, 22:257, 1993.

[140] D. van Oosten, P. van der Straten, and H. T. C. Stoof. Quantum phases in an optical lattice. *Phys. Rev. A*, 63:053601, 2001.

[141] C. J. Pethick and H. Smith. *Bose–Einstein Condensation in Dilute Gases*. Cambridge University Press, New York, 2008.

[142] S. Fölling, A. Widera, T. Müller, F. Gerbier, and I. Bloch. Formation of spatial shell structure in the superfluid to Mott insulator transition. *Phys. Rev. Lett.*, 97:060403, 2006.

[143] G. K. Campbell, J. Mun, M. Boyd, P. Medley, A. E. Leanhardt, L. G. Marcassa, D. E. Pritchard, and W. Ketterle. Imaging the Mott insulator shells by using atomic clock shifts. *Science*, 313(5787):649–652, 2005.

[144] Ulrich Hoeppe, Christian Wolff, Jens Küchenmeister, Jens Niegemann, Malte Drescher, Hartmut Benner, and Kurt Busch. Direct observation of non-markovian radiation dynamics in 3d bulk photonic crystals. *Physical Review Letters*, 108(4):043603, 2012. PRL.

[145] Yanbing Liu and Andrew A. Houck. Quantum electrodynamics near a photonic bandgap. *Nat Phys*, 13(1):48–52, 2017.

[146] Sajeev John. Strong localization of photons in certain disordered dielectric superlattices. *Physical Review Letters*, 58:2486–2489, Jun 1987.

[147] Eli Yablonovitch. Inhibited spontaneous emission in solid-state physics and electronics. *Phys. Rev. Lett.*, 58:2059–2062, May 1987. doi: 10.1103/PhysRevLett.58.2059.

[148] Pierre Meystre and Murray Sargent III. *Elements of Quantum Optics*. Springer Verlag Berlin Heidelberg, 2007.

[149] P. W. Milonni. *The Quantum Vacuum: An Introduction to Quantum Electrodynamics.* Academic Press, Inc., 1994.

[150] Michael Stewart, Ludwig Krinner, Arturo Pazmiño, and Dominik Schneble. Analysis of non-markovian coupling of a lattice-trapped atom to free space. *Physical Review A*, 95:013626, Jan 2017.

[151] Ludwig Krinner, Michael Stewart, Arturo Pazmiño, and Dominik Schneble. In-situ magnetometry for experiments with atomic quantum gases. *Review of Scientific Instruments*, 89:013108, 2018.

[152] Alfonso Lanuza, Joonhyuk Kwon, Youngshin Kim, and Dominik Schneble. Multiband and array effects in matter-wave-based waveguide qed. *arXiv preprint arXiv:2108.11759*, 2021.

[153] C. Schneider, K. Winkler, M. D. Fraser, M. Kamp, Y. Yamamoto, E. A. Ostrovskaya, and S. Höfling. Exciton-polariton trapping and potential landscape engineering. *Reports on Progress in Physics*, 80(1):016503, 2016. ISSN 0034-4885 1361-6633. doi: 10.1088/0034-4885/80/1/016503.

[154] Ruichao Ma, Brendan Saxberg, Clai Owens, Nelson Leung, Yao Lu, Jonathan Simon, and David I. Schuster. A dissipatively stabilized mott insulator of photons. *Nature*, 566(7742):51–57, 2019. ISSN 1476-4687. doi: 10.1038/s41586-019-0897-9.

[155] Michael J. Hartmann. Quantum simulation with interacting photons. *Journal of Optics*, 18(10):104005, 2016. ISSN 2040-8978 2040-8986. doi: 10.1088/2040-8978/18/10/104005.

[156] Neereja M. Sundaresan, Rex Lundgren, Guanyu Zhu, Alexey V. Gorshkov, and Andrew A. Houck. Interacting qubit-photon bound states with superconducting circuits. *Phys. Rev. X*, 9:011021, Feb 2019. doi: 10.1103/PhysRevX.9.011021. URL `https://link.aps.org/doi/10.1103/PhysRevX.9.011021`.

[157] Alexandre Blais, Steven M. Girvin, and William D. Oliver. Quantum information processing and quantum optics with circuit quantum electrodynamics. *Nature Physics*, 16(3):247–256, 2020. ISSN 1745-2481. doi: 10.1038/s41567-020-0806-z.

[158] T Shi, Y-H Wu, A González-Tudela, and J I Cirac. Effective many-body hamiltonians of qubit-photon bound states. *New Journal of Physics*, 20 (10):105005, oct 2018.

[159] Thilo Stöferle, Henning Moritz, Christian Schori, Michael Köhl, and Tilman Esslinger. Transition from a strongly interacting 1d superfluid to a mott insulator. *Physical Review Letters*, 92(13), 2004. ISSN 0031-9007 1079-7114. doi: 10.1103/PhysRevLett.92.130403.

[160] C. Kollath, A. Iucci, T. Giamarchi, W. Hofstetter, and U. Schollwöck. Spectroscopy of ultracold atoms by periodic lattice modulations. *Physical Review Letters*, 97(5), 2006. ISSN 0031-9007 1079-7114. doi: 10.1103/PhysRevLett.97.050402.

[161] C. Kollath, U. Schollwöck, J. von Delft, and W. Zwerger. Spatial correlations of trapped one-dimensional bosons in an optical lattice. *Physical Review A*, 69(3), 2004. ISSN 1050-2947 1094-1622. doi: 10.1103/PhysRevA.69.031601.

[162] N. Syassen, D. M. Bauer, M. Lettner, T. Volz, D. Dietze, J. J. García-Ripoll, J. I. Cirac, G. Rempe, and S. Dürr. Strong dissipation inhibits losses and induces correlations in cold molecular gases. *Science*, 320 (5881):1329–1331, 2008. doi: 10.1126/science.1155309.

[163] Takafumi Tomita, Shuta Nakajima, Ippei Danshita, Yosuke Takasu, and Yoshiro Takahashi. Observation of the mott insulator to superfluid crossover of a driven-dissipative bose-hubbard system. *Science Advances*, 3(12), 2017. doi: 10.1126/sciadv.1701513.

[164] K. M. Birnbaum, A. Boca, R. Miller, A. D. Boozer, T. E. Northup, and H. J. Kimble. Photon blockade in an optical cavity with one trapped atom. *Nature*, 436(7047):87–90, 2005. ISSN 1476-4687. doi: 10.1038/nature03804.

[165] C. Ouellet-Plamondon, G. Sallen, F. Jabeen, D. Y. Oberli, and B. Deveaud. Multiple polariton modes originating from the coupling of quantum wells in planar microcavity. *Physical Review B*, 92(7):075313, 2015. doi: 10.1103/PhysRevB.92.075313.

[166] Neereja M. Sundaresan, Yanbing Liu, Darius Sadri, László J. Szőcs, Devin L. Underwood, Moein Malekakhlagh, Hakan E. Türeci, and Andrew A. Houck. Beyond strong coupling in a multimode cavity. *Physical Review X*, 5(2):021035, 2015. doi: 10.1103/PhysRevX.5.021035.

[167] Dmitry D. Solnyshkov, Guillaume Malpuech, Philippe St-Jean, Sylvain Ravets, Jacqueline Bloch, and Alberto Amo. Microcavity polaritons for topological photonics [invited]. *Optical Materials Express*, 11(4):1119–1142, 2021. doi: 10.1364/OME.414890.

[168] Torsten Karzig, Charles-Edouard Bardyn, Netanel H. Lindner, and Gil Refael. Topological polarito. *Phys. Rev. X*, 5:031001, Jul 2015. doi: 10.1103/PhysRevX.5.031001.

[169] R. H. Dicke. Coherence in spontaneous radiation processes. *Physical Review*, 93(1):99–110, 1954.

[170] Michel Gross and Serge Haroche. Superradiance: An essay on the theory of collective spontaneous emission. *Physics reports*, 93(5):301–396, 1982.

[171] Ralf Röhlsberger, Kai Schlage, Balaram Sahoo, Sebastien Couet, and Rudolf Rüffer. Collective lamb shift in single-photon superradiance. *Science*, 328(5983):1248–1251, 2010.

[172] AP Chikkatur, A Görlitz, DM Stamper-Kurn, S Inouye, S Gupta, and W Ketterle. Suppression and enhancement of impurity scattering in a bose-einstein condensate. *Physical review letters*, 85(3):483, 2000.

[173] Adrian Kantian, Ulrich Schollwöck, and Thierry Giamarchi. Competing regimes of motion of 1d mobile impurities. *Physical review letters*, 113 (7):070601, 2014.

[174] Charles JM Mathy, Mikhail B Zvonarev, and Eugene Demler. Quantum flutter of supersonic particles in one-dimensional quantum liquids. *Nature Physics*, 8(12):881–886, 2012.

[175] Florian Meinert, Michael Knap, Emil Kirilov, Katharina Jag-Lauber, Mikhail B Zvonarev, Eugene Demler, and Hanns-Christoph Nägerl. Bloch oscillations in the absence of a lattice. *Science*, 356(6341):945–948, 2017.

[176] DM Gangardt and A Kamenev. Bloch oscillations in a one-dimensional spinor gas. *Physical review letters*, 102(7):070402, 2009.

[177] Lev Landau. Theory of the superfluidity of helium ii. *Physical Review*, 60(4):356, 1941.

[178] T. Giamarchi. *Quantum Physics in One Dimension*. Oxford University Press, New York, 2003.

[179] M. A. Cazalilla, R. Citro, T. Giamarchi, E. Orignac, and M. Rigol. One dimensional bosons: From condensed matter systems to ultracold gases. *Rev. Mod. Phys.*, 83:1405–1466, 2011.

[180] E. H. Lieb and W. Liniger. Exact analysis of an interacting Bose gas. I. The general solution and the ground state. *Phys. Rev.*, 130:1605–1616, 1963.

[181] T. Kinoshita, T. Wenger, and D. S. Weiss. Observation of a one-dimensional Tonks–Girardeau gas. *Science*, 305:1125–1128, 2004.

[182] B. Paredes, A. Widera, V. Murg, O. Mandel, S. Fölling, I. Cirac, G. V. Shlyapnikov, T. W. Hänsch, and I. Bloch. Tonksñ-Girardeau gas of ultracold atoms in an optical lattice. *Nature*, 429:277–281, 2004.

[183] S. Palzer, C. Zipkes, C. Sias, and M. Köhl. Quantum transport through a Tonks-Girardeau gas. *Phys. Rev. Lett.*, 103(15):150601, 2009.

[184] Andrew G Sykes, Matthew J Davis, and David C Roberts. Drag force on an impurity below the superfluid critical velocity in a quasi-one-dimensional bose-einstein condensate. *Physical review letters*, 103(8): 085302, 2009.

[185] Chen-Ning Yang. Some exact results for the many-body problem in one dimension with repulsive delta-function interaction. *Physical Review Letters*, 19(23):1312, 1967.

[186] M. Gaudin. Un systeme a une dimension de fermions en interaction. *Physics Letters A*, 24(1):55–56, 1967. ISSN 0375-9601. doi: https://doi.org/10.1016/0375-9601(67)90193-4. URL `https://www.sciencedirect.com/science/article/pii/0375960167901934`.

[187] AM Kaufman, RP Anderson, Thomas M Hanna, Eite Tiesinga, Paul S Julienne, and DS Hall. Radio-frequency dressing of multiple feshbach resonances. *Physical Review A*, 80(5):050701, 2009.

Appendix A

Appendix

This is an appendix for technical improvements to which the author of this dissertation contributed.

A.1 Logging magnetic fields

The importance of the precise control of the magnetic field in our lab cannot be overemphasized. All transitions and related accurate measurements depend on the magnetic field, and monitoring of it is absolutely important. There is an in-measurement method called field-tagging (see sec.4.3.1), but this measurement is narrow-windowed, also experiment-dependent. Moreover, magnetic field drifts on a large scale due to sources outside of the lab are of concern as well. This includes fields that are produced by other labs nearby.

To address this issue, we mounted a 3-axis magnetometer (Mag-3MS1000, Bartington Instruments) near the science-cell as shown in fig. A.1 (A) (1). The magnetic field along the vertical axis is measured so that we can extract any large-scale magnetic field drifts that the atoms feel over the experiment.

Similarly, it is important to monitor and stabilize the current of our power supply when accessing $\sim$ 1007G Feshbach resonance (see A. Pazmiño's thesis [114]); for this purpose we use a current transducer (DS600IDSA, Danisense), shown in fig. A.1 (A) (2).

The sensors are read out with 7-1/2 digit digital multi-meters (DMM) (Agilent). To extract the value of magnetic field/current at a certain time, i.e. when the experiment happens, we need to trigger DMMs and the measured values are read out via GPIB. The system configuration is displayed in fig. A.1 (B).

Fig. A.2 shows our Labview-based DMM monitoring program. The digital trigger from the experiment-control system triggers the DMM and the

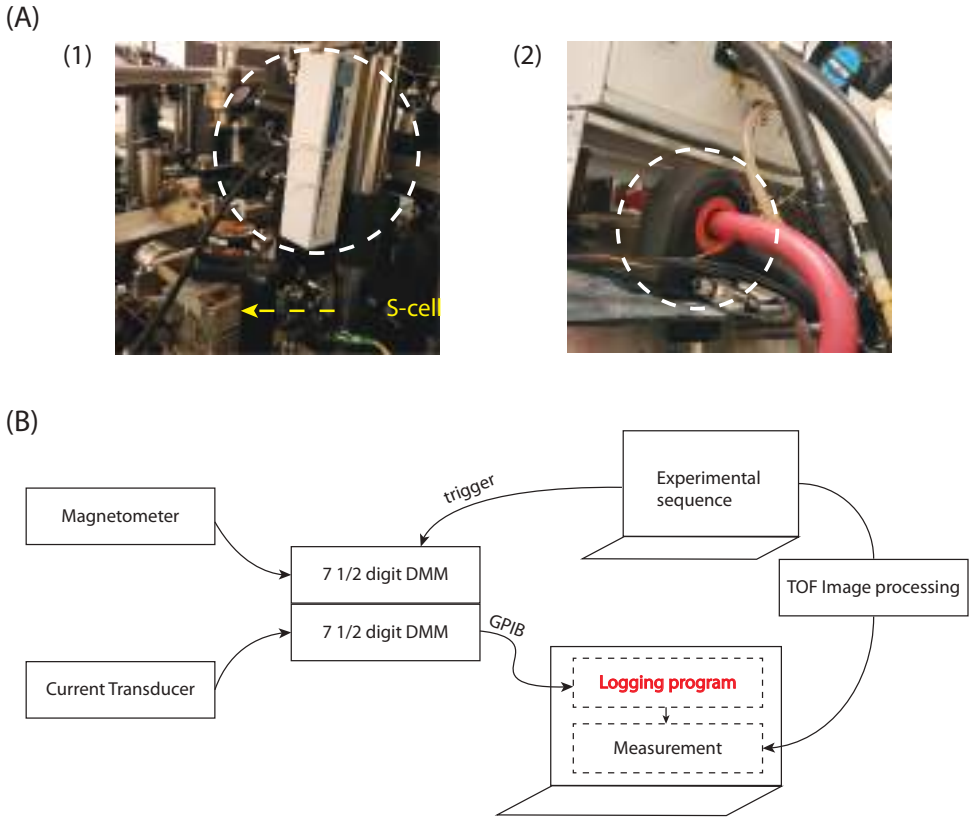

Figure A.1: Field monitoring infrastructure. (A) (1) Magnetometer (in the white dashed circle) is placed near ($\lesssim$ 15cm) the science-cell. The vertical direction of magnetic field is measured. (2) Transducer (marked as white dashed circle) is placed to the input side of IGBT that acts as a switch of large magnetic field coil. For both cases, the measured signal is connected to digital multi-meter (DMM). (B) Schematic diagram of the system configuration.

measured value is then sent to the program and recorded. Depending on the setting, we can record several measurements after a single trigger which is helpful to track the local stability. The program shows the real-time accumulated curve for the convenience, and provides a log file with extra time-stamp so that the values can be matched with the corresponding experimental data. The log is given in .lvm format which is compatible with both Excel and Mathematica.

Figure A.2: DMM monitoring program.

A.2 Automated polarization control

The polarization of our state-dependent lattice determines the strength of the coupling for the different magnetic hyperfine states. To control the polarization, we use a rotatable $\lambda/4$ plate in a linearly polarized beam. In most cases, once the polarizer is set, it is never touched to preserve the target polarization, unless it needs to be changed.

The problem is that, sometimes it is required to rotate the polarization in a very accurate manner. Furthermore, a dynamical change of the polarization may be needed depending on experimental sequence. For example, if we want to change the relative lattice depth of $|r\rangle$ and $|b\rangle$ states using state-dependent lattice frequently, the best way is to change the polarization since changing the wavelength in a real-time measurement is not feasible, with our Coherent 899 Ti:Saph laser.

This motivated us to install a rotational mount with rotatable $\lambda/4$ plate. Fig.A.3 shows the installed automated mount (PRM1Z8, Thorlabs), which

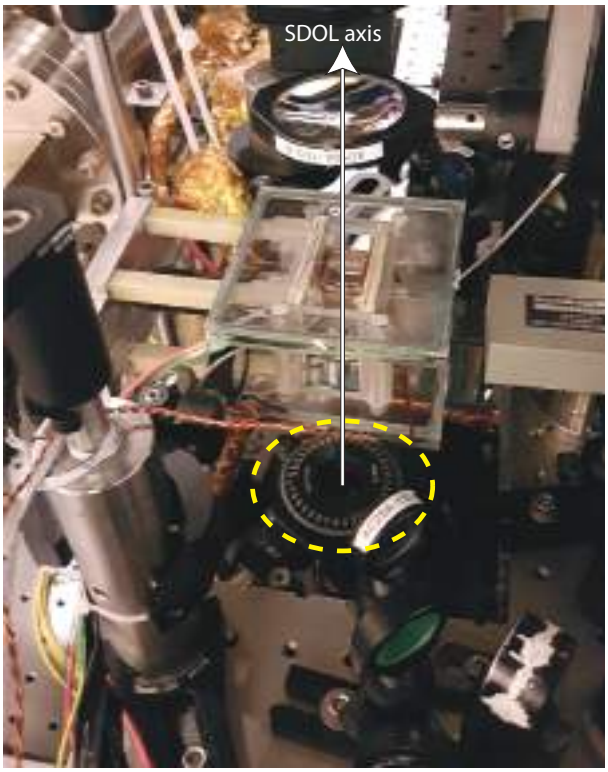

Figure A.3: Step-motor polarizer (dashed yellow circle) is mounted on the way of forwarding state-dependent laser in front (below) of the science cell. The vertical axis that SDOL is elongated is marked as white line.

is connected to a brushed DC servo moter (KDC101, Thorlabs) that is not shown in figure. It is mounted below the science cell on the way for forwarding state-dependent lattice in z-axis. This step-motor polarizer is controlled by a program (Kinesis, Thorlabs) which we connected to our experimental sequence program (Cicero) to enable the execution of pre-set rotations by triggering in the experiment.

Fig.A.4 shows results obtained with the installed system for calibrating the optimal state-dependent light polarization with the rotation angle varied between experimental runs.

A.3 Accordion lattice

The presence of gravity is sometimes very unhelpful in terms of a uniform weakly confining system. We designed new optical lattice setup that gives

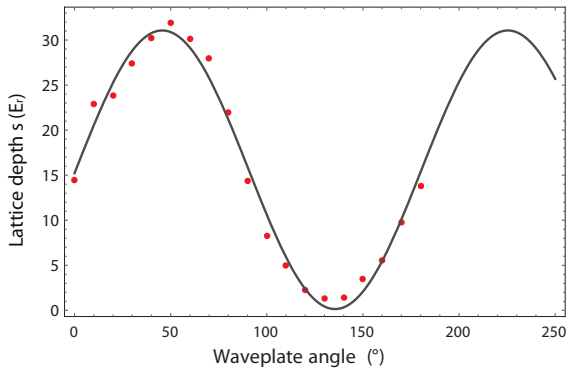

Figure A.4: Lattice depth is measured for different polarization using the installed step-motor polarizer. The lattice depth is measured by KD (Kapitza-Dirac) diffraction, and the polarization is changed by automatic triggering system.

transverse trap confinement in $y' - z$ plane which provides effective 1D tube along x'-axis that is irrelevant to the gravity. Here x' and y' are the new axes that are rotated 45° in the $x - y$ plane.

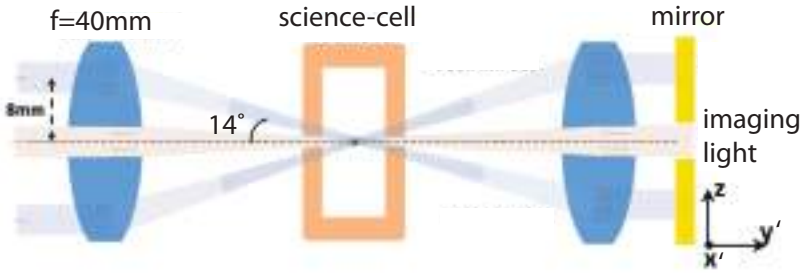

Figure A.5: Design for accordion lattice setup. $f = 40$mm 1-inch lens is the biggest lens that we can mount to the science cell as close as possible due to the existing configuration. Two independent laser beams pass through the same lens above/below with 8mm distance from the center, then cross at the position of the atom in the science cell with the incident angle of 14° against the orthogonal axis. The beam passes the same $f = 40$mm lens behind the science cell to control the profile and reflected back from the mirror. The mirror has a hole (diameter: ≈ 0.8cm) at the center to be compatible with the existing light path for imaging.

The main point of concern for the setup design is to not destroy any existing

setup for the lab consistency. As shown in previous setup for the current beam path, 45° against the science-cell is already occupied by existing $x - y$ optical lattices. This causes a problem when it is combined with the fact that the wall of our science-cell in use is not specially coated for anti-reflection, thus we are not allowed to put the laser beam for the optical lattice with the orthogonal incident angle against the wall plane. Moreover, the space near the science-cell is very restricted due to the presence of the moving coil as discussed in sec.2.1.

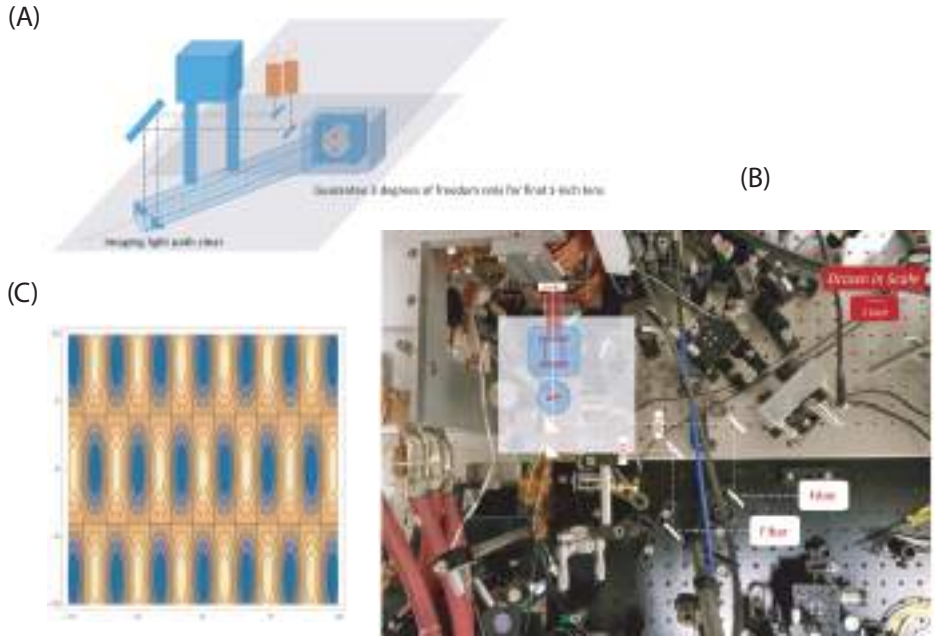

Figure A.6: Accordion lattice beam realization (A) Design of the accordion lattice system in practice. (B) Illustration of the setup on the top of real experimental configuration. (C) Calculated optical potential profile from the accordion lattice

The setup of the accordion lattice came out to circumvent this restriction, which is shown in fig. A.5. Instead of giving the angle of incidence with separate systems, we can use one big lens that focuses down the two laser beams for optical lattices at the same time. Two beams are separated enough not to interfere with each other and also not to touch the existing imaging light path. At the same time, however, if the beams are located too far close to the edge, the lens does not work as supposed due to the spherical aberration (using aspheric lens is helpful, but this requires more space in general).

In terms of the incident angle, the ideal angle is 45° which gives orthogonal lattices. In our system, the largest available angle is 14°, which is marginal

but still feasible to make 2D optical lattices. At the exit side of the glass cell, we need an additional $f = 40$mm lens in combination with a retro-reflecting mirror which is shown in fig. A.7. The reflecting mirror has a hole in the center so that the imaging light can propagate through.

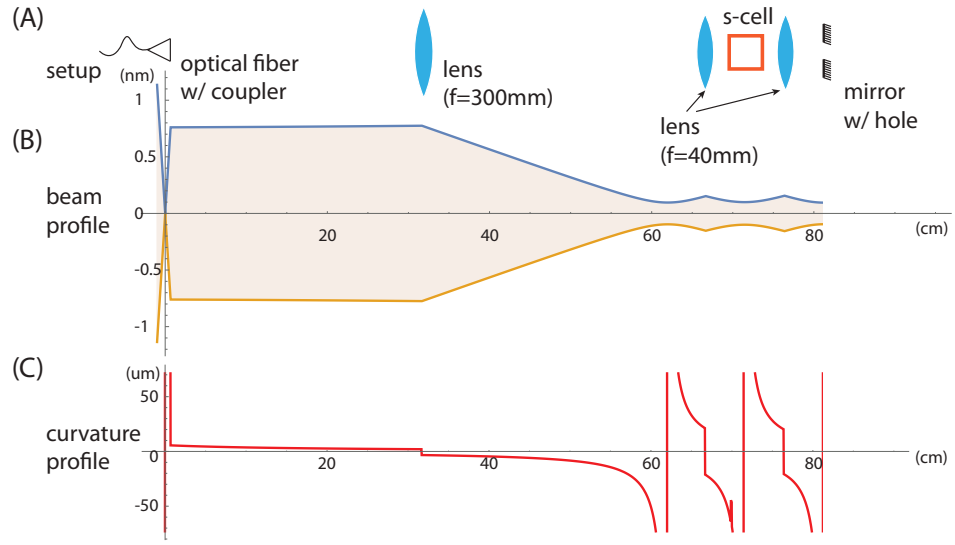

Figure A.7: Accordion lattice beam profile. (A) The schematic diagram of setup is drawn in scale to be compared with for beam profile below. (B) Calculated beam profile with the equipped parameters. (C) Corresponding beam curvature. At the position of the atom where beam is focused, the curvature is infinite.

Fig. A.6 shows the practical setup of the accordion lattice. Due to space limitations, we decided to mount the final lens in an upside down way, and this is done by putting the second layer which is depicted as a white box in fig. A.6 (B). Fig. A.6 (B) shows the setup on top of the current configuration at the early phase of the project, which are mostly in place now, except the white box zone which consists of a tube-like lens mount and a rotational mount. The purpose of the rotational mount is to tilt the beam with a very small amount for the final alignment.

Fig. A.7 shows the calculated beam profile for the designed setup. The choice of fiber couplers and lens in earlier beam path are also made for optimizing the lattice profile at the science cell. The beam profile in fig. A.7 (B) inside the science cell is not diverging or converging too much so that the lattice can capture atom uniformly. The waist at the focus is designed (and tested) as $\sim 100\mu$m, and this can be adjusted down to $\sim 60\mu$m within current

setup. The calculation is done with 'ABCD' matrix method [141], and this gives the beam curvature as well, shown in fig. A.7 (C). The curvature diverges at the focus (where atom is supposed to be) as planned.

A.4 Microwave amplifier

We use microwave radiation at $\sim$ 6.8GHz to couple $F = 1$ levels and $F = 2$ levels.

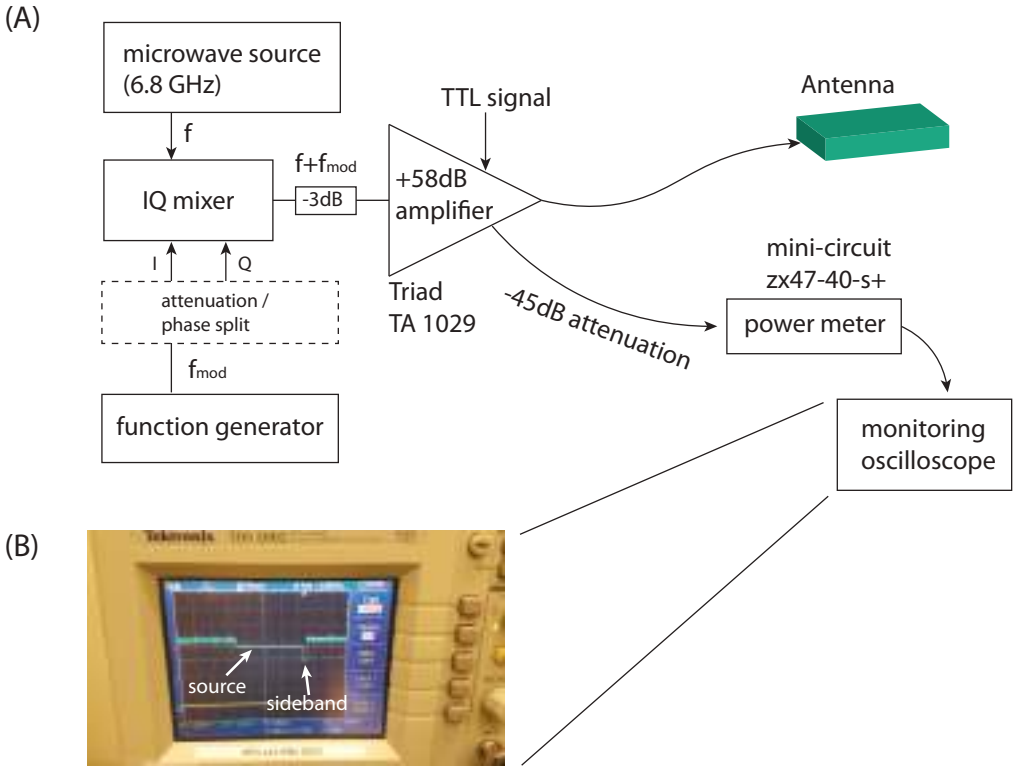

Figure A.8: (A) Schematic diagram of microwave amplifying system with newly implemented monitoring feature. (B) Recorded output signal. The first step in signal is from the microwave source (6.8GHz) that is not resonant with the energy level of atom. The second step is from the sideband that is mixed with the power/frequency from the function generator, and this is the pulse that is in use for the experiment.

After a decrease in power of our existing system (cf. PhD thesis of D. Pertot [110]), we installed a new amplifier with $\sim$ 58dB amplification (TA1029, Triad

RF Systems). The microwave source that provides 6.8GHz is mixed with RF frequency from a function generator that we can arbitrarily control, and then amplified [110]. The amplifier allows to monitor its output with −45dB of natural attenuation inside, which is useful to compensate any thermal drifts. We connected this monitoring output to a Mini Circuits powermeter (ZX-47-40-$s+$) whose output is displayed on an oscilloscope with a proper trigger at an instance of measurement as shown in fig.A.8 (B). The first inverted plateau is a pre-triggered signal from the main band of the microwave source which is not resonant with the atom, and the second inverted peak is the resonant microwave pulse that we are using in experiments.

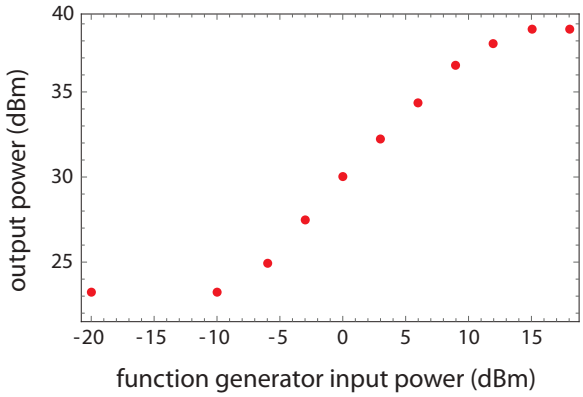

Figure A.9: Microwave output power gain curve. Function generator that create f_{mod} frequency controls the final output microwave power at antenna. The output power is monitored with −45 dB attenuation from the monitoring port, and then re-adjusted (see fig. A.8 (A)). There is 2 $\sim$ 3dB loss from a cable, and this is also the case for the output side. The power seems saturated around $\sim$ 40dBm ($\sim$ 42dBm with a consideration of cable loss) , which is a little bit lower than 44dBm (Psat specification).

Fig. A.9 shows the gain curve of the new amplifier. The output power is monitored from the system described above (fig. A.8) and then converted into units of power (dBm). We set the active linear region of input from the function generator side up to 20dBm, to protect our internal circuit configuration. The gain curve gives an amplification of 56dB which is a bit short of the specification, but still acceptable.